BOTTOM-UP SIMULATIONS OF NANOPARTICLE SURFACE LAYERING AND CORONA FORMATION

by

Gene Chong

A dissertation submitted to Johns Hopkins University in conformity with the

requirements for the degree of Doctor of Philosophy

Baltimore, Maryland

July 2019

Abstract

Nanoparticles (NPs), by way of their coating, can acquire biomolecular coronas, hindering their intended function and potentially leading to toxicity. However, knowledge of how a NP's initial surface chemistry dictates the protein or lipid composition of its corona and biological response is limited. We use a combination of all-atom molecular dynamics (MD) and coarse-grained dissipative particle dynamics (DPD) simulations to determine the surface structure of engineered gold nanoparticles (AuNPs) and their surface chemistry-dependent transformations. We develop a complementary MD simulation and experimental approach to determine preferential orientational binding in and the converged structure of protein coronas with amino acid-level specificity, using a limited number of 200 ns simulation trajectories. All-atom MD simulations further reveal that typical engineered (AuNPs), such as self-assembled monolayers on AuNPs and polyelectrolyte-wrapped AuNPs, are not pristine. Instead, they have heterogeneous spatial charge and hydrophobic group distributions on their surface. This non-uniformity plays an important role in interactions of AuNPs with lipids, which have distinct spatially distributed hydrophobic head- and hydrophilic tail-groups. We incorporate this molecular-level complexity into coarse-grained NP models to reveal mechanisms of NP insertion, lipid extraction, bilayer thinning, and membrane disruption at microsecond time-scales *via* DPD simulations. We thereby establish that non-uniformity in NP surface functionalizations matters, and determine molecular-level transformations that could trigger the onset of toxicity.

Advisor: Dr. Rigoberto Hernandez

Readers: Dr. Howard Fairbrother, Dr. Kit Bowen

Acknowledgments

Completing this thesis would not be possible without, first, my advisor Professor Rigoberto Hernandez. I thank him for his advice, support, respect, and trust. I would also like to thank my collaborators Meng Wu and Catherine Murphy, Elizabeth Laudadio and Robert Hamers, and Emily Tollefson and Erin Carlson, whose work I share in this thesis. The stories I wrote would not be complete without them. I thank my committee members Professors Howard Fairbrother and Kit Bowen for welcoming and helping me since I moved to Johns Hopkins. I thank Hailey Bureau, my mentor and friend in the group, and Dr. Alex Popov for his insightful questions and support. Many thanks to Ben Frank and Miranda Gallagher, my first and closest friends at Johns Hopkins and the CSN, and to my CSN cohort and friends, Emily Caudill, Diamond Jones, and Arielle Mensch. I am grateful for my friends, roommates, and travel buddies at GA Tech: Svetoslav Nikolov, Harrison Ansley, and Linda Nhon. We've traveled 0.14% of the world together and counting. Last but not least, I thank my mom, dad, sister, brother-in-law, nephews, and Momo for always being there.

Contents

List of Tables

List of Figures

Chapter 1

Introduction

1.1 Motivation

Nanoparticles (NPs) are 1-100 nm along their smallest dimension with tunable shape, size, and surface chemistry [1, 2]. At this nanoscale size range, NPs have a higher surface area to volume ratio, increasing the area for interactions at interfaces, with applications in catalysis [3], energy storage [4], cosmetics [5], dyes [2, 5], and biomedicine [2]. With advances in the synthesis and control over the functionalization and functionality of engineered NPs, attention is increasingly being brought to the sustainability of these materials. After use, NPs can get discarded into the environment at the end of use, where their entry into various nodes of the food web could have deleterious effects at the ecosystem level [6, 7]. *Do the technological benefits of NPs outweigh the health risks?*

Initial efforts to understand NP sustainability have primarily focused on large-scale toxicological studies of cell and organismal viability in response to NP exposure. NPs with cationic surfaces are generally more toxic than anionic NPs [8, 9, 10]. However, design rules for implementing sustainability into NPs should shift focus from the correlation between NP surface chemistry and toxicity to causation. After all, "nano" is an umbrella term for size, but nanomaterials are diverse in core material, shape, size, and ligand structure. NPs functionalized with different cationic ligands or with the same cationic ligand but different NP size exhibit varying degrees of organismal stress and cytotoxicity [11, 12, 13], and even anionic NPs can induce biological response [8, 14, 15, 16, 17].

Determining causation of NP toxicity towards sustainable NP design is a multi-scale problem: starting from an NP's first contact with the biological environment, to the molecular-level transformations that occur at this nano-bio interface, and the biological response pathways triggered from these physiological changes. After NPs are initially synthesized, they generally need to be functionalized with charged organic ligands, such as thiols and polyelectrolytes, to protect the core and impart colloidal stability. The ligand layer is, thereby, the first to interface with biomolecules, such as extracellular proteins and lipid membranes.

The model nanoparticles we use are gold nanoparticles (AuNPs), as they are biologically inert and technologically relevant. Their biocompatibility coupled with the plasmonic properties of NPs makes AuNPs an ideal choice for biomedical applications such as sensing [18, 19] and targeted therapeutic [20, 21] agents. The biocompatibility of AuNPs also enables their use as models to probe how the ligand layer of NPs–whether functionalized for biological applications, or other technological devices that might get discarded into the environment at end-of-life–interfaces with biological systems [6]. By tuning the AuNP shape, size, and ligand structure, we decipher the interdependence of these variables on the molecular-level surface structure of NPs towards developing design rules to control their surface chemistry-dependent transformations in complex biological environments.

1.2 Thesis Objectives

Computer simulations can potentially link atomistic-scale interactions between nanoparticles and biomolecules to the onset of toxicity in cells, but require accurate bottom-up coarse-graining to tackle this inherently multiscale problem [22]. A common bottom-up coarse-graining strategy for complex multicomponent systems, such as nanoparticles in suspension media or in biological environments, starts with the atomistic structure of each component at the lowest scale and then groups neighboring atoms with similar chemical properties into larger beads at the higher scale.

We take this bottom-up approach by first using all-atom molecular dynamics (MD) simulations to determine the surface structure of typical engineered AuNPs with different methods of surface functionalization, such as self-assembled alkanethiol monolayers and polyelectrolyte wrappings on AuNPs. The next objective is to develop structurally benchmarked coarse-grained models of these engineered AuNPs. The particular coarse-graining scheme we apply is to group approximately three adjacent methylene groups along the charged, organic ligand chains into a larger hydrophobic bead and charged terminal groups into a charged bead. We benchmark these simpler models such that the coarse-grained ligands self-assemble into the structures observed in the all-atom MD simulations. We, then, implement coarse-grained simulations of these NP models with lipid-bilayer systems to determine the influence of molecular-level surface structure, such as spatial charge and hydrophobic group distribution, on lipid corona formation and other transformations at the nanoparticle-lipid bilayer interface at longer time- and length-scales.

1.3 Thesis Structure

A detailed overview is provided in Chapter 2 on our approach and challenges to characterizing the molecular-level structure of engineered nanoparticles and their transformations in biological environments.

In Chapter 3, we present published work in Ref. [17] on a combined, complementary computational and experimental approach to determine the evolution and molecular structure of protein coronas on AuNPs. We implemented a computational assay technique using a cross-correlation of a small ensemble of 200 ns long MD trajectories to identify a preferred nonrigid binding orientation of the peripheral membrane protein cytochrome *c* on anionic ligand-coated AuNPs. Our experimental collaborators employed a mass spectrometry-based footprinting method that enables the characterization of the stable protein corona that forms at long time-scales in solution. Through the combination of these computational and experimental primary results, we have established a consensus result establishing the identity of the exposed regions of cytochrome *c* in proximity to the AuNP and its complementary pose(s) with amino-acid specificity. Moreover, the tandem use of the two methods can be applied broadly to determine the accessibility of membrane-binding sites for peripheral membrane proteins upon adsorption to AuNPs or to determine the exposed amino-acid residues of the hard corona that drive the acquisition of dynamic soft coronas. We anticipate that the combined use of simulation and experimental methods to characterize biomolecule-nanoparticle interactions, as demonstrated here, will become increasingly necessary as the complexity of such target systems grows.

We detail another combined experimental and computational approach in Chapter 4 on published work in Ref. [23] to determine the structure of self-assembled alkanethiol monolayers on AuNPs. Specifically, our collaborators developed a solution NMR-based analysis of quaternary ammonium-terminated alkanethiol monolayers on AuNPs with diameters from 1.2 to 25 nm. The chemical-shift analysis of the proton signals from the solvent-exposed ammonium headgroups suggests that the headgroups are saturated on the ligand shell as the sizes of the NPs increase beyond ∼10 nm. Quantitative NMR shows that the ligand density of these alkanethiols is size-dependent. Ligand density ranges from ∼3 molecules nm^{-2} for 25 nm particles to up to 5-6 molecules nm^{-2} in ∼10 nm and smaller particles. MD simulations of 4, 6, and 8 nm alkanethiol-coated AuNPs confirm greater hydrophobic chain packing order and saturation of charged headgroups within the same spherical ligand shell at larger nanoparticle sizes and higher ligand densities. Combining the NMR studies and MD simulations, we establish the relationship between the AuNP size, molecular structure of the ligand, ligand density, and self-assembled monolayer (SAM) structure on AuNPs.

In Chapter 5, we present published work in Ref. [24], in which we determined the structure of another class of typical engineered AuNPs, specifically long polycations layered on anionic AuNPs. While top-down coarse-grained models of polyelectrolyte-coated AuNPs have focused on polyelectrolytes of short length, from 10 to a 100 monomers represented as one charged bead per monomer, here we used MD simulations and bottom-up coarse-grained approaches to access more typical polymer lengths on the order of 200 monomers. Specifically, we simulated the adsorption dynamics and structure of one or two such long polycations on negatively charged 4 nm citrate-coated AuNPs within implicit or explicit solvents. The first polycation coats approximately half of the AuNP surface regardless of solvent model and leaves a significant part of the anionic citrate layer exposed to absorption by a second polycation. We find that the most prevalent structural features across solvent conditions consist of 1–2-monomer loops or kinks. They extend radially from the nanoparticle surface and assemble into a double-layered coating of the AuNP. We compile a set of structural features of adsorbed polycations that would be ripe for coarse graining and outline a bottom-up coarse-graining scheme for simulations of polyelectrolyte-coated AuNPs with amphiphilic biomolecules that incorporates the hemispheric polycation coverage with exposed citrate layer, surface-bound bilayer-like segments, and long amphiphilic loops and tails.

Continuing our work on developing structurally accurate models for typical engineered AuNPs, we detail in Chapter 6 our characterization of the citrate layer on as-synthesized AuNPs and its stability upon polycation adsorption, the latter process which is highlighted in Chapter 5. Specifically, we present published work in Ref. [25], in which we simulated the packing of citrate^{3-} and H_2citrate^{-} onto AuNPs to understand how citrate anions cap and stabilize AuNPs. We determine the molecular configurations of citrate on 4, 6, and 8 nm AuNP surfaces as a function of charge state and packing density and find that both the distribution of configurations and maximum packing density are independent of AuNP size. A combination of MD simulations and *in situ* Fourier transform infrared spectroscopy (FTIR) is employed to compare the molecular configurations, stability, and density of citrate on 4 nm citrate-coated (cit-AuNPs) and within polycation-wrapped 4 nm cit-AuNPs. FTIR experiments indicate the presence of H_2citrate^{-} within polycation-wrapped cit-AuNPs with coordination between the H_2citrate^{-} layer and polycation layer in agreement with simulations. Intermolecular hydrogen bonding between terminal carboxylic acid groups of H_2citrate^{-} stabilizes the anionic layer at the interface between cit-AuNPs and adsorbing charged molecules. The calculated total density of H_2citrate^{-} on AuNPs decreases from 3.3×10^{-10} to 3.0×10^{-10} mol/cm^2 upon adsorption of a polycation due to some displacement of dangling H_2citrate$^-$hydrogen bonded to the surface-bound layer. The density of the surface-bound layer is consistently 2.8×10^{-10} mol/cm^2 with and without polycation adsorption. We provide all-atom level insight into the distribution and organization of experimentally derived binding modes of citrate on bare and coated cit-AuNPs. The citrate density and surface charge density are determined for all-atom and coarse-grained modeling of cit-AuNPs, their functionalization, and transformations in complex environments.

In Chapter 7, we introduce the dissipative particle dynamics (DPD) coarse-grained method that we implement for simulations at the nanoparticle-lipid bilayer interface. We present the development and structural benchmarking for coarse-grained models of alkanethiol- and polycation-coated NPs from the all-atom structures determined in Chapters 4-6, as well as for lipid-vesicle systems.

In Chapter 8, we detail the results from the DPD models and methods developed in Chapter 7. We first highlight published work in Ref. [26], in which we use our all-atom polycation-coated AuNPs to validate the corresponding coarse-grained MARTINI model and simulate lipid self-assembly on such AuNPs towards understanding the lipid coronas that these NPs can acquire as observed experimentally. We also present work from manuscripts in preparation on coarse-grained DPD simulations to directly probe transformations at the interface between nanoparticles and lipid-bilayer systems. As an example, metal NPs functionalized with SAMs of alkanethiol ligands are subject to defects in the SAM structure due to the interplay between alkyl chain packing and free volume available in space per ligand. We find *via* coarse-grained dissipative particle dynamics simulations that hydrophobic contact between protruding lipid tails from bilayers and exposed alkyl chains in SAM defects prompts NP insertion and that defects become sites for lipid extraction. We also report that lipid extraction and the structure of the ligands inserted in bilayers collectively contribute to bilayer thinning at the site of NP insertion and bilayer curvature-dependent deformability, revealing how these commonly synthesized NPs interface with lipid-bilayer systems with potential biological consequences.

Lastly, In Chapter 9, we proffer concluding remarks, new insights from this work, and future directions.

Chapter 2

Bottom-Up Characterization for Sustainable Nanotechnology: Non-Uniformity in Nanoparticle Surface Chemistry and Mechanisms of Corona Formation

2.1 Introduction

When nanoparticles (NPs) are released into a biological environment, they can quickly acquire biomolecular coronas. The evolution of protein coronas on NPs has been extensively studied. The hard corona consists of long-lived, surface-bound proteins, while the soft corona dynamically changes with exchangeable, weakly associated proteins [27, 28, 29, 30]. The procurement of protein coronas has been shown to exhibit toxicity, and suggested mechanisms include deformation in protein structure and impairment of function; alteration in the display of protein epitopes and activation of an immune response; and facilitation of NP internalization into cells and DNA damage [27, 28]. However, knowledge of particular nanoparticle surface chemistries and corona proteins that causally trigger a toxicological response is limited [27, 31]. The acquisition of lipid coronas is also possible and has been less studied, but has been shown to disrupt membrane structure and fluidity [26].

Moreover, experimental characterization of biomolecular coronas has largely focused on top-down measurements, such as the acquisition of a corona itself and its correlation to toxicity. Computer simulation studies have also taken a top-down approach, assuming spherically symmetric surface chemistry in spherical NP models and varying effective surface charge, charge density, and core size [32, 33, 34, 35]. Experiments have shown that NPs of similar size and same effective charge, but different ligand, have distinct protein compositions in their corona [36]. Similarly, polycation-coated AuNPs aggregate after acquiring lipids, while cationic alkanethiol-coated AuNPs do not, suggesting a unique lipid-corona structure by ligand type [37].

We take a bottom-up approach by first using all-atom molecular dynamics (MD) simulations to obtain the missing molecular-level information on the NP surface. The challenges in capturing the NP surface structure and surface chemistry-dependent transformations at a fully atomistic scale are limitations in the accessible system sizes and timescales [38, 22]. As an example, an MD simulation of the adsorption of a long 200-mer polycation onto a single 4 nm citrate-coated gold nanoparticle (AuNP) in solution under experimentally and physiologically relevant 0.1 M salt concentration, discussed in Chapter 5 and Reference [24], yields a system size of 500,000 atoms. The end-to-end adsorption of the polycation onto the NP takes place within 120 ns simulation time, and the computation time per 120 ns trajectory is on the order of several weeks. Multiple trajectories are required to approximate an equilibrium ensemble, and this single project can use up all of the available computational resources that could best be allocated to multiple projects. We, thereby, must go up in scale and system complexity by implementing coarse-grained simulations with structurally benchmarked coarse-grained NP models, such as for the polycation-coated AuNP, in tandem with complementary experiments developed by collaborators for high molecular-level sensitivity measurements to determine the distinguishing characteristics of NP surface chemistries and mechanisms of their transformations.

2.2 All-Atom Simulations and Protein Footprinting: Deciphering Bottom-up Evolution of Protein Coronas

Here, we briefly discuss the scalability issue in using all-atom MD simulations for capturing protein corona formation on an anionic ligand-coated AuNP and solutions to the problem. Detailed results and discussion are presented in Chapter 3 and Reference [17].

From six 200 ns trajectories starting from the electropositive protein cytochrome *c* (cyt *c*) deposited in a different orientation for each trajectory near an AuNP uniformly coated with mercaptopropionic acid (MPA), we found no clear preferred orientation of the protein on the MPA-coated AuNP (MPA-AuNP). We were also limited in the number of trajectories to establish a statistical distribution of protein orientations. However, we find that lysine residues drive the nonrigid binding of cyt *c* to MPA-AuNPs *via* salt-bridge formation between lysine ammonium groups and MPA carboxylate groups. This molecular-level detail informed our collaborators Carlson and co-workers on how to setup their protein footprinting experiments. By chemically modifying lysine residues in free cyt *c* in solution and in cyt *c* incubated with MPA-AuNPs followed by mass spectrometry-based analysis, lysines bound to the MPA-AuNP surface or facing a neighboring protein in the corona should have decreased modification compared to the same lysine residues in free cyt *c*. Solvent-accessible lysines should have no change in modification. Lysines that become more solvent-accessible due to deformations in cyt *c* upon binding to the MPA-AuNP should have increased modification compared to the same lysine residues in free cyt *c*. Through this complementary computational and experimental approach, we find two poses from our six 200 ns simulations that persist in the 18 h incubation of cyt *c* with MPA-AuNPs (Figure 1).

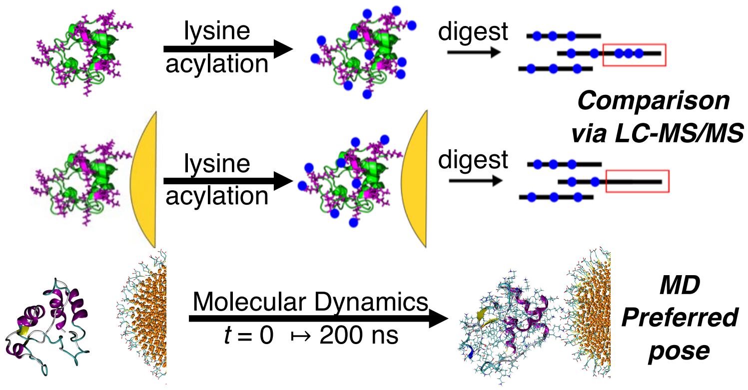

Figure 1: (Top) Workflow of protein footprinting experiments for cytochrome *c* without exposure to MPA-AuNPs or with 18 h exposure to MPA-AuNPs. (Bottom) 200 ns molecular dynamics simulation of cytochrome *c* initially positioned near MPA-AuNP.

Our bottom-up approach incorporates a spiral feedback mechanism between the results from simulation and experiment. From an initial set of simulations, we can determine the molecular-level interactions that drive the binding of proteins on engineered NPs and can be targeted *via* protein footprinting experiments. Experimental results can guide simulations to focus on a smaller set of initial protein orientations near the NP, reducing the amount of sampling and computational cost. Simulations can further determine the molecular-level structure of the hard corona that facilitates the formation of soft coronas.

In our first implementation of the tandem MD simulation and protein footprinting approach, we used an AuNP with spatially uniform, anionic surface chemistry and could focus on the orientation of the protein relative to the AuNP. Our methods can be broadly applied such that we can reduce the sampling of the initial orientation of the protein based on footprinting experiments and, in turn, sample the orientation of the NP.

2.3 All-Atom Simulations and Solution-Based Spectroscopy: Non-Uniform Surfaces of Typical Engineered Nanoparticles

For our bottom-up approach, what information do we need to construct all-atom models of engineered AuNPs, such as the MPA-AuNP described in the previous section? Ligand binding mode (*e.g.* electrostatic, noncovalent, covalent), ligand density, and the average length of a polymer (if for polyelectrolyte-coated AuNPs [39]), are sufficient, but ligand-shell characterization has largely been done on dried samples, using X-ray photoelectron spectrsocopy [40], thermogravimetric analysis [41], attenuated total reflectance-Fourier transform infrared spectroscopy (ATR-FTIR) [42], and solid-state nuclear magnetic resonance (NMR) spectroscopy [43]. The drying of NP samples can lead to aggregation of free ligands, thereby overestimating the ligand density. Since NPs are likely to be released into aqueous environments, solution-based techniques are needed to understand both the structure and dynamics of the NP surface *in situ*.

Our collaborators Murphy and co-workers developed solution-based NMR analyses for self-assembled alkanethiol monolayers on AuNPs and found AuNP size-dependent ligand density and ligand headgroup mobility. By varying AuNP size and ligand density within the range calculated from the experiments, we found through MD simulations that for ligands with headgroup volumes larger than sulfur, the headgroup layer saturates with increasing AuNP size and lower surface curvature, limiting ligand density and reducing headgroup mobility [23]. For alkanethiols with short ligand chains, such as MPA, there is little hydrophobic chain packing and less volume available in space per ligand, and charged headgroups are closer together and repellant, leading to a uniform spatial distribution of ligands in the monolayer. For longer ligands and at higher surface curvatures, there is greater competition between ligand chain packing and free volume available in space per ligand, leading to a heterogeneous distribution of ordered (*i.e.* packed ligands) and disordered domains in the monolayer.

For ligands with titratable groups, a high localization of charge on the NP surface can shift the pK_a of ligands [44]. Therefore, NP models can have the approximate ligand density but inappropriate charge density. If ligand density were overestimated from characterization of dried samples, then indeed a high surface charge density on the NP surface would be unsuitable and unstable in simulation. In the case of citrate–the common capping layer in AuNP synthesis and substrate for polyelectrolyte wrappings [12] and protein corona studies [33, 34], the charge state in solution at neutral pH is citrate^{3-}, but was found to be in the doubly protonated H_2citrate$^-$ state on the AuNP surface [42]. We used MD simulations to pack citrate^{3-} or H_2citrate$^-$ onto AuNPs and observed the desorption of excess citrate and equilibration of citrate anions into a stable population of binding modes (Figure 2). Deposition of a polycation onto citrate-coated AuNPs show that the citrate layer is stable at charged interfaces only if in the H_2citrate$^-$ *via* hydrogen bonding between the terminal carboxylic acid groups of neighboring citrate. The binding modes of H_2citrate$^-$ and molecular interactions between H_2citrate$^-$ and the polycation were confirmed using *in situ* ATR-FTIR [23]. We, thus, determined the stable charge state and charge density of citrate on AuNPs for both all-atom and coarse-grained models. Polycation wrappings on citrate-coated AuNPs show non-uniform spatial charge and hydrophobic distribution and coverage on the NP surface [24, 25].

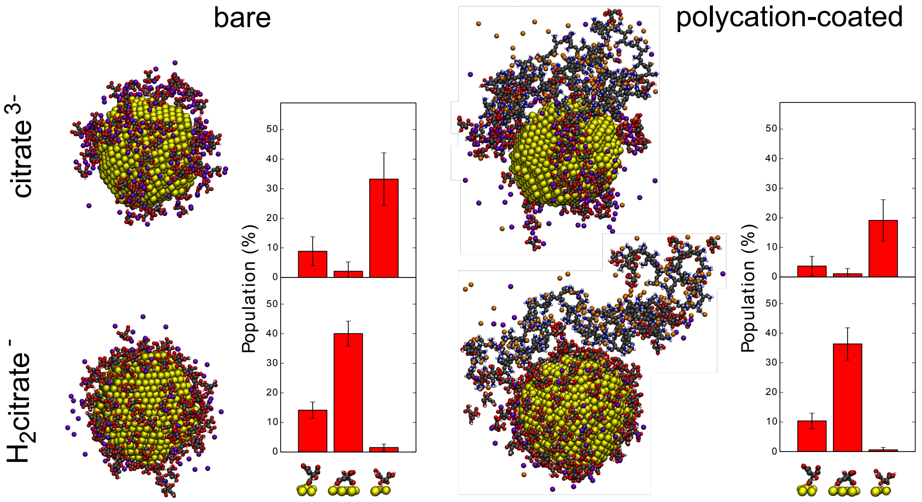

Figure 2: Population of binding modes and stability by charge state of citrate anions and non-uniform adsorption of polycations on citrate-coated AuNPs.

2.4 Bottom-Up Coarse-Grained Simulations: Influence of Spatial Chemical Heterogeneity on Nanoparticle Transformations

We develop force-field parameters for coarse-grained dissipative particle dynamics (DPD) simulations to reproduce the spatially distributed ordered and disordered ligand domains in alkanethiol monolayers on AuNPs (Figure 3). The cationic ligands promote attraction with the anionic phosphate groups in the lipid vesicle. Further, the exposed hydrophobic chains in the ordered ligand domains on NPs prompt contact with hydrophobic lipid tails, NP insertion, and lipid extraction. This minimum level of detail is required in understanding molecular-level transformations of engineered NPs and can be obtained from determining the molecular-level structure through all-atom MD simulations and complementary solution-based experimental techniques. A different transformation by polycation-coated AuNPs at the nano-bio interface can be attributed to a distinct spatial charge and hydrophobic group distribution of polycations on AuNPs compared to alkanethiol ligands.

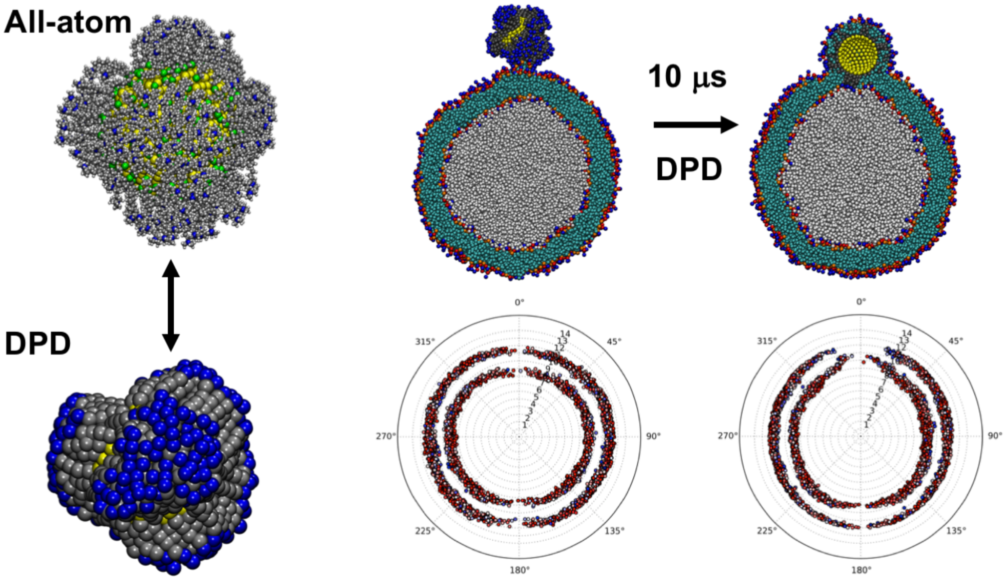

Figure 3: Bottom-up coarse-graining of defects in self-assembled monolayers on AuNPs that drive NP insertion, lipid extraction, and bilayer thinning at the μs timescale from coarse-grained dissipative particle dynamics (DPD) simulations.

2.5 Conclusion

In this Chapter, a review of the chapters and connection between chapters have been described. Concluding remarks and future directions based on these results are addressed in Chapter 9.

Chapter 3

Preferential Binding of a Peripheral Membrane Protein to a Uniformly Anionic Gold Nanoparticle

3.1 Introduction

When nanoparticles (NPs) interact with proteins, they might alter the protein's secondary, tertiary, or quaternary structures critical to protein functionality, causing unexpected organismal stress, toxicity, or other unanticipated biological consequences [45]. It is well established that the characteristics of NPs, such as their composition, size, and ligand coating, are crucial to their interactions with proteins and other biomolecules [46]. Both computational modeling and advances in the experimental synthesis of NPs have enabled controlled synthesis of NP shape, size, and surface chemistry to probe NP surface-specific interactions with biomolecules [23], but developing a predictive mechanistic understanding of how a nanoparticle transforms and triggers toxicity depending on its initial surface chemistry is the ultimate challenge [6, 36]. Experimental characterization of the nano-bio interface with high molecular-level sensitivity has been limited and has largely focused on the acquisition of a protein corona by NPs, more generally, and its effect on cytotoxicity [36, 29, 47, 48, 49]. Likewise, the dynamic evolution of protein coronas and other nanoparticle transformations across multiple time- and length-scales is inaccessible through all-atom molecular dynamics simulations (MD) due to limitations in computational power [22].

MD simulations at all-atom to coarse-grained scales indeed have emerged as a useful tool for exploring non-static binding partners such as that involving a protein (or proteins as in corona formation) and a nanoparticle [35, 50, 51, 52]. The difficulty in identifying the preferred orientation of biomolecules towards a given NP using MD simulations is exacerbated by the near degeneracy of many putative binding sights on the NP due to the self-similarity–if not quite uniformity–of the NP. Nevertheless, if one samples the initial conditions sufficiently to remove biases that could lead to local minima in the binding process, one can predict properties of the protein-NP system such as protein face- and amino acid-specific interactions with NP ligands that drive the formation and structuring of coronas on NPs. The corresponding experiments to such simulations have thus far confirmed the general orientation of proteins on NPs *via* NMR [32, 33] and the presence of salt-bridge formation between carboxylate-terminated NP ligands and ammonium groups, as present in the amino acid lysine, *via* infrared spectroscopy [25].

To identify specific amino acid residues involved in protein-NP interactions, mass spectrometry-based methods have been developed to determine the specific residues responsible for interaction between biomolecules, called protein footprinting [53, 54]. Protein footprinting utilizes the differential solvent accessibility of amino acids in a free protein relative to a protein that is complexed with another biomolecule or material. This technique has been widely utilized to study many processes such as protein-protein and protein-ligand interactions, and has been successfully applied to protein-NP systems [55, 56, 57, 58]. For example, Dordick and co-workers [55] utilized lysine-specific acylation coupled with matrix assisted laser desorption-ionization time of flight tandem mass spectrometry (MALDI-TOF MS/MS) to propose which faces of cytochrome *c*, RNase A, and lysozyme interacted with 4 and 15 nm silica nanoparticles.

When paired with molecular dynamics (MD) simulations, protein footprinting can be used as a robust experimental technique to determine the accuracy of the predicted models of protein-nanoparticle interactions and assist in improving simulations; likewise, the computational models can provide deeper insight into conformational information that cannot be probed by surface accessibility experiments alone. In the present work, the amino acid residue-specific interactions predicted by simulation for a protein-NP system were validated experimentally using mass spectrometry-based protein footprinting. We establish protein footprinting as a complementary experimental technique to identify preferential binding of proteins to NPs and reduce the number of initial starting configurations needed for simulations.

Specifically, we examine the model system of horse heart cytochrome *c* (cyt *c*) and 4 nm 3-mercaptopropionic acid (MPA) coated gold NPs (AuNPs)–which we call MPA-AuNP throughout this work. Cyt *c* associates with anionic lipid domains in the inner mitochondrial membrane and is directly involved in the electron transport chain when bound to the membrane and indirectly in cell apoptosis when removed from the membrane [59]. The exact location of the anionic phospholipid hosting region(s) in cyt *c* and, therefore, the final orientation(s) of the protein on bilayers containing anionic phospholipids has been highly debated [60, 61], and some of us recently suggested a possible resolution [16]. Specifically, the degree of binding between cyt *c* and the lipid bilayer was found to exhibit preferred orientational binding sites in cyt *c*, and to vary depending on the model bilayer composition [16]. Experiments have shown that MPA-AuNPs only weakly associate with supported lipid bilayers but associate strongly in the presence of cyt *c* on bilayers proportional to the number of cyt *c* bound to the bilayer [16]. AuNPs coated with polyacrylic acid were also found to remove a small population of cyt *c* weakly bound to the bilayer [16]. These results suggest a preferred cyt *c* orientation such that cyt *c* stably associates with the membrane, exposing a face to solvent that preferentially attracts MPA-AuNPs, and a potentially interfering role of anionic NPs in the regulatory membrane (dis)association of cyt *c*.

Here, we are interested in pursuing this question through a complementary approach by investigating the degree to which a membrane binding protein, cyt *c*, binds regiospecifically to the nanoparticle, rather than the bilayer. To this end, we will make reference to the binding sites [62, 63, 64] of cyt *c* to anionic cardiolipin-containing lipid domains: site N (Phe36, Gly37, Thr58, Trp59, Lys60), site A (Lys72, Lys73, Lys86, Lys87), site C (Asn52), and site L (Lys22, Lys25, His26, Lys27, His33). If there is to be binding between the three components–nanoparticle, cyt *c*, and the bilayer–then the exposure of cyt *c* to an NP would in turn also need to be preferentially oriented. Thus, the aim of this work is to interrogate the binding of cyt *c* to NP so as to establish the nature of their mutual binding interaction and its implications on three-body interactions, such as in the case of cyt *c*-assisted binding between NPs and a bilayer.

The MD simulations reveal the preferred non-rigid binding orientation of the peripheral membrane protein cyt *c* on anionic AuNPs that persists in the AuNP hard corona at long time-scales, as confirmed by mass spectrometry-based footprinting experiments. The combined bottom-up modeling and protein footprinting methodology also reveals the consequent corresponding solvent-accessible protein faces and amino acids. The latter are available to drive the acquisition of additional biomolecules in the formation of a soft corona [29, 30, 65, 66], and to preferentially bind to anionic membranes [16]. We thereby infer the possible preferred organizational structure of NP-cyt *c*-membrane complexes with biological implications due to potential NP interference in cyt *c* (dis)association from membranes which forms a prediction of this work. Our integrated approach can be applied to NPs and proteins, each with a broader range of surface chemistries, to develop a database and an associated set of design rules for the interaction between NPs and proteins, and represents an important strategy for the mapping of related systems.

3.2 Materials and Methods

3.2.1 Molecular Dynamics Simulations

To characterize the molecular interaction between cyt *c* (with structure 1AKK from the PDB) [67] and ligand-coated gold nanoparticles (AuNPs), several molecular dynamics (MD) simulations were performed with the two species in a large periodic box (Figure 3). The AuNP model consisted of a fully atomistic, 4 nm gold core of 2123 atoms with fully deprotonated mercaptopropionic (MPA) acid ligands grafted uniformly on the AuNP surface, following previous work [23], at a ligand density of 5.6 molecules nm^{-2} as determined by experiment [11]. The CHARMM36 force field was used for protein-AuNP simulations [68, 69]. Before the AuNPs and cyt *c* were combined into one simulation, we first performed separate equilibrations. The protein and AuNP were solvated in TIP3P water, neutralized, and ionized using sodium and chloride ions to below physiological salt concentrations (0.01 M). These systems first underwent an energy minimization for 200,000 steps using the conjugate gradient algorithm. Thereafter, the system was equilibrated for 1 ns under NPT (constant pressure and temperature) conditions using a standard numerical barostat and thermostat as described below. For the protein system, backbone atoms as well as the iron and surrounding nitrogens on the heme group were held fixed during the process. Meanwhile, the gold atoms were similarly constrained for the nanoparticle's NPT equilibration. The final coordinates from these simulations were the initial conditions for 1.6 ns NVT (constant volume and temperature) equilibrations. During these relaxations, the previously imposed constraints on the atoms were gradually released. Specifically, a constraint with a 10 kcal mol^{-1} Å^{-2} force constant was applied for the first 200 ps, followed by 200 ps with a 5 kcal mol^{-1} Å^{-2} constraint, and then 200 ps with a 1 kcal mol^{-1} Å^{-2} constraint. Finally, the system was allowed to equilibrate unconstrained for one 1 ns.

Once the protein and nanoparticle were equilibrated, the protein was placed in six different starting orientations with respect to the nanoparticle. By sampling all six of these orthogonally defined faces, we sampled the state space of possible orientations so as to obtain a statistically meaningful characterization of the relative preferred binding orientations. The center of mass of cyt *c* was held tangentially to the nanoparticle at a distance of approximately 30 Å. This initial placement was intended to increase the amount of protein surface area that is exposed to the nanoparticle, without overly biasing any particular binding site. The initial configurations were subsequently solvated with a 14 Å layer of TIP3P water. The nanoparticle and protein were placed along the longest diagonal of the simulation box with box volumes of approximately 1,000,000 Å^3 and average box length of 100 Å, which varied slightly depending on the dimensions of the protein configurations relative to the AuNP. These combined AuNP-cyt *c* systems were ionized and equilibrated using the same procedure as when they were equilibrated separately. After equilibration, 200 ns production runs with NVT conditions were used for data collection.

All simulations in this work were carried out using NAMD [70]. Particle Mesh Ewald (PME) with a 1.0 Å grid spacing was used to describe the electrostatics. Periodic boundary conditions and scaled 1-4 exclusions were also used throughout all simulations with a 12 Å pairwise-interaction cutoff and a switching function between 8 and 12 Å to address the nonbonded interactions. Additionally, all bonds were constrained using the SHAKE algorithm to allow for a 2 fs time step. Normally, long range electrostatics were only calculated every 10 fs, whereas short range nonbonded interactions were fully determined at every time step. However, when needed, the frequency of nonbonded force calculations was increased, or the time step was decreased, or both, during the equilibration steps to address errors within associated with the SHAKE algorithm. Temperature was kept at a constant 300 K using a Langevin thermostat. It had a 5 ps^{-1} damping constant and was not coupled to hydrogens. For NPT steps, pressure was maintained at 1 atmosphere using a Langevin piston, with a period of 100 fs and decay rate of 50 fs. Under these conditions, the simulation box was allowed to expand isotropically in all dimensions. No Langevin piston was used for NVT simulations, and the dimensions of the box did not change.

3.2.2 Protein Footprinting

Cyt *c* is first incubated for 18 h in the presence of 4 nm MPA-AuNPs or without. Next, N-acetoxy-succinimide is used in 10,000 molar excess of cyt *c* for lysine labeling for 1 min, at which point excess reagent is quenched with Tris. To recover the entire protein, the MPA-AuNPs are dissolved by treatment of the samples with KCN, washing the protein with 10,000 MWC filters, and evaporating them to dryness. Finally, the proteins are digested with chymotrypsin, and the resulting peptides are subjected to LC-MS/MS for percent lysine modification analysis and comparison.

3.3 Results and Discussion

3.3.1 Cytochrome *c* Structure and Orientation with Mercaptopropionic Acid (MPA)-Functionalized AuNPs (MPA-AuNPs)

Despite being perhaps the most thoroughly investigated peripheral membrane protein, the full characterization of the preferred binding of cyt *c* to arbitrary nanoscale constructs such as membranes or nanoparticles is incomplete. Absent crystal structures of cyt *c* bound to MPA-AuNP (which may not be possible because the binding may not be rigid), the precise site(s) or preferred binding orientation(s) on MPA-AuNPs can nevertheless be assessed *via* atomistic molecular dynamics (MD) simulations. Sites A, C, L, N (Figure 4), and several lysine residues have been implicated as possible candidates for the non-rigid binding site of cyt *c* to MPA-AuNP [60, 61, 71, 72, 73, 74, 75]. In our MD simulations, we focused on observables that characterize their relative positions. For simplicity, we labeled six opposing faces of cyt *c* by associating each with a plane of a cube, and arbitrarily chose face 1 to be one that was particularly electropositive. Specifically, the residues that are closest to this plane are Gly37, Arg38, Lys60, Glu61, Glu62, Lys99. The orientation around face 1 was constrained by choosing face 2 to be identified with Glu66, Glu69, Asn70, Lys73, Lys87, and Arg91. The remaining planes

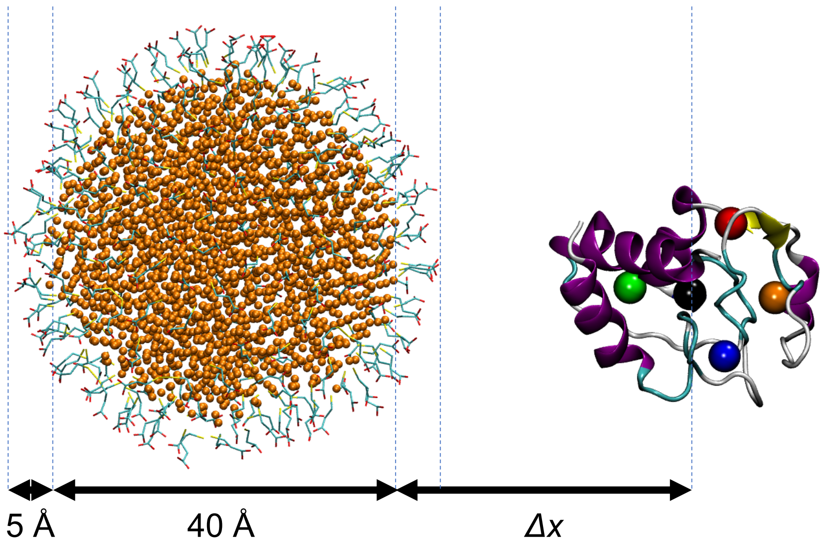

Figure 4: Representative initial orientation of cytochrome c (cyt c) near the 4 nm mercaptopropionic acid-functionalized AuNP (MPA-AuNP). The five centers of mass (COMs) on cyt c (shown to the right of the MPA-AuNP) used to monitor the distances Δx to the bare AuNP surface are color coded for site A (green), site C (orange), site L (blue), site N (red), and the cyt c (black) COM. In the MPA-AuNP, gold atoms are shown as orange beads, and the ligands are shown as a stick model highlighting sulfur atoms, oxygen atoms, and the carbon chains in yellow, red, and cyan, respectively. Note: the MPA ligand layer is 5 Å, and this distance can be subtracted from Δx to obtain distance from the ligand-coated AuNP surface.

were then associated as follows: Face 3 with Thr48, Thr49, Asp50, Ala51, Lys53, and Asn54; face 4 with Asp2, Val3, Glu4, Lys5, Lys7, and Lys8; face 5 with Glu21, Lys22, Gly23, Gly24, Lys25 and His26; and face 6 with Lys13, Gln16, Thr28, Lys72, Lys79, and Ile81. We ran six molecular dynamics trajectories, each with a different face of cyt c facing the MPA-AuNP as the starting orientation (Figure 5).

3.3.2 Relative Orientation of Cytochrome *c* in Close Proximity to MPA-AuNPs

The relative orientation of cyt c in each of the trajectories was tracked using the relative distance between the COMs of selected sites and the bare AuNP surface shown in Figure

4. The values of these figures of merit along the trajectories from a representative sample of initial orientations of cyt *c* are shown in Figure 6 and correspond to the structures shown in Figure 5. The steady descent of the cyt *c* COM towards the AuNP surface suggests non-rigid association of the protein with the AuNP. The three trajectories not shown here either had the cyt *c* effectively remain in the initial orientation (either near site A or site L), or did not quite relax to any structure within the 200 nanosecond simulation (Figs. A3.2, A3.3, A3.4 in the Appendix). The three shown here display relaxation from different orientations, and all three settle into configurations with either site A or L facing the MPA-AuNP, suggesting that they are the preferred non-rigid binding orientations. In some trajectories, cyt *c* reaches a minimum in which site

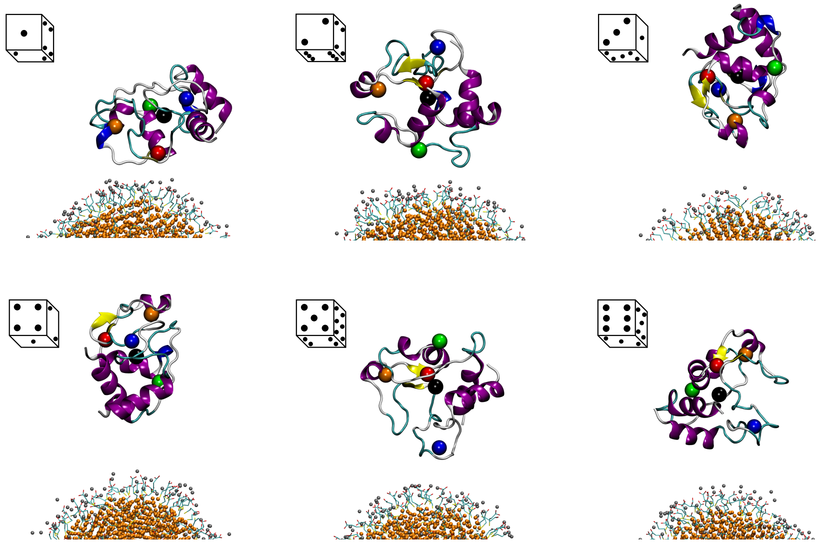

Figure 5: The starting orientations of cyt *c* around the MPA-AuNP for Trajectories 1-6, as labeled by the face of the protein and corresponding die shown coming out of the page to the reader. The face of the protein initially pointing towards the NP is indicated by the face of the bottom of the die. For example, trajectory 1 has face 2 initially pointing towards the NP, and that face can be seen from the initial structure of trajectory 2. The color scheme representing the COMs of the cyt *c* binding sites and the atoms and ligands on MPA-AuNP is the same as in Figure 4. Sodium ions are shown as gray beads.

L drives the binding but site A is not quite on the opposite end. Further detail on the orientation is captured in Figures 7 and 8, which show the distances from specific residues on sites A and L, respectively. Lysine residues that are within 10 Å of the AuNP surface suggest salt-bridge formation with the MPA ligand layer. In those trajectories which lead to structures with good overall binding for site A, residue K86 is closest to MPA-AuNP. This does not necessarily mean that the interaction between K86 and the NP is driving the binding because it is the totality of the interactions facing the NP for the preferred orientations of cyt *c* that drives the binding. However, the tendency for the proximity of K86 does suggest specificity in the relative orientation of the binding. That is, the contact is nearly centered at residue K86 for site A, whereas all of the residues associated with site L are in near proximity, including K22. Both of these sites are accessible through the footprinting methods being used experimentally in this work

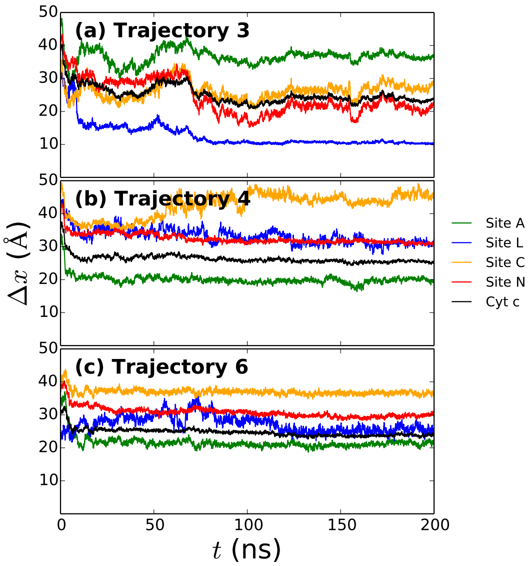

Figure 6: The distance Δx between the COM positions of the cyt *c* binding sites and the MPA-AuNP surface, as highlighted in Fig. 4, are monitored for trajectories 3, 4, and 6. The green, blue, orange, red, and black curves are the measured distances between the bare AuNP surface and the COM of site A, site L, site C, and site N or the cyt *c* COM, respectively.

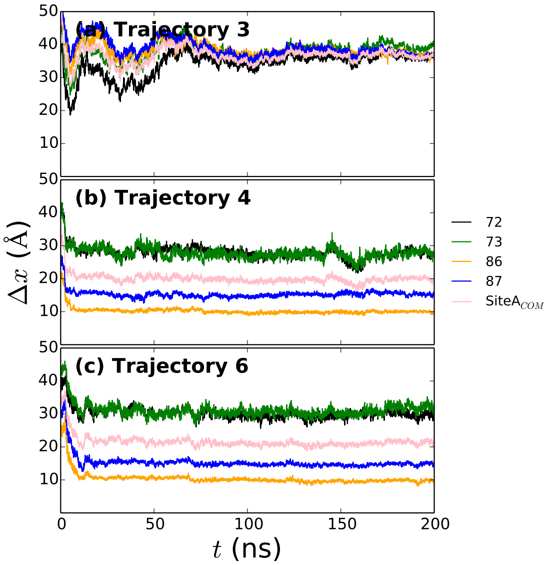

Figure 7: The distance Δx between the specific groups of amino acid–residues K72, K73, K86, and K87, and the COM of site A–in the anionic phospholipid binding site A of cyt c and the surface of the MPA-AuNP for trajectories 3, 4, and 6.

(*vide infra*).

3.3.3 Cytochrome *c* Secondary and Tertiary Structure Conformations

While the relative distance and orientation of cyt c to the MPA-AuNP surface were revealed through the simulations reported in the previous section, these do not clearly tell us which of the two local minima–with binding at sites A or L–is preferred. To help resolve this question, we monitored the radius of gyration as shown in Figures 9 and A3.5 and RMSD of cyt c as shown in Figure A3.6 throughout the 200 ns trajectories. As a control on the size of the protein, we ran a 200 ns trajectory of cyt c solvated by the same density of TIP3P waters as used in the protein-NP simulations, and provide those values in Figure A3.1. As seen there, the radius of gyration, R_g, of the free cyt c in solution is approximately 13.6 Å in agreement with the experimentally observed value at 13.5 Å [76]. The trajectories that bind to site L, such as that from trajectory

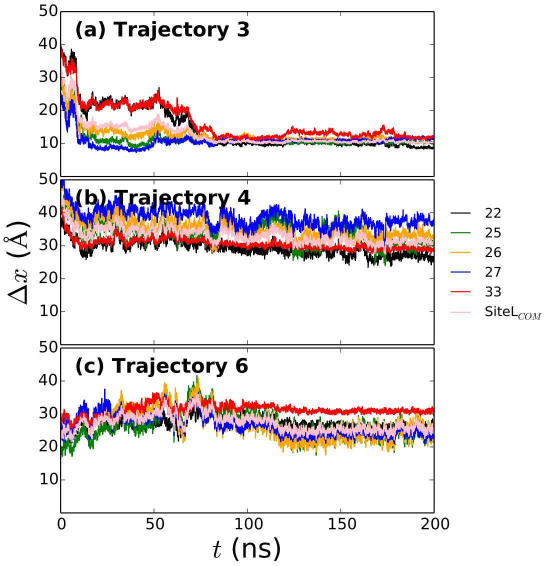

Figure 8: The distance Δx between the specific groups of amino acids–residues K22, K25, K26, K27 and K33, and the COM of site L–in the anionic phospholipid binding site L of cyt c and the surface of the MPA-AuNP for trajectories 3, 4, and 6.

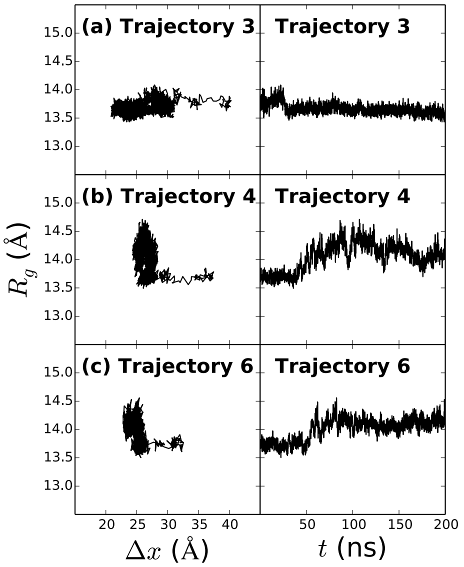

Figure 9: The radius of gyration R_g of cyt c *vs.* time along each 200 ns MD trajectory (right panels) as a function of the distance Δx between the cyt c COM and the surface of the MPA-AuNP (left panels).

3 (Figs. 6a and 8a), remain at R_g values comparable to that of the free protein. On the other hand, in the case of the structures binding at site A (from trajectories 4 and 6; Figs. 6b,c and 7b,c), both the R_g and RMSD increase as cyt *c* approaches the MPA-AuNP, suggesting the proteins open up in response to an interaction with the MPA-AuNP. This further suggests that non-rigid binding at site A may be strengthened by internal energy changes (which compensate for the internal restructuring), while the non-rigid binding at site L is driven by entropic considerations (which permit a large set of orientations to be stable.) This finding in the simulations agrees with the experimental observations in that both sites are found to have some degree of non-rigid binding, and the specific sites exposed to solvent in the final configurations seen here correspond to those seen to be available in the footprinting results (*vide infra*). In all trajectories, the RMSD values for the heme group remain nearly constant throughout the trajectory, and the heme group is not directly involved in binding, as previously shown in simulations of cyt *c* on Ag surfaces [75].

3.3.4 Cytochrome *c* Circular Dichroism

The secondary and tertiary structure of both free cyt *c* in water and cyt *c* adsorbed on MPA-AuNPs were examined by circular dichroism (CD) [77]. The far-UV CD spectra of free cyt *c* has two negative peaks at 208 and 222 nm, corresponding to the helical character of the protein (Figure 10) [78]. The ratio of the 222 nm and 208 nm signal can be utilized to evaluate the α-helices of proteins [79]. Canonical α-helices have an expected range of 1.25-1.75 [80]. The 222/208 nm ratio is 1.72 in free cyt *c* and corresponds to reported CD spectra of cyt *c* [81, 82, 83, 84, 85]. In comparison, while cyt *c* incubated with MPA-AuNPs exhibits minima at the same wavelengths, the global minimum has switched from 222 nm to 208 nm, resulting in a lowered 222/208 nm ratio of 0.77. A similar shift, while not as pronounced, has been observed in studies of cyt *c* adsorbed to multiwall carbon nanotubes and glutathione-capped AuNPs [81, 82, 83, 84, 85].

To estimate the percent composition of secondary structures, the CD spectra were further deconvoluted using CONTIN (Figure 11) [86]. The regular α-helix composition decreased upon adsorption to MPA-AuNPs (28% versus 17%). A corresponding increase was calculated in the content of distorted α-helix structures (8% versus 12%) and regular α-sheet content (3% versus 12%). Increase in α-sheet composition of cyt *c* has been reported to correlate to conformational changes, which increase exposure of the heme site [87]. Taken in combination with the protein deformation observed in the MD simulations (*vide supra*), the secondary and tertiary structure of cyt *c* are distorted upon interaction with MPA-AuNPs.

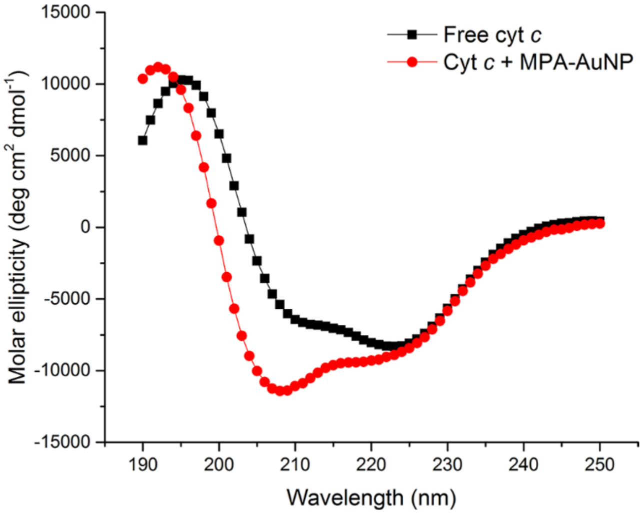

Figure 10: Circular dichroism spectra for cyt *c* free and incubated with MPA-AuNPs. The CD spectra of free cyt *c*, 4 μM in H_2O, is shown in black and cyt *c* + MPA-AuNP (18 nM) is shown in red.

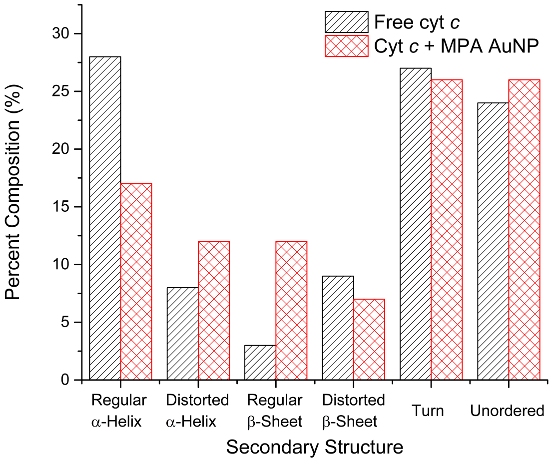

Figure 11: Secondary structure calculations. Contributions to cyt c secondary structure were determined by fitting CD spectra using CONTIN. Contributions from regular α-helix, distorted α-helix, regular β-sheet, distorted β-sheet, turn, and unordered are shown in black for free cyt c and red for cyt c incubated with MPA-AuNP.

3.3.5 Cytochrome *c* Lysine-Specific Protein Footprinting

The binding sites indicated to be important for particle interaction by the MD simulations are all lysine-based. Previous studies of cyt c-nanoparticle systems have identified that the electrostatic interaction of lysine residues with negatively charged ligands is important [55, 57, 75, 81, 82, 83, 84]. In addition, lysine residues have been found to have a higher propensity to penetrate the NP surface-bound water layer due to their flexible side chain, thereby facilitating binding [75]. Dordick and co-workers determined site A preferentially interacted with 4 and 15 nm silica NP [55] . However, in a previous report Dordick and co-workers did not observe a change in cyt c structure upon adsorption to 4 nm silica NPs, but did for larger NPs [82]. The preferential binding of both sites A and L in cyt c observed in our simulations and the deformations observed by both simulation and CD experiments suggest that the binding interactions are likely not the same with 4 nm MPA-AuNPs.

To interrogate preferential binding, we utilized lysine-specific protein footprinting [53]. This strategy enables the identification of lysine residues that are differentially accessible in the native *versus* nanoparticle-bound forms of cyt *c*. This is accomplished by acetylation of only solvent accessible residues followed by characterization of the extent to which each lysine is modified using mass spectrometry-based methods. Chymotrypic digests of labeled cyt *c* and of labeled cyt *c* from complexes with MPA-AuNPs were subjected to nanoLC-MS/MS for peptide mapping. There was a decrease in modification upon incubation with MPA-AuNPs for all three lysine residues in site L (Figure 12: K22, K25, K27), in addition to K86 of site A and K79, indicating decreased solvent accessibility either due to particle binding or protein deformation. On the other hand,

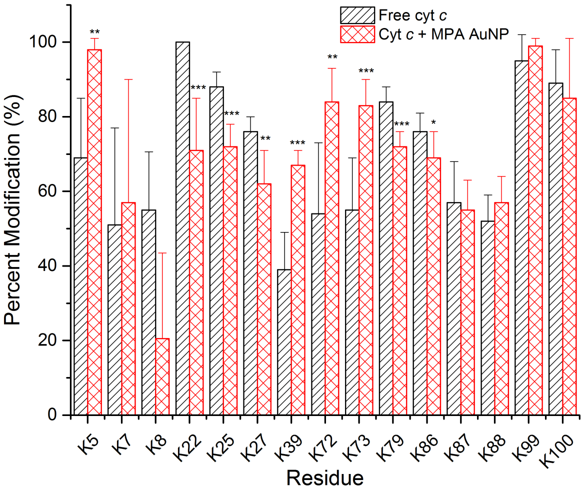

Figure 12: Degree of lysine modification determined by nanoLC-MS/MS. Site L (K22, K25, K27) exhibits a decrease in acetylation when incubated with MPA- AuNPs (red) compared to free cyt *c* (black) as do K86 of site A and K79. Site A exhibits an increase in labeling at lysines 73 and 74, as well as K5 and K39, upon incubation with MPA-AuNPs. Error bars represent the standard error of three independent experiments. Included spectral data had peptide identification with $p < 0.01$ and modification site identification with $p < 0.01$. Statistical analysis was performed with non-parametric one-way ANOVA ($\alpha = 0.05$; $***p < 0.001$; $**p < 0.01$; $*p < 0.05$).

two lysine residues in site A (K72 and K73), as well as K39 exhibited an increase in acetylation, and therefore solvent accessibility, suggesting they are not integral in the interaction of cyt *c* with 4 nm MPA-coated AuNP. This also implies that these residues may become more solvent exposed due to protein deformation on the NP surface. Examination of the location of the lysine residues–illustrated in Figure 13–with decreased acetylation upon interaction with MPA-AuNP reveals that they are close in space. Nakano and co-workers have previously identified K13, K25, K27, K79, and K86–of which K25 and K27 are associated with site L and K86 is associated with site A–as the probable interaction site of cyt *c* with 11-mercaptoundecanoic acid coated Au surfaces [88], in line with our results indicating that the lysine residues of site L, as well as K79 and K86, preferentially interact with the MPA-AuNP.

Figure 14 summarizes the collective findings between the experiments and simulations. Two of the putative binding sites to cardiolipin, sites A and L, are seen to have some degree of preferred non-rigid binding to MPA-AuNP. Neither subspace of structures is perfectly aligned with the corresponding cardiolipin binding site because not all of a given site's residues are in proximity to MPA-AuNP at equilibrium. The poses that they take on are aligned, and exhibit similar orientation between simulation and experiment in so far as the lysine residues that are seen to be exposed or not exposed in the experiment are commensurate with the poses from the simulation. In these two orientations, the residues of sites A and L become less solvent accessible by either facing the MPA-AuNP surface or neighboring cyt *c* in the protein corona.

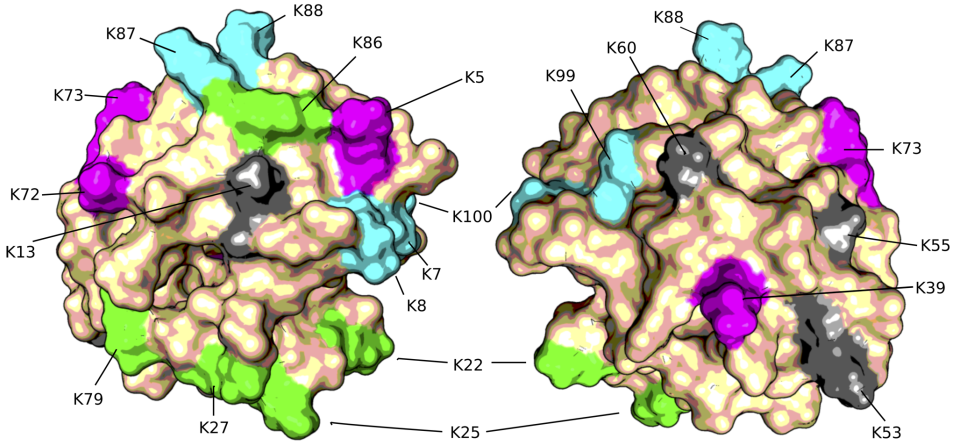

Figure 13: Horse heart cyt *c* (1AKK). Lysines K5, K72, K73, and K39 had an increase in percent modification upon MPA-AuNP incubation (magenta). Lysines K22, K25, K27, K79, and K86 had a decrease in percent modification upon MPA-AuNP incubation (green). Lysines K7, K8, K60, K87, K88, K99, and K100 had no change in percent modification (cyan). Lysines K13, K60, and K53 were not detected by LC-MS/MS (gray).

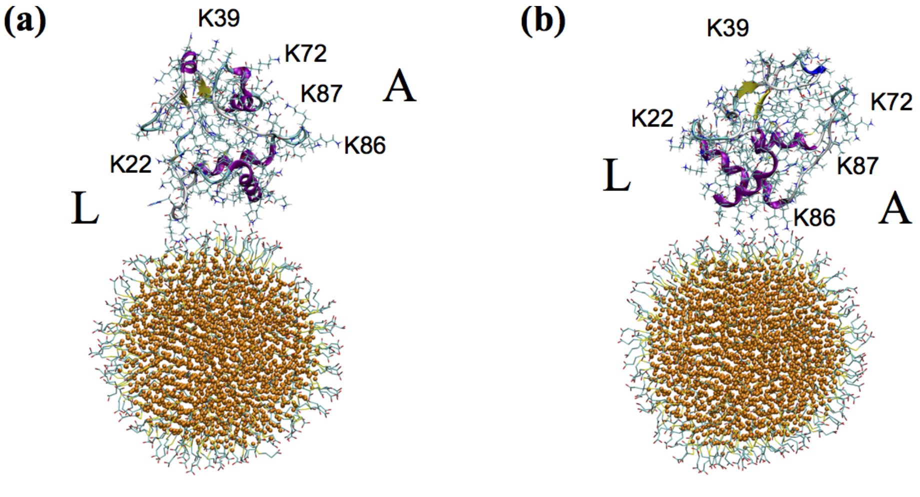

Figure 14: Two possible orientations of cyt *c* non-rigidly bound to MPA-AuNP consistent with the simulations and experiments are shown here: (a) K22 (in site L) and K86 and 87 (both in site A) facing the NP, and (b) K86 and K87 (both in site A) and K22 (in site L) facing the NP. In both orientations, K39 and K72 (in site A) are opposite to the MPA-AuNP and the most solvent accessible. K86 is closer to the MPA-AuNP surface than K87, making it less solvent accessible, in agreement with footprinting experiments.

3.4 Conclusion

A central tenet of this work has been the advantages for combining experimental footprinting and computational molecular dynamics methods to efficiently converge on an optimal binding structure in long-lived hard coronas [89] even when binding is not fully specific or rigid. This was shown through the particular interaction between cyt *c* and 4 nm MPA-AuNPs, but the overall tandem strategy is general and represents a promising approach to quickly identify and verify potential binding regions. It can be used, for example, to probe preferential binding orientation and deformability of proteins in a NP size-dependent manner, as previously observed by simulations and experiments [34, 90, 91]. A key aspect to the success of the footprinting was the confirmation, suggested by the simulations, that lysine residues can be used as reporters for determining the possible poses of cyt *c* in relation to MPA-AuNP. Similarly, the results of the footprinting, in supporting the MD simulations, removed the need for determining a larger number of trajectories so as to reduce the error from the ensemble averaging of trajectories that would have come at large computational cost.

Previously, we observed a preferred binding site of cyt *c* on anionic lipid domains and the binding of MPA-AuNPs to membranes proportional to the number of cyt *c* on the membrane, using MD simulations and quartz crystal microbalance with dissipation monitoring experiments, respectively [16]. Through MD simulations and protein footprinting in this work, we show that cyt *c* can adopt two different but specific orientations in non-rigidly binding to MPA-AuNP. The solvent-exposed faces resulting from the preferred orientations of cyt *c* on membranes are thus available for cyt *c* to bind to MPA-AuNPs if that process is additive. Thus, protein footprinting and MD simulations of peripheral membrane proteins adsorbed onto NPs provide a critical component to understand the role of cyt *c* in facilitating the binding of NPs to membranes. Given the technical challenges of exploring this three-way interaction, our ability to make these connections through pairwise studies is of particular significance. More generally, this combination of experimental and computational tools will find broad utility for the exploration of many pairwise and multi-component interactions to investigate mechanisms of protein corona formation and potentially, predict particle toxicity by the structure and reactivity of its corona.

Chapter 4

The Effect of Surface Curvature and Ligand Structure on Ligand Environment in Self-Assembled Monolayers on Gold Nanoparticles

4.1 Introduction

The molecular composition and conformation of the ligand shell are crucial to the chemical and biological behavior of the nanoparticles [92]. Thiolated ligands are known to bind strongly to gold nanoparticles (AuNPs) and form self-assembled monolayers (SAMs), which impart colloidal stability and desired functionality to the nanoparticles [93]. Surface functionality of SAMs on AuNPs also plays an important role in nanoparticle cytotoxicity [94]. Spectroscopy and microscopy techniques, including UV-Vis [95], FTIR [96], XPS [40, 96], TEM [97], and STM [98], have been explored to investigate the chemical environment of SAMs on AuNPs. However, the determination of the ligand conformation at the molecular level is still challenging [99].

Nuclear Magnetic Resonance (NMR)-based approaches provide great potential in elucidating the surface chemistry of ligand shells on nanoparticles in solution [100].

NMR has been used previously to investigate ligand shells on nanoparticles, to discriminate between bound and free ligands, to identify and quantify bound ligands, and to understand the binding mode of ligands and their dynamics [97, 101, 102, 103, 104, 105, 106]. The majority of the reported NMR studies on small molecule SAMs on AuNPs have been limited to isotropic spherical nanoparticles, or gold nanospheres (AuNSs), with diameters less than 6 nm. This is partly due to the relative low sensitivity of NMR, which requires a very concentrated nanoparticle sample. Typical AuNP colloidal solutions, for instance, are nM to μM in particles, and the concentration limit for the larger nanoparticles is inherently lower because of their larger volumes. Moreover, ligands that are associated with larger nanoparticles experience significant line broadening, which can obscure peak assignments and integration.

To overcome the aforementioned problems of using NMR to study ligand environment on larger nanoparticles, we synthesized (16-mercaptohexadecyl)trimethylammonium bromide (MTAB) and used MTAB SAMs on AuNSs (MTAB-AuNSs) as a model for solution NMR analysis (Figure 15). MTAB-AuNSs are very stable in aqueous solution at very high particle concentrations, allowing the low sensitivity of NMR to be overcome [107]. The protons in the trimethylammonium headgroups that are exposed to the solvent are the most mobile protons in the ligand, which makes them suffer the least from line broadening [107]. Furthermore, their chemical shift is ∼2 ppm away from that of the interfering protons in the methylene main chain. Taken together, we choose these protons to infer ligand packing, mobility, and conformation.

It is known that the conformation of SAMs on AuNSs less than 5 nm is highly dependent on the nanoparticle size and the surface curvature [108]. To further

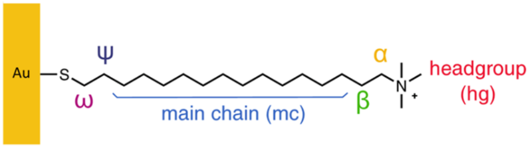

Figure 15: A cartoon of the MTAB monolayer binding to a gold surface.

investigate the role of surface curvature on the ligand environment, and to examine the upper limit of the nanoparticle size that is suitable for NMR analysis, MTAB-AuNSs of sizes ranging from 1.4 nm to 25 nm were synthesized and analyzed by solution NMR. We used complementary MD simulations to investigate (11-mercaptoundecyl) trimethylammonium bromide (MUTAB), an analog of MTAB, on 4, 6 and 8 nm MTAB-AuNSs at different ligand densities. These simulations provide exquisite detail on the typical positions of the ligands at each of these three diameter sizes. Indeed, the NMR determined ligand packing order and headgroup mobility are seen to be commensurate with the structuring of the ligands seen in the MD simulations.

4.2 Materials and Methods

4.2.1 Molecular Dynamics Simulations

Computational structures of AuNSs at sizes 4, 6, 8 nm in diameter were constructed through a sequence of steps: placing gold atoms at least four atomic radii apart within a sphere, heating the system to 1400 K, slowly cooling to 300 K, and equilibrating at 300 K. We used (11-mercaptoundecyl)trimethylammonium bromide (MUTAB) as a simplified model for MTAB. The OPLS-AA force field [109] is used to model the interactions of MUTAB ligands. Previous simulation studies of SAMs on gold surfaces with chain lengths in the range of 9-20 carbons have shown that the hydrophobic chain packing dominates the structure with a negligible effect of the headgroup chemistry on the positioning of headgroups [110, 111]. The interaction between the gold atoms is modeled using a Lennard-Jones potential initially with the parameters specified by Heinz and co-workers [112]. The Lennard-Jones parameters for the interaction potential between gold atoms employed in simulations of MUTAB functionalization onto gold were subsequently adjusted so that the gold-carbon parameters, after applying geometric mixing rules, fit those developed by Landman and co-workers to model alkane adsorption onto gold surfaces [113]. The adjusted parameter for ε_{Au-Au} is 1.55 kcal/mol and for ε_{Au-Au} is 2.629 Å.

To simulate ligand attachment, a Morse potential was used for the interaction between sulfur and gold atoms, using the parameterization of Ghorai and Glotzer [110]. MUTAB ligands were placed with sulfur atoms near the AuNS surface with the AuNS fixed at the center of the simulation box, and simulations were run for 0.1 ns at 300 K. We subsequently defined harmonic bonds between sulfur atoms and their nearest gold atoms. The system was equilibrated for 2 ns at 300 K, and then heated for 3 ns at 400 K, following the protocol of Luedtke and Landman [114]. The system was re-equilibrated for 10 ns at 300 K and until a convergence in the average tilt angle of ligands was reached (Figure A4.1 in the Appendix). Production simulations for an additional 10 ns were then run to obtain data for analysis with samples collected once every picosecond.

Packmol [115] was used to construct initial configurations for AuNS synthesis and to distribute MUTAB ligands on the AuNS surface at 4.0 and 6.0 molecules per nm^2 densities. All simulations were propagated using LAMMPS [116] at 2 fs per timestep. Periodic boundary conditions were employed with a 10 Å cutoff for pairwise interactions at constant NVE condition–that is, number of atoms N, volume V, and energy E. A Langevin thermostat with a damping constant of 10 ps^{-1} provided energy dissipation and maintained the average energy vis-à-vis effective temperature. The particle-particle particle-mesh (PPPM) method was used to calculate electrostatic interactions with explicit bromide counterions included to neutralize each ligand. The relative permittivity was set to 80.1 so as to represent water. Box sizes were chosen so that the total bromide concentration was 0.136 M.

4.2.2 MTAB-AuNP Synthesis and Characterization

In a typical synthesis, citrate- or CTAB-stabilized gold nanoparticles are first synthesized and then MTAB ligands are exchanged at elevated temperature in excess. After synthesis, nanoparticles were characterized by UV-Vis spectroscopy, dynamic light scattering (DLS), zeta potential analysis, and transmission electron microscopy (TEM). Concentrations were determined according to published UV-Vis extinction coefficients [117]. Inductively coupled plasma mass spectrometry (ICP-MS) was used to determine the gold concentration of digested samples. Nuclear magnetic resonance (NMR) spectra were acquired using a Varian Unity Inova narrow-bore 500 MHz (UI500NB) spectrometer and Varian Unity Inova narrow-bore 750 MHz (VNS750NB) spectrometer (Varian Inc.) at 298.15 K. Spectra were processed with MNova (Mestrelab Research). Chemical shifts are reported in parts per million (ppm) and are referenced to the residual proton solvent peak. For quantitative NMR analysis, a known amount of maleic acid (with D_2O as solvent) or benzoic acid (with $CDCl_3$ as solvent) was added as internal standard and peak integrations were compared to this internal standard.

4.3 Results

4.3.1 NMR Chemical Shifts

Chemical shifts of the headgroup proton signals depend on the size of the AuNSs (Figure 16). The chemical shift of the headgroup protons in the free MTAB ligands is 2.99 ppm. We observe a gradual downfield shift in the headgroup proton signals from 3.05 ppm to 3.23 ppm as the size of the nanospheres increases from 1.2 nm to 10.8 nm. Then, the chemical shift plateaus after the size of AuNSs reach beyond 10.8 nm. The chemical shift of thiol ligands is known to be not only determined by their chemical structures but also by their neighboring ligands [98]. For a single moiety ligand shell such as MTAB, the chemical shift of headgroup protons is dependent on the MTAB packing density: the number and/or distance of neighboring positively charged headgroups affect the electron density of headgroup protons. The trend in chemical shift is similar to what is observed for the MTAB analog CTAB as a function of concentration: as CTAB transition from single molecules to premicelles, to spherical micelles, and finally to rod-shaped micelles in water upon increasing concentration, the headgroup proton signals shift downfield from 2.98 ppm to 3.11 ppm [118]. For MTAB on AuNSs, the similar trend in chemical shift from 2.99 ppm to 3.23 ppm suggests that MTAB packing density increases as particle size increases, up to 10.8 nm. Beyond 10.8 nm, MTAB headgroups are saturated on the gold nanoparticle surface. The headgroups might form a more ordered structure on the particle surface compared to CTAB micelles.

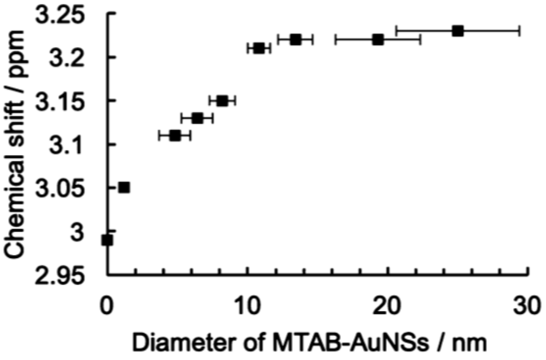

Figure 16: Dependence of the chemical shift of the headgroup protons of bound MTAB as a function of AuNS diameter. Error bars for chemical shifts are smaller than the squares. Free MTAB is at 0 diameter.

4.3.2 Ligand Density of MTAB on AuNPs

Since the headgroup protons can be fully detected by ^{1}H NMR for sizes up to 25 nm, we can potentially use the headgroup proton peaks as a probe to quantify the ligands on nanoparticles by quantitative ^{1}H NMR analysis using an internal standard. Maleic acid was used as an internal standard because its proton signals do not overlap with the MTAB headgroup protons, and it does not interact with MTAB ligands.

One might argue that since the headgroup proton peaks are broad, the processing of the NMR spectra such as baseline correction and peak fitting may cause integration errors. Therefore, we also used an indirect method to quantify the ligand density. I_2/I^- was used to etch the gold core in MTAB-AuNSs and release the surface-bound MTAB ligands. Since MTAB and its disulfide do not dissolve in water under room temperature after being released, $CHCl_3$ was used to extract the released the ligands. We found that no more free ligands can be extracted after 48 hours of reaction. Benzoic acid was used as an internal standard because its proton signals do not overlap with the MTAB headgroup protons, and it does not interact with MTAB ligands.

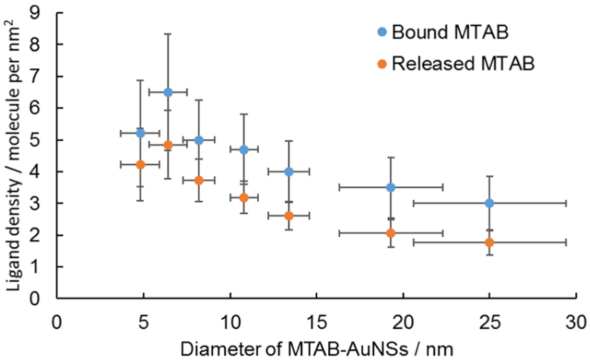

Figure 17: Dependence of ligand density of the headgroup protons of bound MTAB as a function of AuNS diameter. Blue dots: Data from *in situ* quantitative NMR integration relative to a maleic acid internal standard. Orange dots: Data from experiments in which the gold was digested and free ligands were quantified after purification relative to a benzoic acid internal standard.

Figure 17 shows the relationship between the ligand density and the sizes of the nanospheres. The error bars in Figure 17 combine that of particle size heterogeneity from TEM, gold content quantification from ICP-MS measurement, and the ligand quantification from quantitative NMR. The MTAB ligand density is size dependent from both methods: the ligand density decreases as the size of the nanoparticles increases, from ∼5-6 MTAB molecules per nm^2 to ∼3 MTAB molecules per nm^2 if we directly quantify the bound MTAB ligands, or from ∼4-5 MTAB molecules per nm^2 to ∼2 molecules per nm^2 if we quantify the released MTAB ligands after I_2/I^- treatment, as nanosphere size increases from 4.8 nm to 25.0 nm.

4.3.3 Molecular Dynamics Simulations of MUTAB-AuNPs

We used molecular dynamics (MD) simulations to study the structure of the MUTAB ligand layer on 4, 6, and 8 nm AuNSs at ligand densities of 4.0 and 6.0 molecules per nm^2–the minimum and maximum in the range of ligand densities determined for 4 and 8 nm AuNSs (Figure 17). Representative images of MUTAB-AuNSs show that MUTAB

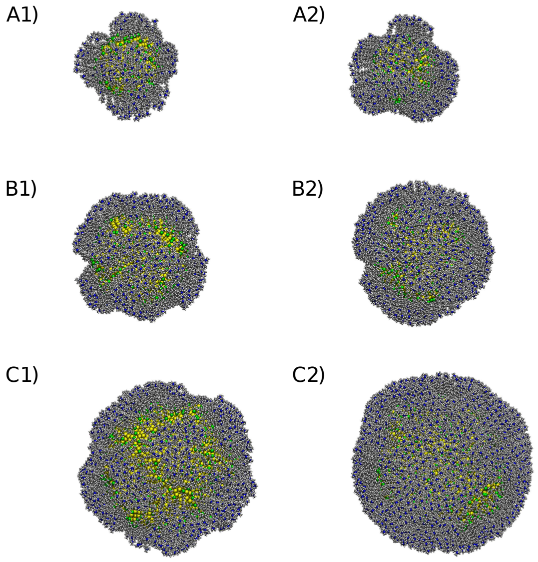

Figure 18: Simulation snapshots of MUTAB-AuNSs with the following size and ligand density: Rows A, B and C correspond to 4 nm, 6 nm, and 8 nm diameters, respectively; and Columns 1 and 2 correspond to 4.0 molecules nm^{-2} and 6.0 molecules nm^{-2} ligand densities. Gold atoms are shown in yellow, sulfur in green, carbon in gray, hydrogen in white, and nitrogen in blue. Bromide counterions are removed for clarity.

forms islands on the nanoparticle surface (Figure 18). The formation of ligand islands is attributed to the competition between hydrophobic chain packing and the free volume in space available per ligand particularly at high surface curvatures [110, 111, 119]. To quantify the structural changes in the MUTAB layer as a function of AuNS size and ligand density, we calculated the radial distribution function, *g(r)*, between the AuNS center of mass and nitrogen atoms in the headgroup of MUTAB (Figure 19) and the *g(r)* between all pairs of nitrogen atoms (Figure 20). The *g(r)*'s were obtained using histograms with bin sizes of 0.1 Å averaged over 5000 frames per trajectory for five trajectories per AuNS size and ligand density and normalized by the annular volume. The *g(r)*'s for individual trajectories are available in the Appendix (Figs. A4.2 and A4.3).

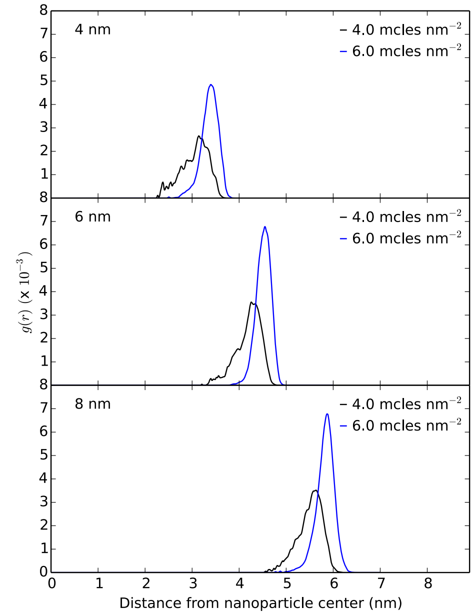

Figure 19: Radial distribution function, *g(r)*, between the nanoparticle center of mass for 4, 6, and 8 nm AuNSs and the nitrogen atoms of MUTAB at ligand densities of 4.0 and 6.0 MUTAB molecules nm^{-2}.

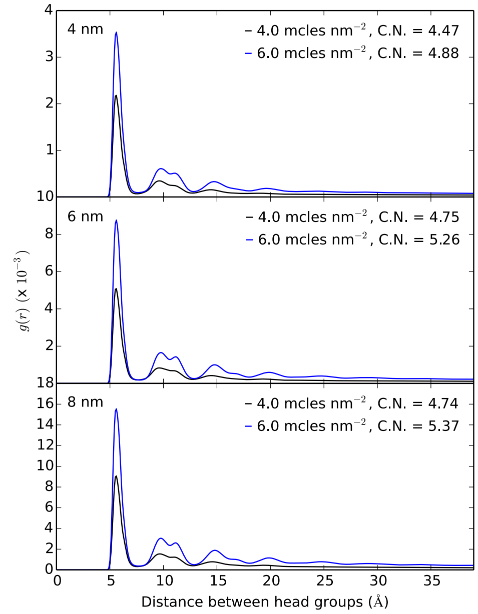

Figure 20: Radial distribution function, *g(r)*, between all pairs of nitrogen atoms in the headgroup of MUTAB at ligand densities of 4.0 and 6.0 MUTAB molecules nm^{-2}. The coordination number (C.N.) of MUTAB headgroups is determined by taking the integral under the first peak in each *g(r)*.

At a ligand density of 4.0 molecules nm^{-2}, the *g(r)* between the AuNS center and MUTAB headgroups for 4 nm AuNSs shows peaks that appear near the surface (Figure 19). This suggests that a significant number of ligands lie along the AuNS surface. As the AuNS size increases and curvature decreases, there are fewer ligands lying on the nanoparticle surface, as shown by the disappearance of the peaks near the surface, designated as 2 nm, 3 nm, and 4 nm from the nanoparticle center for 4, 6, and 8 nm AuNSs, respectively (Figure 19). The hump between peaks at the surface and the major peak also disappears as the nanoparticle size increases. The greater spatial distribution of MUTAB headgroups on smaller AuNSs is attributed to an increase in chain packing disorder due to greater free volume per ligand [120] and the greater tilt of chains particularly on the edges of the ligand islands as ligands pack along AuNSs of higher surface curvature [110, 119]. Further, the disappearance of the hump and the increase in magnitude of the major peak suggest that MUTAB ligands on 8 nm AuNSs are more ordered, standing more upright with decreased tilt due to greater hydrophobic chain packing on the nanoparticle surface. At a higher ligand density of 6.0 molecules nm^{-2}, the *g(r)* between the AuNS center and MUTAB headgroups reveals a single major peak for all AuNS sizes (Figure 19). The *g(r)*'s show a more pronounced tail near the surface of 4 nm AuNSs and sharper peaks for the larger AuNSs, signifying greater chain packing order at lower surface curvatures and higher ligand densities.

Measuring the distance between all pairs of nitrogen atoms, we find that the nearest neighbor for each MUTAB headgroup is 5.4 Å away independent of AuNS size and ligand density (Figure 20). The coordination number of each headgroup increases and approaches the hexagonal packing limit of 6.0 with both increasing AuNS size and ligand density. Figures 19 and 20 combined suggest that for smaller AuNSs and at lower ligand densities, there is a greater spatial distribution of headgroups relative to the AuNS surface with smaller coordination number per headgroup. For larger AuNSs and at higher ligand densities, a higher coordination number per charged headgroup and greater chain packing order lead to the accumulation of high charge density within the same spherical shell relative to the nanoparticle center, which could explain the downfield shifts in headgroup protons observed under such conditions by NMR experiments.

4.4 Discussion

The literature of self-assembled monolayers of thiols on gold is vast [93]. The majority of studies that focus on the details of ligand density and conformation are on flat gold surfaces or on colloidal AuNPs of less than ∼6 nm diameter. For instance, Häkkinen *et al.* interpreted the ^{1}H spectra of *p*-mercaptobenzoic acid capped 1.5 nm gold clusters in solution in terms of the special ligand environments on the cluster surface by multidimensional NMR, DFT calculations, and MD simulations [121]. Murray *et al.* investigated dodecanethiolate capped AuNPs of 1.5 to 5.2 nm in diameter by studying the methylene stretching modes in infrared spectroscopy (IR), and showed that ligands adopted a highly ordered conformation on ∼4 nm gold nanoparticles in the solid phase. They also analyzed gold nanoparticles by ^{1}H NMR and showed that NMR signals are broader as the diameter of the AuNPs increases from 1.5 nm to 5.2 nm, and the peak broadening causes difficulties in interpretation [108]. For particles larger than 5 nm, Castner *et al.* used ATR-FTIR to investigate the compactness of –COOH terminated SAMs on 14 nm, 25 nm, and 40 nm AuNPs in the solid phase, and showed that C_{16}COOH-SAMs are well-ordered on 14 nm gold nanoparticles [96]. To our knowledge, there are no reports of using NMR to study SAMs on AuNPs larger than ∼6 nm. The advantage of using solution-phase NMR for detailed ligand characterization is that measurements can be made *in situ* in aqueous solution, the most relevant environment for the many biological applications of these particles; the disadvantage is the low sensitivity of NMR [100].

To overcome the main disadvantage of NMR, colloidal AuNP solutions in this study were prepared at concentrations ∼100 times compared to those of typical measurements, without aggregation. The highly charged and somewhat bulky headgroups of the MTAB ligands helped contribute to this increase in colloidal stability as well as providing a convenient NMR handle (the solvent-accessible quaternary ammoniums).

For MTAB-AuNSs, the chemical shift analysis of the headgroups and ligand density analysis allow us to infer the packing of the headgroups and the sulfur atoms, respectively, in MTAB ligands when bound to AuNPs of various diameters. One key result is the ligand density and the packing of headgroups are not necessarily correlated. If we consider Figures 16 and 17, we learn that as the particle diameter increases, the chemical environment of the ligand headgroup more and more resembles, and may even pack denser than that of a well-packed micelle (Figure 16); yet the ligand density is largest for the smallest nanoparticles, and is smallest for the largest nanoparticles (Figure 17). We are forced to conclude, then, that for the smaller nanoparticles, the ligands must be more disordered and mobile. The experimental data agree well with the conclusions from the MD simulations reported above. The pair correlation functions, *g(r)*, in Figures 19 and 20 show that increasing the nanoparticle size leads both to increased ordering of the headgroups and decreased direct contact between the headgroups and the nanoparticle surface. The key result from the simulations, illustrated in Figure 18, is the existence of ligand islands with increased propensity in the smaller nanoparticles that leads to closer headgroup packing between proximal ligands than would be seen if they were uniformly distributed across the nanoparticle. The consensus interpretation from both the experiments and simulations is summarized in Figure 21, illustrating how the conformation of MTAB SAMs on AuNPs changes according to the nanoparticle size.

Ligand densities of MTAB on AuNSs of different diameters were quantified by NMR in two independent ways: direct peak integration, relative to a maleic acid standard, of bound ligands; and peak integration of released ligands after iodide etching of the gold cores, relative to a benzoic acid standard. The numerical values follow the same trend with size (Figure 17), but the averages differ by ∼30-50%, with the *in situ* measurements systematically larger than the digested values. This result might imply that digestion is not complete, or that the ligand losses in the purification process are considerable. Therefore, *in situ* measurements of nanoparticle-bound ligands, with an appropriate internal standard, might be preferable for quantification of ligand density for particles up to 25 nm in diameter.

There are many reports of ligand density on SAMs on AuNPs in the literature, using many different methods. Some reports suggest that ligand density is size-dependent, similar to what we found. As early as 1987, Nuzzo and Dubois *et al.* studied methanethiolate SAMs on Au(111) surface under ultra-high vacuum (UHV) conditions, and reported a surface coverage of 0.33, or a ligand density of 4.65 molecules per nm^2, by XPS [122]. Murray *et al.* studied dodecanethiol capped 2.4 nm gold nanoclusters, and found out that surface coverage is double this value (0.66), compared to ligands on flat Au(111) surface, combining SAXS and elemental analysis. Their analysis suggested that the high surface curvature relieves the steric crowding and/or the reactivity of Au atoms on the surface [108]. Mirkin *et al.* quantified thiolated oligonucleotides on AuNPs of 10 to 200 nm diameters by fluorescence. They also observed that smaller nanoparticle sizes exhibited larger ligand densities than larger particles, but the absolute values of ligand density are smaller than the ones we report here, due to large size of the oligonucletides [123].

Other reports, however, suggest that the ligand density on AuNPs is size-independent. Lämmerhofer *et al.* studied ligand coverage of C3, C11, C16 COOH-SAMs on AuNPs of 13 nm to 26 nm in diameter by plotting the ratio of gold to sulfur amount determined by ICP-MS to nanoparticle diameter. A linear relationship was observed, implying that the ligand density is size-independent [124]. Millstone *et al.* also analyzed the ligand density of C8 and C11 COOH terminated SAMs on AuNPs of 13 nm and 31 nm in diameter by using NMR to quantify digested ligands and ICP-MS to quantify gold content, and the results also suggest that ligand density is size-independent [125].

These apparently conflicting reports can be reconciled by considering the volume of the terminal headgroup on the SAM. The spherical volume occupied by sulfur, COO^-, and $N(CH_3)^{3+}$ is 7.24, 8.18, and 82.4 Å^3, respectively. For ligands with bulky headgroups and flexible linkers, such as MTAB and DNA, headgroup size controls ligand density. At small particle sizes, headgroup jamming is avoided by altered conformations at full ligand coverage, but at sufficiently large sizes where the headgroups are saturated on the ligand shells, headgroup sizes and surface curvature control ligand density (Figure 22). The computer images captured in Figure 18 and the statistically significant structure found through the radial distribution functions of Figure 20 reveal that MTAB headgroups transition from islands to uniform coverage with increasing ligand density, and the onset occurs at lower ligand density with increasing AuNSs size. For headgroups that have a similar or smaller size than sulfur bound to the gold surface, such as carboxylic acids, ligand density is size-independent (Figure 22).

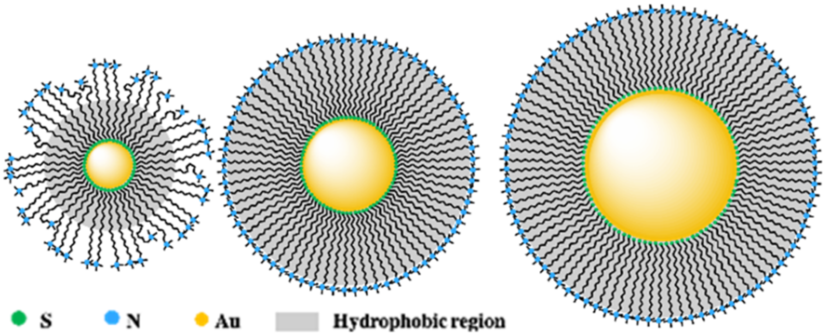

Figure 21: Scheme showing the MTAB conformation and packing as a function of nanoparticle size.

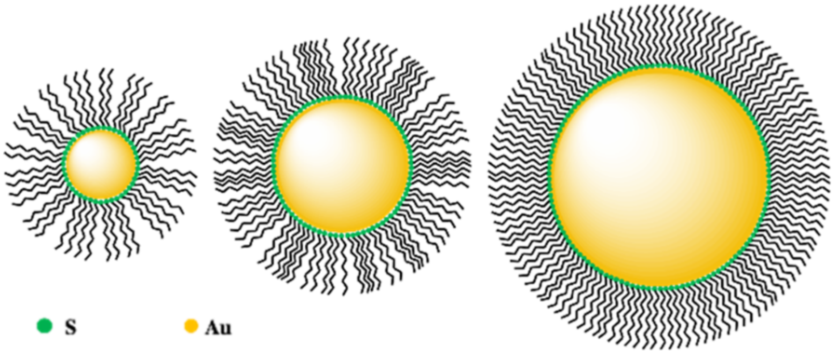

Figure 22: Scheme showing for ligands that have headgroups that are similar or smaller in size than sulfur, ligand density should be independent of particle size.

4.5 Conclusion

In this work, we have shown that solution NMR spectroscopy is a robust analytical tool for determining the structural conformation of the ligand shell of nanoparticles *in situ*. In parallel, molecular dynamics simulations provided an atomic resolution of the equilibrium structure and the transition of the ligand coverage from small to large diameter AuNSs. By studying the chemical shifts and ligand densities in concert with simulations, we are able to systematically demonstrate the ligand conformation of MTAB-AuNSs of sizes from 1.2 nm to 25 nm.

Chapter 5

Adsorption Dynamics and Structure of Polycations on Citrate-Coated Gold Nanoparticles

5.1 Introduction

Layer-by-layer assembly of oppositely charged polyelectrolytes onto the gold nanoparticle (AuNP) surfaces with molecular probes or small drug molecules embedded between layers allows for AuNPs to act as sensing [126], imaging [127], and drug-delivering agents [128, 129]. In addition to exhibiting a desired function or property, such particles increasingly must satisfy an additional figure of merit: they and their transformations in the environment must have zero or minimal impact on biological systems [6, 7]. As an example, AuNPs grafted with charged, long-chained alkanethiols have been seen in simulations to insert into and disrupt lipid membranes [130, 131, 132, 133, 134]. AuNPs coated with the cationic polyelectrolyte poly(allylamine hydrochloride) (PAH) are more prone to aggregation compared to alkanethiol-coated AuNPs despite having a higher surface charge density [11]. PAH-coated AuNPs (PAH-AuNPs) have also been shown to bind irreversibly to supported lipid bilayers [135] and exhibit greater toxicity to bacteria [11] and simple multicellular organisms [12, 136]. A better understanding of the polyelectrolyte-nanoparticle interface is therefore required to control the interactions of nanoparticles in the environment and thereby nanoparticle functionality and possible toxicity.

For polyelectrolyte-coated nanoparticles, many computational studies have focused largely on top-down models of polyelectrolytes of relatively short length, ranging from tens of monomers to a hundred, in which monomers are represented as single charged beads. Molecular dynamics simulations of top-down polyelectrolyte models have been used to characterize polyelectrolyte adsorption onto flat [137] and spherical surfaces [138, 139]. These simulations have shown that highly charged polyelectrolytes localize charge by distributing into multiple layers through the formation of loops and tails. Loops consist of free, solvent-exposed segments of polymers flanked by surface-bound segments referred to as trains. Tails form, if the ends of the polymer are free instead of surface bound. Nuclear magnetic resonance (NMR) spectroscopy of the polyelectrolyte PAH covalently grafted onto 5 nm nanodiamond similarly reveals both motion-restricted regions of PAH bound to the surface and highly mobile ones, suggesting the presence of loops and tails that extend into solution [102]. The heterogeneous spatial distribution of dynamic charged groups in polyelectrolyte-coated AuNPs could be a factor in why polyelectrolyte-coated AuNPs induce larger biological responses than alkanethiol-coated AuNPs.

Here, we perform atomistic molecular dynamics (MD) simulations of polyelectrolyte adsorption onto AuNPs to reveal other chemical properties at the atomistic level in addition to charge distribution that need to be represented in coarse-grained models. A combination of implicit- and explicit-solvent simulations is used to study the adsorption dynamics, surface coverage, and structure of PAH on AuNPs. Specifically, we deposit PAH such that the end-to-end vector of the polyelectrolyte is normal to the AuNP surface. We observe the relaxation and equilibrium behavior of a finite number of trajectories of this system, both in implicit and explicit solvents. Although the set is not enough to have complete representation of the ensemble, this finite poll exhibits a range of behaviors providing a view of the end-to-end adsorption and resulting structure of longer-length polyelectrolytes on AuNPs. Geiger and co-workers determined that the average number of ammonium groups per PAH adsorbed onto 4 nm citrate-coated AuNPs is 200 [39]. We therefore deposit PAH of 200 monomers (PAH_{200}) on a 4 nm citrate-coated AuNP in simulations. Although both experiment and simulation have shown preferential binding of ligands, specifically citrate and poly(vinylpyrrolidone), on different facets of gold [42] and silver nanoparticles [140, 141], respectively, here we study the simpler case of a homogeneously covered citrate-coated AuNP along with fully protonated PAH_{200} (Figure 23). Both experimental and computational studies [142, 143] have also shown that protonation levels of PAH can vary from 0.14 in neutral pH solution to 0.70 at charged lipid-membrane interfaces due to local pH effects. The use of a fully protonated PAH_{200} in our all-atom model allows for direct comparison to top-down, coarse-grained models of fully charged polyelectrolytes and serves as a benchmark for future coarse-grained simulations investigating how variation in protonation states and sites along longer-length polyelectrolytes affects polyelectrolyte conformation and surface coverage on AuNPs. Further, the results are useful in identifying reduced dimensional variables and observables that would be relevant for a new bottom-up coarse-grained approach for polyelectrolyte-coated AuNPs of possible use in simulating both the polyelectrolyte-AuNP interface and the nano-bio interface.

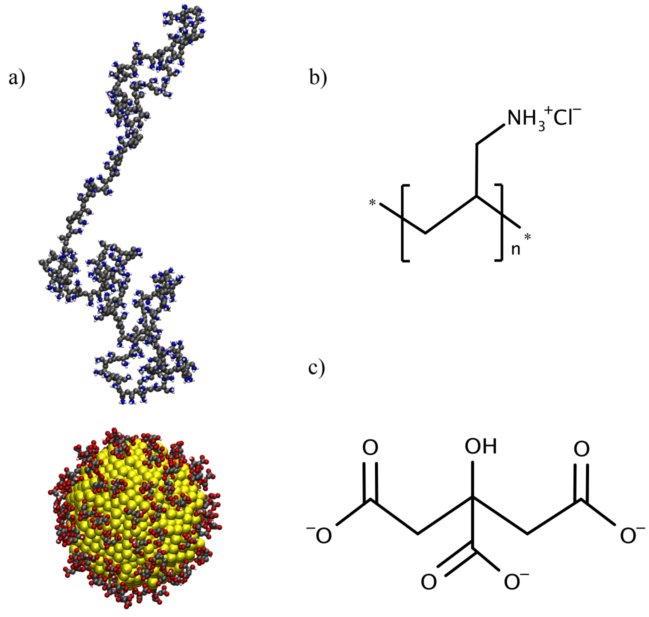

Figure 23: Representative structures for (a) the initial configuration for PAH_{200} deposition on citrate-coated AuNPs with gold (yellow), carbon (gray), oxygen (red), hydrogen (white), and nitrogen (blue) atoms (and counterions not shown for clarity); (b) a PAH monomer; and (c) $citrate^{3-}$.

In this chapter, we report the development of our all-atom 4 nm PAH-AuNP model from the construction of a 4 nm AuNP and the adsorption of the negatively charged citrate layer to the adsorption of the polycation layer in Section 5.2. Despite different adsorption dynamics shown in Section 5.3.1, longer-length polycation PAH_{200} conformations cover approximately half of the 4 nm AuNP surface, leaving the citrate layer exposed (Section 5.3.2). The hydrophilic charged groups of PAH_{200} segregate radially relative to the AuNP center into multiple layers due to the competition between electrostatic attraction to the AuNP surface and repulsion between monomers (Section 5.3.3). We reproduce the formation of solvent-exposed loops and tails and surface-bound trains observed in top-down models [137, 138, 139]. At the atomistic scale, we find that short 1–2-monomer trains and loops are the dominant structural features of the adsorbed PAH_{200}, forming bilayer-like segments on the AuNP surface (Section 5.3.4). We conclude with a possible coarse-graining scheme described in Section 5.3.5, incorporating the hemispheric coverage of the polycation with exposed citrate layer, surface-bound bilayer-like segments, and dynamic amphiphilic loops and tails unique to PAH-AuNPs. For coarse-grained simulations of the nano-bio interface, we find that it would be essential and appropriate to implement this minimum level of detail for interactions of these polyelectrolyte-coated nanoparticles with amphiphilic biomolecules, such as lipids and proteins.

5.2 Materials and Methods

5.2.1 Citrate-Coated AuNP, PAH_{200}, and Solvent Models

AuNPs were created by placing gold atoms four atomic radii apart, arranged in a face-centered cubic lattice contained within a sphere, and equilibrating at 300 K in vacuum, using Lennard-Jones parameters developed by Heinz and co-workers [112] to create a nearly spherical, 4 nm diameter multifaceted core. In simulations for the adsorption of citrate and PAH_{200} onto gold, a shallower potential well depth is used for the Lennard-Jones parameter, ε, for gold [110, 119], and positions of gold atoms are kept fixed throughout the simulations. The OPLS-UA force field [144] was used for the carbon backbones of citrate and PAH_{200} and the -AA force field [109] for charged terminal groups, sodium and chloride counterions, and TIP3P solvent. The list of force-field parameters is presented in Table A5.1 in the Appendix.

Citrate-coated AuNPs were constructed in implicit solvent. Implicit solvent for all simulations was modeled using a Langevin thermostat at 300 K, a damping constant of

10 ps^{-1}, relative permittivity of 80.1, and the particle-particle particle-mesh (PPPM) method to compute electrostatic interactions in the presence of explicit counterions. Following the surface citrate density predicted by experiment [42] and used in simulations [33], we randomly distributed 90 citrate^{3-} molecules in a simulation box with the AuNP at the center. A steering force was applied to guide the central-carboxylate groups of citrate molecules to the AuNP surface. We focus on the citrate^{3-} charge state, although the presence of H_2citrate^{-} on the AuNP surface has also been reported [42]. The effect of citrate charge state on polycation adsorption will be discussed in Chapter 6. Due to the known unphysical electrostatic interactions between the hydroxyl hydrogen and central-carboxylate oxygen in citrate that occur with existing force fields [145], the citrate backbone that contains the central-carboxylate and hydroxyl groups was kept rigid and fixed on the AuNP surface for subsequent simulations. At charged interfaces, it is possible that small charged molecules reorient or detach from the interface, as observed at the lipid-water interface upon adsorption of polycations [146]. In studies of protein adsorption onto citrate-coated AuNPs, the use of AuNP models with citrate fixed on the surface in simulations has been seen to lead to final protein orientation on the AuNP surface in agreement with experiment [32, 33].

PAH_{200} was initially fully extended and energy minimized. The atoms were given random initial velocities and heated to 300 K in implicit solvent, until the PAH_{200} reached a random-coil state that fit in a $200 \times 100 \times 100$ Å^3 water box. PAH_{200} was equilibrated for 50 ns in TIP3P water with chloride ions. All explicit-solvent simulations were run at constant NPT at 1.0 atm and 300 K with a 1.0 fs timestep, using the PPPM method for electrostatic calculations. Five different PAH_{200} conformations were generated using this setup, which reproduced loosely clustered regions along the extended polymeric backbone, as previously observed in simulations of polyelectrolytes in explicitly modeled poor solvent (*e.g.* water) [147]. Each conformation was paired with a different citrate-coated AuNP in simulations (Figure A5.1).

5.2.2 Methods: All-Atom Simulations

The adsorption of PAH_{200} onto citrate-coated AuNPs was simulated using both implicit- and explicit-solvent conditions. Periodic boundary conditions are used with at least 15 Å from the PAH_{200} and AuNP to the edges of the simulation box along x, y, and z dimensions. Box sizes were chosen such that the salt concentration fell within the range 0.1-0.2 M with varying number of PAH_{200} added and the changing box size during the NPT equilibration. Box volume was approximately 5,000,000 Å^3 and included ∼500,000 atoms in explicit-solvent simulations. Initial configurations for all simulations were generated using Packmol [115], and all simulations were performed using LAMMPS [116] at 1.0 fs per timestep with 10 Å cutoff for pairwise interactions. On the XSEDE HPC Resource Bridges, this required ∼480 CPU hours to integrate for 120 ns on 448 processors, and this limited the number of trajectories that was obtained. Additional simulation details on system size and simulation times are in Table A5.2.

For implicit-solvent simulations, PAH_{200} was initially equilibrated in explicit solvent along with its coordinating chloride ions and then placed near a nanoparticle with one of the polycation's ends 8 Å away from its surface (Figure 23). Sodium and chloride ions were allowed to equilibrate for 2.5 ns, while keeping the atoms in the gold core and PAH_{200} fixed. The constraints on PAH_{200} were removed, and the distances between each nitrogen atom per monomer of PAH_{200} and the nanoparticle's center of mass (NP-COM) were tracked at each timestep to check the progress of PAH_{200} adsorption.

Once all nitrogen atoms were within 4 nm of the NP-COM, simulations were run for an additional 5 ns with data collected every picosecond during the last nanosecond. Five simulations were run in total, one for each PAH_{200} conformation. An additional simulation was run for each condition, so as to observe the deposition of a second PAH_{200} a onto the opposite pole from which the first was added.

For explicit-solvent simulations, the PAH_{200} was placed near the AuNP with one of the polycation's ends at 4 Å away from its surface. The gold core and PAH_{200} were first fixed, and water and counterions were allowed to equilibrate for 0.5 ns. To track adsorption of PAH_{200} once released, each PAH_{200} was evenly divided into five segments, and the distances between the COM of the first, middle, and last 40-monomer segments, labeled 1, 3, and 5, respectively, and their NP-COMs were plotted over time (Figure 24). These distances relaxed to a small constant value after 110 ns of simulations, signifying adsorption. Simulations were then run for an additional 10 ns with data collected every 10 ps.

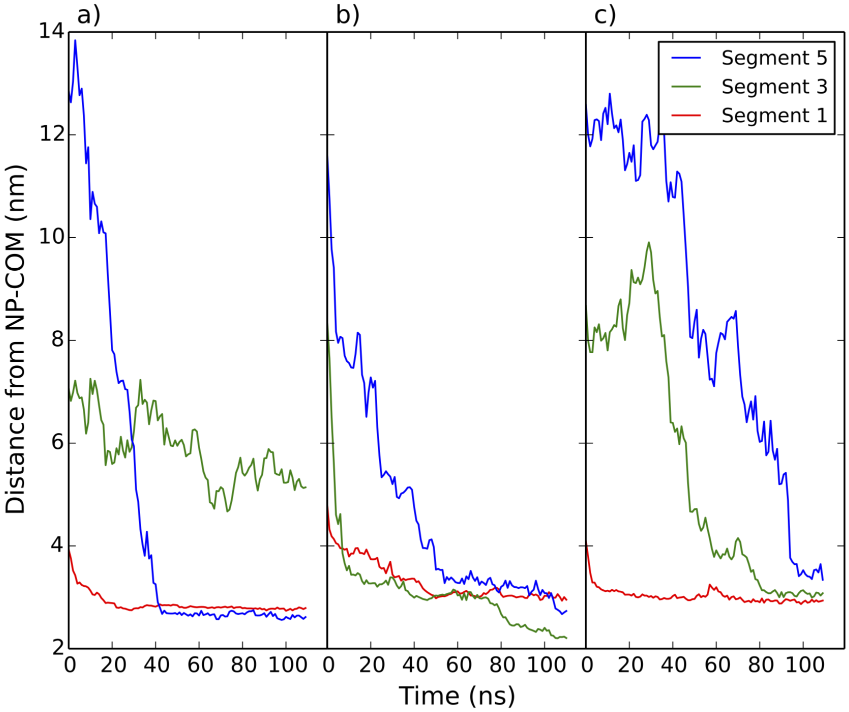

Figure 24: Adsorption of the center of mass of the first (segment 1), third (segment 3), and fifth (segment 5) 40-monomer segment of PAH_{200} over time in explicit solvent relative to the nanoparticle center of mass (NP-COM) for different PAH_{200} (a-c).

Due to the system size, three simulations were run in explicit solvent. We compare the adsorption of the three starting configurations for PAH_{200} used in both implicit- and explicit-solvent simulations. Results for the remaining two PAH_{200} conformations used in implicit-solvent simulations are presented in the Appendix (Figs A5.5 and A5.6). From this finite number of trajectories, we find common structural features that emerge upon adsorption of long-length polyelectrolytes onto the AuNP surface independent of solvent condition.

5.2.3 Methods: Coarse-Graining Schemes

From the final frame of each simulation run in explicit solvent, we group the three-carbon chain into one hydrophobic bead and the ammonium group into one charged bead for each monomer with bead positions set by their centers of mass. We provide a preliminary coarse-graining scheme to emphasize atomistic properties that will be implemented in future coarse-grained simulations of PAH-AuNPs at the interface of biomembranes. The coarse-grained structures are, therefore, a product of the all-atom simulations of this work and are available for use in coarse-grained simulations in future work.

5.3 Results and Discussion

5.3.1 Adsorption Dynamics of PAH_{200}

The effects of implicit and explicit solvents on dynamical processes, such as the mechanical pulling of polypeptides [148], the formation of polyelectrolyte complexes [149], and the adsorption of polyelectrolytes onto surfaces [150, 151], have been well addressed. For the dynamical behavior of the system, we, therefore, focus our attention on the differences in adsorption dynamics in explicit solvent between different starting PAH_{200} conformations. For each simulation, PAH_{200} was initially aligned such that the end-to-end vector was normal to the nanoparticle surface. Figure 24a shows that the first and last 40-monomer segments of PAH_{200} (segments 1 and 5, respectively) adsorb to the surface within 20 ns of each other, leaving the middle 40-monomer segment 3 as a loop in solution. For a different PAH_{200} conformation, segment 3 adsorbs onto the nanoparticle surface first, followed by segment 1, and then segment 5 (Figure 24b).

Figure 24c shows sequential wrapping of the nanoparticle from segments 1 to 5 by PAH_{200}. Even though the same orientation is used for the initial deposition of PAH_{200} on the nanoparticle surface, different adsorption dynamics are sampled as a result of the different starting conformations of PAH_{200}.

5.3.2 Surface Coverage of PAH_{200}

Despite the different adsorption mechanisms per PAH_{200} configuration, PAH_{200} adsorption leads to a half-coated AuNP in all cases (Figure 25). To depict the surface coverage of PAH_{200} on AuNPs, each PAH-AuNP is, first, rotated so that the vector connecting the nanoparticle's center of mass (NP-COM) to the center of mass of PAH_{200} maps onto the positive z axis. We create a two-dimensional histogram with a bin size of $\pi/20$ rad and track the projection of nitrogen atoms in PAH_{200} onto the AuNP surface as a function of spherical azimuthal- and polar-angle coordinates. The density profile of the nitrogen atoms in PAH_{200} shows that PAH_{200} is more evenly distributed on a hemisphere of the nanoparticle in implicit solvent, whereas more voids are present in the density profiles in explicit solvent, signifying incomplete hemispheric coverage of PAH_{200} (Figure 25). The voids in the surface coverage of PAH_{200} in explicit solvent suggest that there is a greater distribution of monomers along the radial direction relative to the NP-COM arranged in loops exposed to solution.

Incomplete hemispheric coverage of PAH_{200} suggests that a second PAH_{200} could potentially adsorb onto the bottom hemisphere. Due to the system size and computational cost, we limit simulations of a second PAH_{200} adsorption to implicit solvent. These simulations suggest that, in implicit solvent, adsorption of a second PAH_{200} is possible with similar structure to the first adsorbed PAH_{200}. Without the

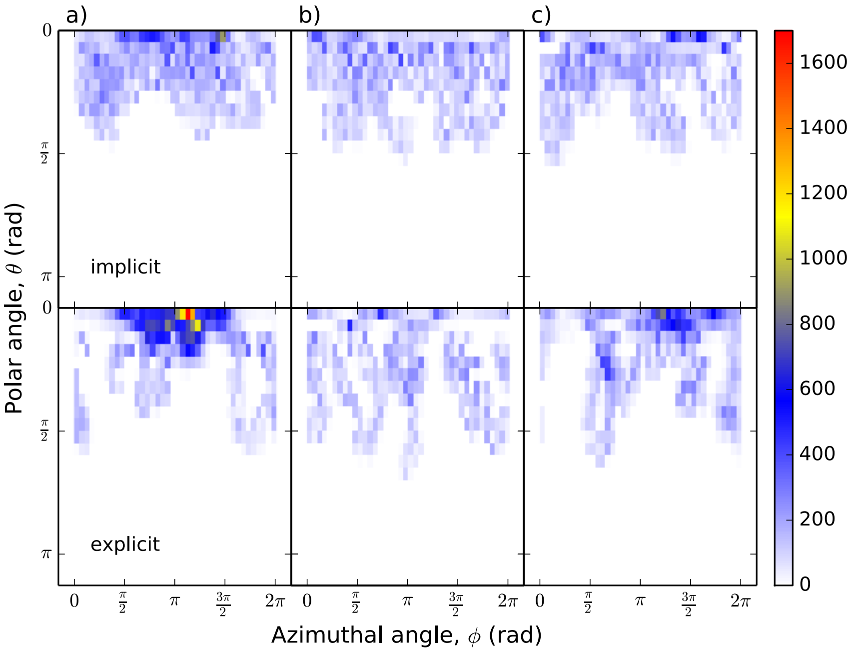

Figure 25: Surface coverage of nitrogen atoms of different PAH_{200} (a-c) in implicit and explicit solvents. The azimuthal angle ranges from 0 to 2π rad along the equator of the nanoparticle. The polar angle ranges from 0 rad at the north pole to π rad at the south pole. The bin size of the two- dimensional histogram is $\pi/20$ rad. The color scale shows the density of the nitrogen atoms.

uniform dielectric screening used for our implicit-solvent model, it is possible that the second PAH_{200} incompletely adsorbs enabling the bridging between two AuNPs and promoting the aggregation of 4 nm PAH-AuNPs observed in experiment [11, 39].

5.3.3 Radial Distribution of PAH_{200}

The radial distribution function, *g(r)*, between nitrogen atoms of PAH_{200} and the NP-COM is calculated through a histogram, with bin size of 0.1 Å, averaged over 1000 frames per trajectory for five trajectories in implicit solvent and three in explicit solvent and normalized by the annular volume (Figure 26). The *g(r)*'s for individual trajectories are provided in Appendix (Figs. A5.3 and A5.4). Two major peaks or sets of peaks, one close to the nanoparticle surface (2 nm away from the NP-COM) and another in solution, are present in the *g(r)* from implicit- and explicit-solvent simulations, respectively (Figure 26). After the addition of a second PAH_{200}, the major peaks in the *g(r)* sharpen, but peak positions remain the same. The *g(r)* from explicit-solvent simulations reaches zero by 6 nm from the NP-COM, confirming that PAH_{200} has a broader radial distribution in explicit solvent extending far into solution. The distance between major peaks in the *g(r)* from implicit-solvent simulations is 0.6 nm, which is slightly less than the length of the five-carbon backbone between $NH_3{}^+$ groups in adjacent monomers, assuming a carbon-carbon single-bond distance to be 1.54 Å. In addition, the peak heights have the same magnitude, signifying that there is a 1:1 distribution of monomers between the surface-bound and solvent-exposed layers. These results suggest that the most significant structural features in the addition of PAH_{200} to the NP is the presence of short 1–2-monomer loops and trains, that resemble kinks, extending radially from the NP surface.

5.3.4 Structural Motifs in PAH_{200}

To determine the specific structural motifs in PAH_{200} adsorbed onto the NP surface, we perform a histogram count of the number of monomers in solvent-exposed loops, free tails, and surface-bound trains divided by total number of sampled frames. A normalized value greater than 1.0 signifies at least one instance in every frame (Figure 27). A monomer is considered to be bound to the surface and part of a train if the nitrogen atom is within 3.48 Å from an oxygen atom on citrate; the cutoff distance was chosen to be $2^{1/6}\sigma$ after applying the geometric mixing rule on the nonbonded distance parameter, σ, from the OPLS-AA force field [109]. The solvent-exposed segments within PAH_{200} are considered as loops and free segments at the ends of PAH_{200} as tails. Representative

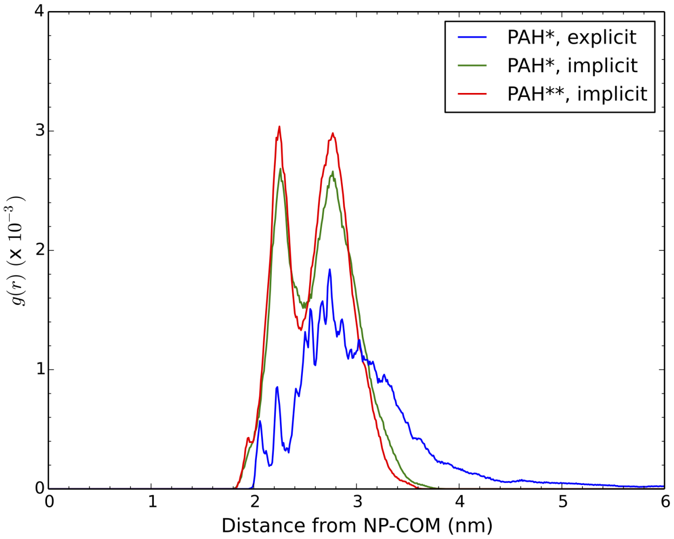

Figure 26: Radial distribution function, *g(r)*, between the nitrogen atoms of PAH_{200} deposited on the upper hemisphere of a nanoparticle and the nanoparticle center of mass (NP-COM). The asterisk (*) denotes the number of PAH_{200} added to the nanoparticle. For **, a second PAH_{200} was deposited on the bottom hemisphere of the AuNP.

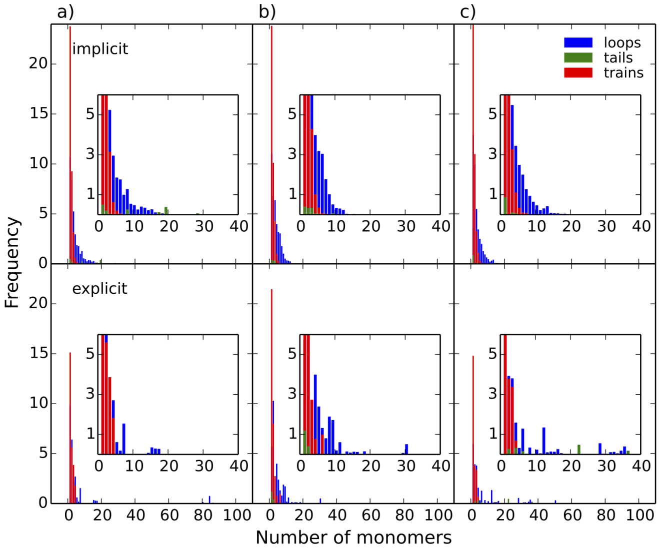

Figure 27: Histogram of the frequency of solvent-exposed loops, free tails, and surface-bound trains with n number of monomers within different PAH_{200} (a-c) in implicit and explicit solvents. The distributions are divided by the total number of frames sampled such that 1.0 indicates one instance in every frame.

snapshots of loop, tail, and train structures are shown in Figure A5.2. As suggested from the radial distribution functions, 1–2-monomer as well as 3-monomer, trains and loops appear most frequently on the nanoparticle surface (Figure 26). Adsorption of PAH_{200} in implicit solvent leads to a similar distribution of short trains and loops with up to 10 monomers per loop, whereas adsorption in explicit solvent leads to a more varied distribution in loop and tail lengths.

5.3.5 Bottom-Up Coarse-Graining Scheme for PAH_{200}-AuNPs

Despite the heterogeneity in the structure of PAH_{200} on AuNPs, it is important to identify which atomistic properties need to be represented in coarse-grained models of polyelectrolyte-coated AuNPs. From the atomistic PAH_{200}-AuNP structures obtained from explicit-solvent simulations, we construct initial coarse-grained structures for PAH_{200} by grouping the atoms in the carbon backbone of each monomer and NH_3^+ group into beads positioned at their respective centers of mass. These coarse-grained PAH_{200} structures are shown with the atomistic AuNP core in Figure 28. Figure 28 highlights the radial extension of charged NH_3^+ groups *via* small solvent-exposed loops formed between surface-bound trains. The separation of charged groups connected by the carbon backbone within adjacent monomers reveals a bilayer-like motif on the nanoparticle surface. Several groups [130, 131, 132, 133, 134] have used simulations of charged alkanethiol-coated AuNPs with lipid bilayers to demonstrate that exposed hydrophobic groups in the alkanethiols are required at the nanoparticle-ligand interface for nanoparticles to associate with and disrupt lipid bilayers. This molecular scale structure on larger-scale behavior is important because it is absent in existing top-down polyelectrolyte models [138, 139]. A coarse-graining scheme for PAH_{200} coating on

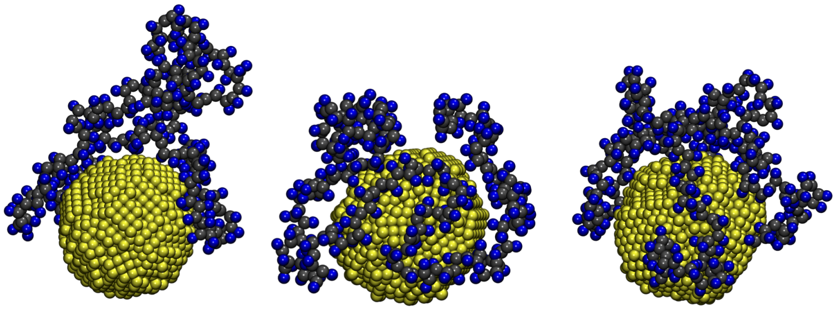

Figure 28: PAH_{200} models coarse-grained per monomer by the center of mass of the carbon atoms (gray) and of the NH_3^+ group (blue) on an atomistic 4 nm gold core.

the AuNP would have to incorporate elements that can give rise to the bilayer-like segments of PAH_{200} observed on the AuNP surface and dynamic segments in the form of longer loops and tails with amphiphilicity shown in Figure 28. How the surface-bound segments and heterogeneous spatial charge and hydrophobic backbone distribution in PAH_{200} adsorbed onto AuNPs induce greater membrane disruption [135] and stress responses in organisms [12, 136] compared to charged alkanethiol-coated AuNPs still needs to be addressed.

5.4 Conclusion

Using atomistic molecular dynamics simulations, we characterize the adsorption and structure of polycations on a citrate-coated gold nanoparticle, and thereby provide a benchmark for structures of polyelectrolyte-coated gold nanoparticles to be used for coarse-grained simulation techniques, such as the MARTINI force field [152] and dissipative particle dynamics [153, 154]. The average length of a PAH polycation was determined by experiment to be 200 monomers [39]. Through simulations, we find that adsorption of a single PAH_{200} leads to incomplete hemispheric coverage of the polyelectrolyte on a 4 nm AuNP. Incomplete hemispheric coverage of positively charged PAH and the exposed negatively charged citrate layer on AuNPs could promote the aggregation of 4 nm PAH-AuNPs observed in experiments [11, 39] *via* bridging nanoparticles by oppositely charged patches or by free PAH in solution [155]. The surface coverage of polyelectrolytes with an average length of 200 monomers as a function of nanoparticle size, therefore, needs to be further considered in the design of nanoparticles as a means of controlling nanoparticle aggregation in suspension.

A detailed structural analysis from our simulations confirms the presence of surface-bound and dynamic polyelectrolyte segments on the nanoparticle surface, as previously reported in top-down coarse-grained simulations of polyelectrolyte adsorption [137, 138, 139] and NMR experiments [102]. It further shows the atomistic distribution of the hydrophobic carbon backbone and NH_3^+ charged groups into bilayer-like segments bound to the surface and amphiphilic, dynamic segments, from which we construct a new coarse-grained representation for polyelectrolyte-coated AuNPs. Nanoparticle transformations in suspension with free PAH and in biological environments are thus strongly affected by incomplete nanoparticle coverage by a positively charged polycation, exposed negatively charged citrate patches, the distribution of polyelectrolyte segments with different dynamics on the surface, and the amphiphilicity of these segments.

Chapter 6

Density, Structure, and Stability of Citrate^{3-} and H$_2$citrate^{-} on Bare and Coated Gold Nanoparticles

6.1 Introduction

Citrate anions act as both reducing and capping agents in the synthesis of gold nanoparticles (AuNPs) through the Turkevich method [156, 157]. They consequently make up the first natural layer coating on engineered AuNPs. Once synthesized, AuNPs can be functionalized for use in biomedical applications, such as molecular sensing, drug delivery, and photothermal therapy [2, 158]. In this latter process, the citrate layer must be readily displaced for the thiol functionalization [93, 159, 160] of AuNPs *via* citrate-thiol ligand exchange, and must also be stably adsorbed on the AuNP surface as the initial charged layer for layer-by-layer polyelectrolyte assembly [12, 15, 161]. An accurate characterization of citrate anions on the AuNP surface is, therefore, essential to characterize the structural and dynamic properties of the functionalized layer in the presence of citrate, and thereby the transformations of these functionalized AuNPs in biological environments that might promote or impede their intended function [6, 7].

The charge state, ligand density, structure, and stability of citrate on the AuNP surface are key measurables that influence AuNP functionalization though the correlations between them have not yet been fully resolved in the literature. Characterization of citrate-coated AuNPs (cit-AuNPs) has, thus far, focused on experimental techniques that require dried samples [40, 42, 43, 162] and *in vacuo* density functional theory (DFT) calculations [43]. Further, computational characterization has largely focused on minimum-energy binding of a single citrate^{3-} or H_2citrate$^-$ anion to a metal nanoparticle surface [43, 163, 164, 165] and reactive simulations limited to small time and length scales [166]. Using attenuated total reflectance-Fourier transform infrared spectroscopy (ATR-FTIR), characteristic peaks of hydrogen-bonded carboxylic acid groups were detected after sealing and isolating the citrate layer with long-chain alkanethiol functionalization, suggesting that citrate exists in the H_2citrate$^-$ state on the AuNP surface [42]. These ATR-FTIR studies further suggest the dominant citrate species as that involving the coordination of citrate to the AuNP surface *via* the central carboxylate group with terminal carboxylate groups also near the surface to promote intermolecular hydrogen bonding. Several possible relative orientations of the carboxylate groups to the AuNP surface are shown in Figure 29B, and the chemical structure of H_2citrate$^-$ is included in Figure A6.1 in the Appendix. The central carboxylate group is directly connected to the –C–OH group, whereas the terminal carboxylate groups are each separated from the –C–OH group by a –CH2 group. The previous ATR-FTIR studies cited above also indicate the presence of a second dangling layer of H_2citrate$^-$, forming bilayered H_2citrate$^-$ complexes on the AuNP surface with an ideal organization of two surface-bound H_2citrate$^-$

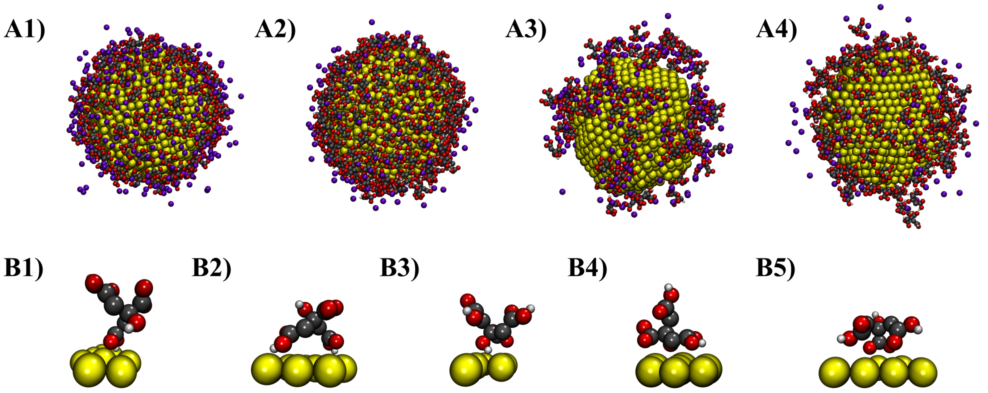

Figure 29: Representative 4 nm cit-AuNPs in row A (top) and citrate configurations in row B (bottom): (A1) citrate^{3-} monolayer maximally packed on AuNPs in implicit solvent, (A2) H_2citrate^{-} monolayer maximally packed on AuNPs in implicit solvent, (A3) citrate^{3-} on AuNPs in explicit solvent, and (A4) H_2citrate^{-} on AuNPs in explicit solvent; (B1) tall, (B2) bridge, (B3) 0-arm, (B4) 1-arm, and (B5) 2-arm citrate configurations on AuNPs described in this study. The "tall" configuration has a single terminal carboxylate group bound to the AuNP surface. The "bridge" configuration has both terminal carboxylate groups bound to the surface with the central carboxylate and hydroxyl groups free. The 0-, 1-, or 2-arm configurations have either the central carboxylate or hydroxyl group bound to the surface with 0, 1, or 2 terminal carboxylate groups also bound, respectively. Cit-AuNPs consist of gold (yellow), carbon (gray), oxygen (red), and hydrogen (white) atoms. Na^{+} ions are shown in purple; water and counterions outside the solvent shell are removed for clarity in row A. Configurations are shown in the H_2citrate^{-} state in row B.

hydrogen-bonded to one dangling H_2citrate^{-}. To understand the binding modes of citrate, peaks from ^{13}C solid-state nuclear magnetic resonance (SSNMR) spectra of cit-AuNPs synthesized under varying initial citrate/Au molar ratios were assigned to molecular configurations of citrate^{3-} extrapolated from DFT calculations of fully deprotonated acetate, succinate, and glutarate anions on gold surfaces [43]. These studies show that the binding of both terminal carboxylate groups to the AuNP surface with central carboxylate and hydroxyl groups free is preferred at low packing density, and that the binding of a single terminal carboxylate group to the AuNP surface is preferred at high packing density.

In addition to the wide variation in the reported charge states of citrate on the AuNP surface in the literature, the surface citrate density has also been seen to range widely from 2.8×10^{-10} to 7.8×10^{-10} mol/cm^2 [12, 42, 162]. We use these units to be consistent with the reported literature and note that they translate to the range of 1.7 to 4.7 molecules/nm^2 in terms of natural units at the nanoparticle scale. The range for surface charge density widens, starting from 2.8×10^{-10} up to 2.34×10^{-9} mol/cm^2, if the charge state of citrate can include either H_2citrate$^-$ or citrate^{3-} on the AuNP surface. Several factors contribute to this broad range for ligand density. To approximate the surface citrate density, a geometric calculation [42] was performed by Park and Shumaker-Parry assuming that each adsorbed citrate has a rectangular covering of the surface with an area approximately equal to 28 Å^2. Their calculation underestimates the ligand density because it assumes that citrate anions adsorb along the length of the molecule with the central carboxylate group bound and terminal carboxylic acid groups near the surface and does not consider other binding modes [43] of citrate. Elemental analysis of carbon [162] in cit-AuNPs has previously been used to determine citrate density, but this method also samples oxidized byproducts of citrate on AuNPs, overestimating the ligand density. Another factor that can lead to overestimates in the experimentally determined ligand density arises from the drying process for preparing samples in both elemental analysis and ligand-density analysis by X-ray photoelectron spectroscopy [12, 40] as it leads to aggregation of ligands. Although AuNP shape, size, and effective surface charge are routinely reported in the characterization of engineered AuNPs [167], reports on experimentally determined ligand densities are less common; for citrate, such values not only range widely but are also limited. This is largely in part because citrate anions are present at high concentrations in solution, making it difficult to characterize and isolate the citrate anions on the AuNP surface *in situ* from those in the bulk solution, and are assumed to be readily displaced [160] upon functionalization of AuNPs. Most prior experiments have centered on the effective negative surface charge of cit-AuNPs and their effect on the acquisition of electropositive protein coronas [29, 47, 48, 49] and cytotoxicity [12, 15]. Generally, cationic AuNPs are considered more toxic than anionic AuNPs [8, 9, 10]. Beyond general toxicity, attention is increasingly being brought to molecular-level mechanistic understanding of how exposure to different ligand types with the same effective charge, such as citrate and anionic thiols and polyanions with varying hydrophobicity, elicits different gene-expression levels and other biological responses [6, 12, 15, 94, 168, 169, 170], emphasizing the need, addressed here, for an accurate characterization of the structure and density of the citrate layer on AuNPs.

Several computational approaches have been used to model functionalization and biomolecular corona formation on cit-AuNPs and the nano-bio interface more generally [22, 171]. In the all-atom molecular dynamics simulations of polycation functionalization onto cit-AuNPs discussed in Chapter 5, citrate^{3-} molecules were explicitly modeled and fixed at a density of 2.8×10^{-10} mol/cm^2 on the AuNP surface [24]. In similar coarse-grained simulations, surface gold atoms were negatively charged to represent the citrate layer and to construct the polycation-coated AuNP and investigate lipid self-assembly on such AuNPs [26]. Three possible models [32, 33] for fibrillogenic-protein binding to cit-AuNPs have been reported recently. In one study [32], the AuNP surface was homogeneously coated with citrate molecules at a density of 4.4×10^{-10} mol/cm^2, and only 10% of the molecules were charged as citrate^{3-} with 90% left neutral to account for local pH effects. In the other study [33], both an all-atom and a coarse-grained point-charge model were used. For the all-atom model, surface gold atoms were positively charged to promote adsorption of citrate^{3-} at a surface density of 2.8×10^{-10} mol/cm^2 with a surface charge density of 8.4×10^{-10} mol/cm^2. For the coarse-grained model, point charges were homogeneously distributed on a spherical NP, following the same surface charge density used in the all-atom model. Fixed point charge-coated nanoparticle models with varying surface charge density have also been used for top-down coarse-grained simulations of nanoparticle-membrane interfaces [172, 173, 174], but experimental validation and bottom-up coarse-graining approaches are needed to predict reliably the biological outcomes of nanoparticle exposure [22, 175]. In all cases, citrate molecules are explicitly modeled as an all-atom citrate^{3-} or implicitly (in coarse-grained models) through a surface charge density on the order of what would be a high density of citrate^{3-} on the AuNP surface. These simulations assume that the density of citrate on the AuNP surface is constant and uniformly distributed in a monolayer and that citrate^{3-} molecules stay fixed on the surface at charged nano-bio interfaces. Recent simulation studies by other groups have investigated citrate adsorption onto gold surfaces to reveal face-dependent binding of citrate and its effects, such as in DNA adsorption onto cit-AuNPs [176], and have determined the structure of citrate adlayers at a range of surface citrate densities ranging from 1.49 to 2.98×10^{-10} mol/cm^2 of an Au(111) slab [177], but to our knowledge only the citrate^{3-} state was considered.

We perform all-atom molecular dynamics simulations to investigate the density, structure, and stability of both citrate^{3-} and H_2citrate^{-} on AuNPs. We use implicit-solvent simulations to examine the maximum packing density and changes in the coordination modes of citrate^{3-} and H_2citrate^{-} on the surface of 4, 6, and 8 nm AuNPs with increasing packing density. We find from implicit-solvent simulations that the maximum packing density and coordination modes of both citrate species on the AuNP surface are independent of nanoparticle size. Explicit-solvent simulations are used to determine if the structures of citrate^{3-} and H_2citrate^{-} layers on 4 nm AuNPs are consistent with those from implicit solvent. The coordination modes and spatial distribution for H_2citrate^{-} are independent of solvent condition but differ significantly for citrate^{3-} between implicit and explicit solvents. The coordination modes of citrate determined previously from ATR-FTIR [42] and ^{13}C SSNMR [43] experiments agree with those found for the H_2citrate^{-} state in our explicit-solvent simulations. Representative images of the coordination modes of citrate examined in this study and structures of 4 nm cit-AuNPs in implicit and explicit solvents are shown in Figure 29. Representative structures of 6 and 8 nm cit-AuNPs in implicit solvent are shown in Figure A6.3. These structures also qualitatively show face-dependent binding of citrate on metal nanoparticles, which has been shown for citrate and other ligands by experiment [42] and simulation [140, 141, 164, 178, 179].

We test the stability of citrate^{3-} and H_2citrate^{-} layers by depositing a 200-mer polycation poly(allylamine hydrochloride), PAH_{200}, on cit-AuNPs. We find that PAH_{200} highly disrupts the citrate^{3-} layer on the AuNP surface. In contrast, PAH_{200} displaces the dangling H_2citrate^{-} layer, but there is no change in the density of the surface-bound H_2citrate^{-} layer. Representative structures of PAH-wrapped cit-AuNPs (PAH-cit-AuNPs) are shown in Figs. A6.4 and A6.5. We use *in situ* ATR-FTIR on PAH-cit-AuNPs to show that citrate exists as H_2citrate^{-} at highly charged interfaces. The intermolecular hydrogen bonding between H_2citrate^{-} stabilizes the negatively charged layer in the presence of adsorbing positively charged molecules, such as PAH_{200}. The density of H_2citrate^{-} on AuNPs including the dangling H_2citrate^{-} layer totals 3.3

$\times$ 10^{-10} and is 2.8 $\times$ 10^{-10} mol/cm^2 for the surface-bound layer. The total density of H_2citrate$^-$ across the two layers decreases slightly to 3.0 $\times$ 10^{-10} mol/cm^2 upon adsorption of PAH_{200} due to some displacements of the dangling second H_2citrate$^-$ layer, and the density of the surface-bound H_2citrate$^-$ layer remains consistent. The surface charge density contributed by H_2citrate$^-$ directly on the AuNP surface is 2.8 $\times$ 10^{-10} mol/cm^2 nonuniformly distributed due to face-dependent binding.

Through a combination of molecular dynamics simulations and *in situ* ATR-FTIR spectroscopy, we determine an ensemble of binding modes that collectively stabilize the citrate layer capping the metal nanoparticles on bare and polycation-coated AuNPs and ultimately determine its structure and density. We provide a consensus citrate density for the citrate^{3-} and H_2citrate$^-$ states to aid in the experimental characterization of as-synthesized and functionalized cit-AuNPs, a surface density of H_2citrate$^-$ that is appropriate for the implementation of all-atom and coarse-grained models, and a surface charge density for fixed-charge coarse-grained models of cit-AuNPs.

6.2 Materials and Methods

6.2.1 Molecular Dynamics Simulations

To simulate the packing of citrate, we applied a steering force of 0.1 kcal/(mol Å) on citrate anions toward the nanoparticle center until they were within 7.5 Å from either the bare nanoparticle surface or a monolayered citrate surface depending on the initial condition of the simulation. Beyond this cutoff distance, the steering force is no longer applied, and the citrate anions remain within the 10 Å cutoff for pairwise interactions such that citrate anions can weakly interact with and potentially adsorb onto the gold surface. Steering forces in the range of 0.1-5.0 kcal/(mol Å) were initially tested (data not shown), and a weak steering force of 0.1 kcal/(mol Å) was chosen to ensure that citrate anions were dispersed in solvent without artificial jamming in the vicinity of the cutoff distance of the steering force. The steering force was not employed during equilibration, enabling desorption of excess citrate from the nanoparticle surface. All simulations were carried out using LAMMPS [116], using periodic boundary conditions and a 1.0 fs timestep. Specific details on the simulation setup and force-field parameters are provided in Tables A6.1, A6.2, A6.3 in the Appendix.

For implicit-solvent simulations, five simulations for the adsorption of citrate^{3-} and five for H$_2$citrate$^-$ adsorption onto AuNPs were run for each AuNP size. The implicit solvent was modeled using Langevin dynamics at 300 K with a damping constant of 10 ps^{-1} and a dielectric constant of 80.1, with the particle-particle particle-mesh (PPPM) method used for long-ranged electrostatic calculations.

For explicit-solvent simulations, we ran five simulations each of the adsorption of citrate^{3-} and H$_2$citrate$^-$ onto 4 nm AuNPs in TIP3P solvent and five simulations each of PAH$_{200}$ deposition onto the equilibrated 4 nm AuNPs coated with citrate^{3-} and H$_2$citrate$^-$ under constant NPT conditions, that is, for number of atoms N, pressure P at 1.0 atm, and temperature T at 300 K, using the PPPM method for long-ranged electrostatic calculations.

6.2.2 ATR-FTIR Spectroscopy

ATR-FTIR spectra of PAH-cit-AuNPs were acquired using a PIKE GladiATR attachment equipped with a triple-bounce diamond IRE on a Bruker Vertex 70 FTIR instrument. Each spectrum was acquired at a resolution of 4 cm^{-1} and signal-averaged over 500 scans. All absorbance spectra were taken in solution and are referenced to ultrapure water.

6.3 Results and Discussion

6.3.1 Maximum Packing Density of Citrate^{3-} Monolayers, H$_2$citrate$^-$ Monolayers, and H$_2$citrate$^-$ Bilayers on 4, 6, and 8 nm AuNPs.

To simulate the packing of citrate anions onto AuNPs using molecular dynamics simulations, we first randomly distributed three citrate^{3-} or H$_2$citrate$^-$ molecules per nm^2 (5×10^{-10} mol/cm^2) in a simulation box with a 4, 6, or 8 nm AuNP fixed at the center. A steering force toward the center of the AuNP was applied to citrate anions until the anions were 7.5 Å from the AuNP surface. This process was run for at least 10 ns until the AuNP surface was saturated with citrate (Figure 30). Simulations were run for an additional 10 ns without a steering force and with data collected during the last 5 ns to analyze the citrate anions that remain packed on the AuNP surface.

In implicit solvent, we find that citrate^{3-} maximally packs into a monolayer, and that the development of high surface charge density prevents bilayer formation. We used this distinction to calculate a minimum Au–O distance between surface gold atoms and oxygen atoms of citrate needed to consider a citrate anion as bound to the AuNP surface in our simulations. We find that the number of citrate^{3-} attached to the AuNP surface as a function of Au–O distance saturates beyond an Au–O distance of 3.5 Å, showing that this Au–O distance accounts for all citrate^{3-} in the adsorbed monolayer (Figure A6.2). We, therefore, define the condition for which citrate^{3-} or H$_2$citrate$^-$ being bound to the surface according to when the anion has an Au–O distance that is less than 3.5 Å.

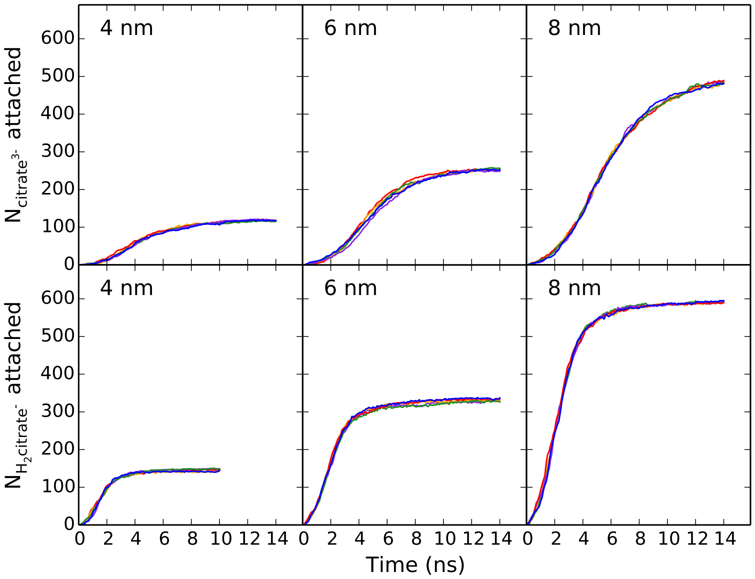

Figure 30: Number of citrate adsorbed onto 4, 6, and 8 nm AuNPs *vs.* time in implicit solvent, according to an Au–O cutoff distance of 3.5 Å and with an initial density of 3 citrate nm^{-2} randomly distributed in the simulation box. Trajectories are distinguished by color with no association between like colors in different panels.

The initial packing density of 3 molecules per nm^2 corresponds to 150 citrates on a 4 nm AuNP, 340 citrates on a 6 nm AuNP, and 600 citrates on an 8 nm AuNP. The number of citrate^{3-} attached after equilibration is lower than the initial packing density, whereas nearly all H$_2$citrate$^-$ adsorb onto the AuNP surface (Figure 30). The greater rate of H$_2$citrate$^-$ absorption and number of H$_2$citrate$^-$ adsorbed on AuNPs compared to citrate^{3-} highlight the increased stability imparted to the anionic citrate layer by the intermolecular hydrogen bonding between H$_2$citrate$^-$ anions. We placed each of the equilibrated structure of AuNPs coated with H$_2$citrate$^-$ in a simulation box, to which we randomly distributed an additional three H$_2$citrate$^-$ molecules per nm^2 of gold surface. A steering force toward the center of the AuNP was applied to the newly added citrate anions until they were 15 Å from the AuNP surface. This process was run for 10 ns to promote H$_2$citrate$^-$ bilayer formation on the AuNPs. For calculations at the packing density of the dangling second layer in bilayered H_2citrate$^-$, any unbound molecule that has a maximum intermolecular O–H hydrogen-bonding distance within 4.0 Å with surface-bound H_2citrate$^-$ is considered to be in the second layer. The conservative choice of this cutoff distance is consistent with the maximum of the observed range of O–H bond distances [180]. Simulations were run without the steering force for 25 ns, and desorption of excess H_2citrate$^-$ was observed (Figure 31). The maximum packing density of each layer in bilayered H_2citrate$^-$ was determined from additional 5 ns production runs. Table 1 shows the increase in packing density from citrate^{3-}, to monolayered H_2citrate$^-$, and to bilayered H_2citrate$^-$ at 3.74, 5.67, and 8.42×10^{-10} mol/cm^2, respectively, for 4 nm AuNPs. The maximum packing density is largely consistent between 4, 6, and 8 nm AuNPs (Table 1). A slightly higher packing density for all citrate species on 4 nm AuNPs could be attributed to greater curvature of this AuNP surface relative to larger-sized AuNPs. By dividing the maximum packing density of H_2citrate$^-$ in the surface-bound monolayer (H_2citrate$^-_{Layer1}$) by that of H_2citrate$^-$ in the dangling, second layer (H_2citrate$^-_{Layer1+2}$ – H_2citrate$^-_{Layer1}$) in Table 1, we determine a ratio of 2.06 for the number of H_2citrate$^-$ in the surface-bound layer to the number in the dangling second H_2citrate$^-$ layer on 4 nm AuNPs, 2.05 on 6 nm AuNPs, and 2.38 on 8 nm AuNPs. These values are close to the ideal distribution predicted by Park and Shumaker-Parry [42], supporting the use of our simulation parameters and implicit-solvent model for the ideal, maximally packed H_2citrate$^-$-coated AuNPs. Our results suggest that the highest reported citrate density, as determined from experiment [12] and referenced in Table 1, can only be reached through some combination of bilayered H_2citrate$^-$ on the AuNP surface and aggregation of citrate anions upon drying of samples for characterization.

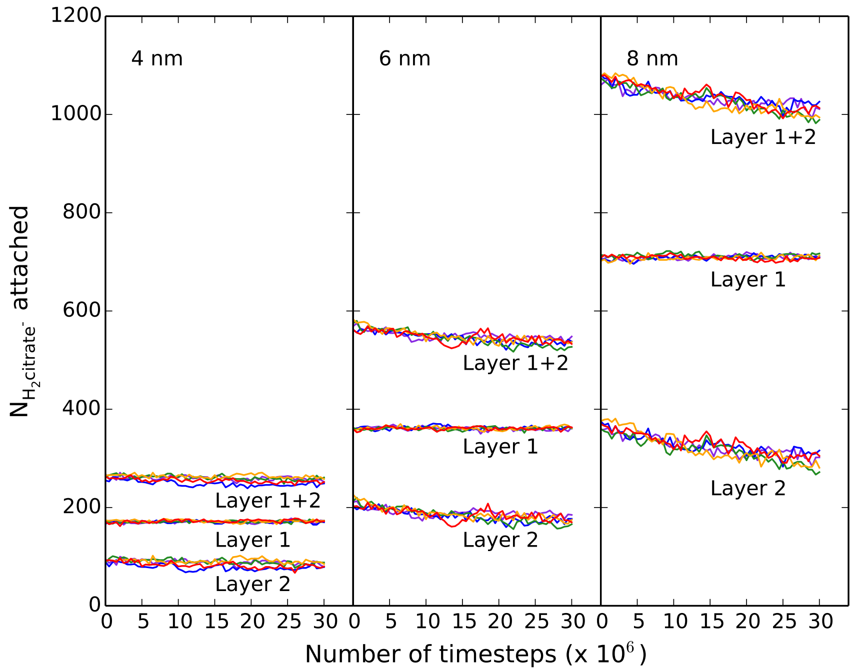

Figure 31: Number of H_2citrate$^-$ adsorbed onto 4, 6, and 8 nm AuNPs *vs.* time in implicit solvent with an additional density of 3 H_2citrate$^-$ nm^{-2} randomly distributed in the simulation box (totaling 6 H_2citrate$^-$ nm^{-2}) to saturate the surface-bound layer (Layer 1), promote the adsorption of a dangling second layer (Layer 2), and form bilayered H_2citrate$^-$ (Layer 1 + 2). Trajectories are distinguished by color with no association between like colors in different panels.

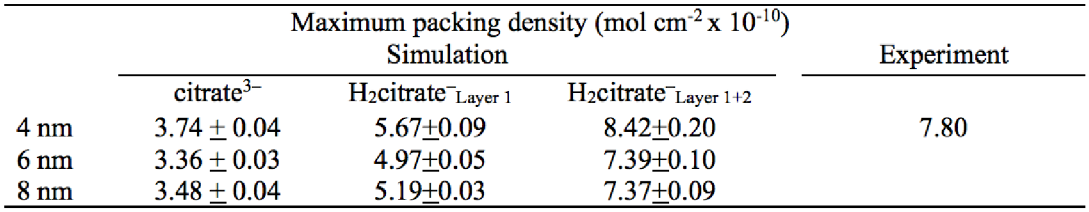

	Maximum packing density (mol cm^{-2} x 10^{-10})			
	Simulation			Experiment
	citrate^{3-}	H_2citrate$^-_{\text{Layer 1}}$	H_2citrate$^-_{\text{Layer 1+2}}$	
4 nm	3.74 ± 0.04	5.67±0.09	8.42±0.20	7.80
6 nm	3.36 ± 0.03	4.97±0.05	7.39±0.10	
8 nm	3.48 ± 0.04	5.19±0.03	7.37±0.09	

Table 1: Maximum Packing Densities of citrate^{3-}, H_2citrate$^-$ Monolayers, and H_2citrate$^-$ Bilayers Compared to Ligand Densities Calculated from Experiment

6.3.2 Molecular Configurations of Citrate as a Function of AuNP Size and Packing Density

We used the Au–O cutoff distance of 3.5 Å to determine if each citrate is bound to the AuNP surface *via* the terminal carboxylate, central carboxylate, or hydroxyl group. We defined molecular configurations according to the groups bound to the surface (Figure 29B). The tall configuration is defined as a citrate that has an oxygen from a single terminal carboxylate group within the cutoff distance from the AuNP surface. The bridge configuration is distinguished by both terminal carboxylate groups of citrate bound to the surface with the central carboxylate and hydroxyl groups free. The configurations are considered 0-, 1-, or 2-arm if either the central carboxylate or hydroxyl group is bound to the surface with 0, 1, or 2 terminal carboxylate groups also bound, respectively.

Figure 32 shows the distribution of molecular configurations for surface-bound citrate anions on 4, 6, and 8 nm AuNPs. For monolayered citrate^{3-}, the dominant configurations are 1-arm and 2-arm, which when combined make up ∼78% of the configurations. Approximately 38-51% of monolayered H_2citrate$^-$ are in the 2-arm configuration across AuNP sizes, which is consistent with previous experimental findings by ATR-FTIR [42] that intermolecular hydrogen bonding between terminal carboxylic acid groups of H_2citrate$^-$ stabilizes the citrate layer on AuNPs. The 1-arm and bridge configurations each make up ∼21-26% of monolayered H_2citrate$^-$ configurations. We find that the bridge configuration, previously attributed to citrate^{3-} at low packing density [43], is significantly present in monolayered H_2citrate$^-$. For the surface-bound layer on an AuNP coated with a bilayer of H_2citrate$^-$ (H_2citrate$^-$, saturated), the percent distribution of 2-arm configurations decreases, accompanied by commensurate increases in the percent distribution of tall and bridge configurations. We find that the distribution of these configurations in monolayered citrate^{3-}, monolayered H_2citrate$^-$, and saturated H_2citrate$^-$ does not change with respect to AuNP size.

As the surface-bound H_2citrate$^-$ layer becomes saturated, the changes in molecular

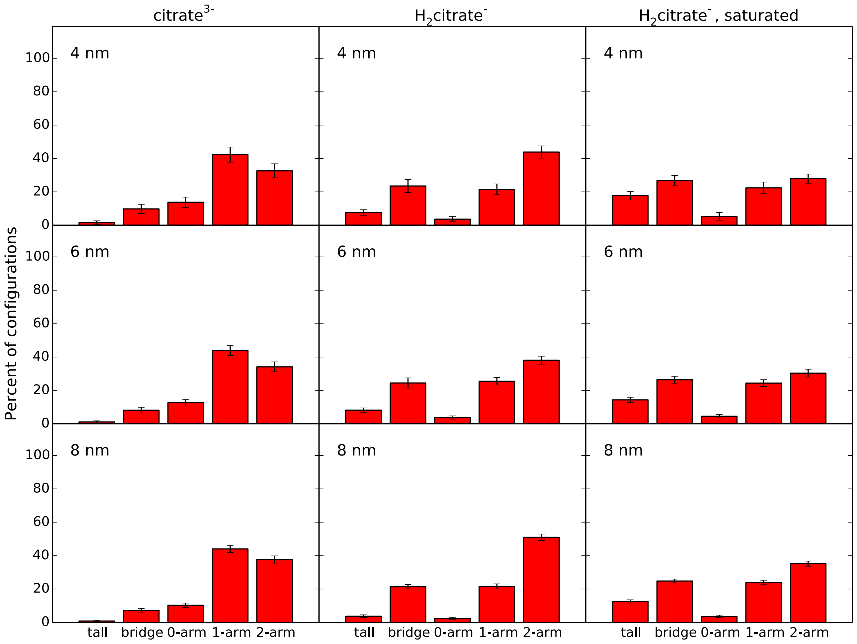

Figure 32: Distribution of molecular configurations in a monolayer of citrate^{3-}, monolayer of H_2citrate^{-}, and the saturated surface-bound layer of H_2citrate^{-} within bilayered H_2citrate^{-} on 4, 6, and 8 nm AuNPs in implicit solvent.

configurations reflect the need to maximize packing and promote bilayer formation. The bridge, 1-arm, and 2-arm configurations, each with at least one terminal carboxylic acid group bound to the AuNP surface, stabilize monolayered H_2citrate^{-}. The bridge configuration maximizes packing compared to 2-arm, which can explain the increase in the percent distribution of the bridge configuration and decrease in the percent distribution of the 2-arm configuration in response to saturating the H_2citrate^{-} layer. The percent distribution of the 1-arm configuration does not significantly change upon saturating the H_2citrate^{-} layer. The 1-arm configuration maximizes packing. It has one surface- bound and one free terminal carboxylic acid group that respectively stabilize the surface-bound layer and promote bilayer formation. Finally, there is a significant increase in the percent distribution of the tall configuration upon saturating the surface. The tall configuration has a free central carboxylate group and only one of the two terminal carboxylic acid groups bound, maximizing packing on the AuNP surface. One of the two free groups in the tall configuration can potentially hydrogen bond with a free group from another tall configuration or the free central groups in the bridge configuration, whereas the remaining free group can hydrogen bond with a dangling citrate in the second layer. Such intermolecular interactions thereby maximize packing, stabilize the surface-bound layer, and promote bilayer formation, while maintaining the ideal 2:1 surface-bound to dangling citrate organization.

6.3.3 Density and Stability of Citrate^{3-} and H$_2$citrate^{-} on 4 nm Cit-AuNPs and PAH-Cit-AuNPs.

We randomly distributed citrate^{3-} and H$_2$citrate^{-} equivalent to their maximum packing density on 4 nm AuNPs in a simulation box with the 4 nm AuNP fixed at the center. A steering force was applied on citrate^{3-} and H$_2$citrate^{-} onto 4 nm AuNPs in explicit TIP3P solvent at constant NPT until the anions were 7.5 Å from the AuNP surface for 20 ns. The citrate molecules were, then, kept frozen, and the solvent was equilibrated for 5 ns. The constraints on citrate were released, and the system was equilibrated for 10 ns. Finally, a production run of 5 ns was performed with data collected at 10 ps intervals.

The polycation PAH$_{200}$ was deposited on the equilibrated structures of cit-AuNPs along with desorbed excess citrate to test the stability of the citrate layers, and the system was resolvated in TIP3P solvent (Figure 33). A steering force was applied to PAH$_{200}$ toward the AuNP surface for 0.05 ns to promote adsorption of the polycation. The system was equilibrated for a total simulation time of 20 ns followed by a 5 ns production run. The numbers of adsorbed citrate molecules, following the construction and equilibration of cit- and PAH-cit-AuNPs, shown in Figures 34 and 35, do not

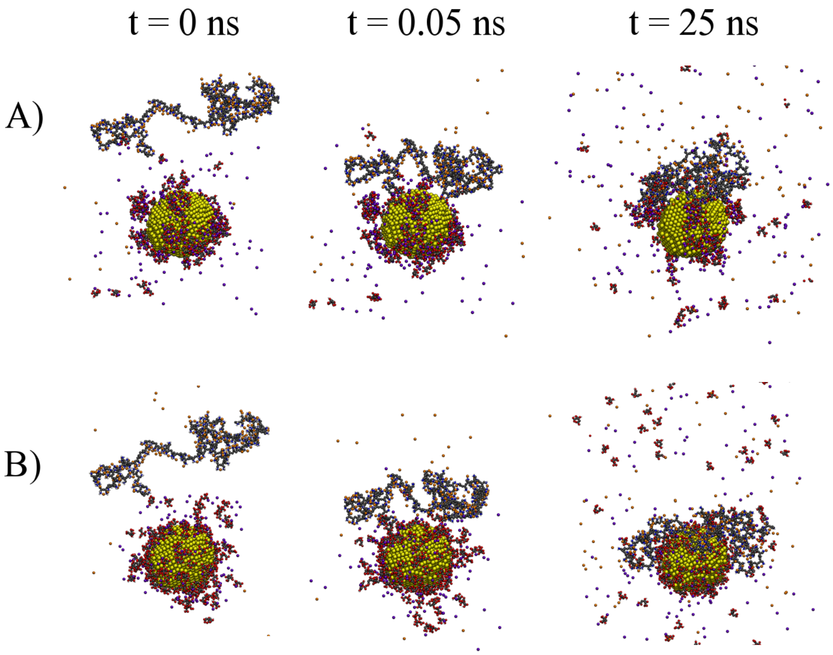

Figure 33: Simulation snapshots of (A) citrate^{3-} and (B) H$_2$citrate$^-$ layers on 4 nm AuNPs in the presence of PAH at the initial configuration (0 ns), after steering PAH to the AuNP surface (0.05 ns), and at the end of equilibration and production runs (25 ns). Gold (yellow), carbon (gray), oxygen (red), hydrogen (white), nitrogen (blue), sodium (purple), and chloride (orange) atoms are shown. Water molecules are not shown for clarity.

significantly change during the production runs.

In explicit solvent, we find that citrate^{3-} molecules do not adsorb into a monolayer (Figs. 29, 33, and A6.4). Rather, citrate^{3-} anions coordinate with Na$^+$ ions and distribute radially from the AuNP surface due to the accumulation of high surface charge density on the AuNP surface in agreement with previous simulations [177]. Because citrate^{3-} anions do not form a distinct monolayer in explicit solvent, we track the density and spatial distribution of citrate^{3-} by distance from the AuNP surface in 3.5 Å increments. We calculate that approximately 28 citrate^{3-} are directly bound to the surface of each AuNP (Figure 34). Beyond 17.5 Å, the number of citrate^{3-} between increments does not significantly change, indicating that there is a total of

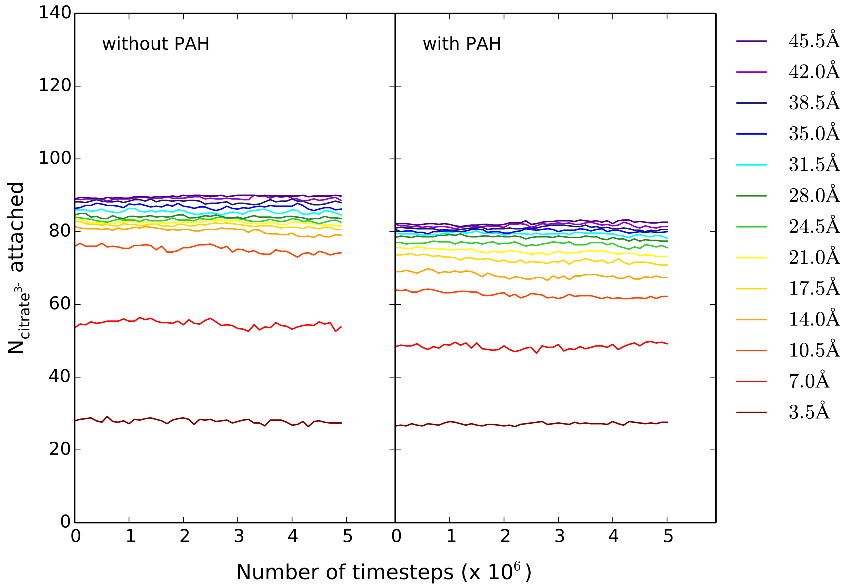

Figure 34: Number of citrate^{3-} within 3.5 Å incremental distances from the 4 nm AuNP surface *vs.* time in explicit solvent without and with PAH adsorbed. Each curve is an average of five trajectories. There are 27.9 ± 2.6 citrates directly bound to the surface on 4 nm citrate-coated AuNPs. Beyond 17.5 Å there is no significant change in the number of citrate between 3.5 Å increments, and free citrates are included in the count. There are 81.7 ± 2.9 citrates within 17.5 Å of the AuNP surface. The number of surface-bound citrate^{3-} is consistent at 27.2 ± 4.0 molecules near the AuNP surface, but overall number and spatial distribution of citrate^{3-} near the surface decrease upon adsorption of PAH.

approximately 82 citrate^{3-} in the adsorbed layer and a surface charge density of 8.1 $\times$ 10^{-10} mol/cm^2, distributed radially from face-dependent sites on the AuNP surface. The remaining citrate^{3-} in the simulation box are free in solution. The difference in the number of citrate^{3-} between increments signifies the number of citrate^{3-} per layer. This spatial charge distribution changes upon adsorption of PAH (Figure 34). The intermolecular interaction between citrate^{3-} through coordination with Na$^+$ ions becomes disrupted, and citrate^{3-} detaches from the AuNP surface, preventing complete adsorption of PAH (Figure A6.4).

The density of H$_2$citrate$^-$ bilayers is determined by the 3.5 Å Au–O cutoff distance for the first layer and an intermolecular O–H distance within 4.0 Å between surface-

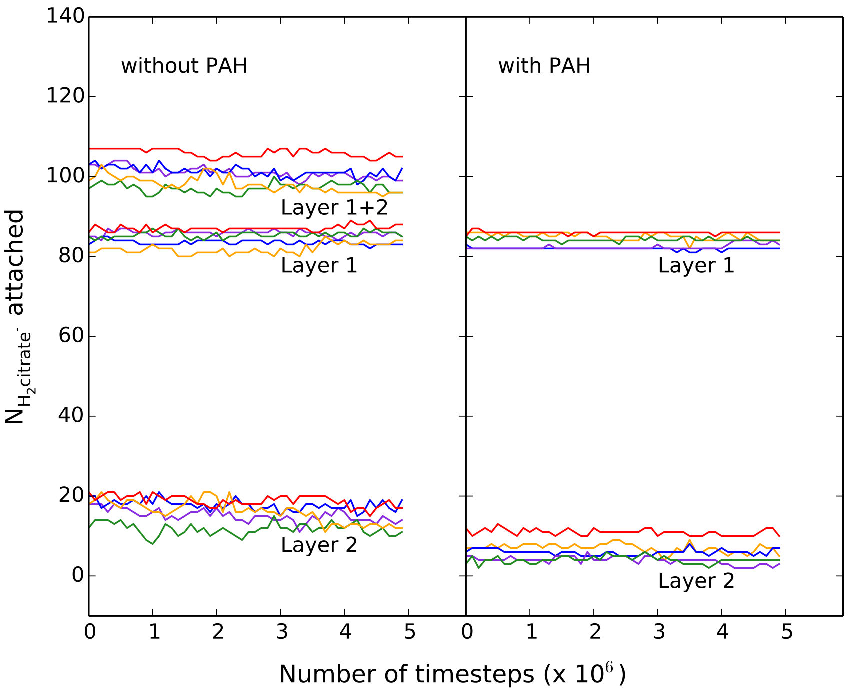

Figure 35: Number of $H_2citrate^-$ in the surface-bound layer (Layer 1), dangling second layer (Layer 2), and the total bilayer (Layer 1 + 2) on 4 nm AuNPs *vs.* time in explicit solvent without and with PAH adsorbed. Trajectories are distinguished by color with no association between like colors in different panels. The number of $H_2citrate^-$ in Layer 1 is 84.7 ± 2.1 without PAH and 83.9 ± 1.7 $H_2citrate^-$ with PAH adsorbed. The total number of $H_2citrate^-$ in the bilayer on 4 nm AuNPs is 100.7 ± 3.3 without PAH and 90.3 ± 3.9 $H_2citrate^-$ with PAH adsorbed.

bound and unbound $H_2citrate^-$ for the second layer. The density of $H_2citrate^-$ and surface charge density are 3.3×10^{-10} and 3.3×10^{-10} mol/cm^2, respectively (Figure 35). We find that the dangling second layer of $H_2citrate^-$ is easily displaced by PAH, but the surface-bound layer is highly stable (Figure 35). The density of the surface-bound $H_2citrate^-$ layer remains fixed with a surface charge density of 2.8×10^{-10} mol/cm^2, and the total surface charge density of the $H_2citrate^-$ bilayer is 3.0×10^{-10} mol/cm^2 upon adsorption of PAH.

The stability of the $H_2citrate^-$ layer on AuNPs is in agreement with previous ATR-FTIR experiments, which found that the citrate layer on AuNPs is resistant to thiol functionalization [160], and suggests that citrate anions are in the H_2citrate$^-$ state on AuNPs. Figure A6.5 qualitatively shows that PAH_{200} forms surface-bound segments, specifically 1–2-monomer loops or kinks, upon adsorption onto cit-AuNPs, as reported in our previous simulations [24] and discussed in Chapter 5. These surface-bound structures are consistent across a range of AuNP surface charge densities provided that the citrate anions remain stable on the AuNP surface, as is the case with H_2citrate$^-$. The lower surface charge density on cit-AuNPs determined in this work only changes the structures of the dynamic solvent-exposed segments, such as the length of longer loops and tails in the adsorbed PAH, but which do not affect the mesoscale interactions of long-chain polyelectrolytes such as observed in our prior work [24].

6.3.4 Molecular Configurations of Citrate^{3-} and H_2citrate$^-$ on 4 nm Cit-AuNPs and PAH-Cit-AuNPs.

The distribution of citrate^{3-} configurations on gold differs between implicit and explicit solvents, but the distribution of H_2citrate$^-$ is in agreement between the solvent conditions (Figs. 32 and 36). The different distribution of citrate^{3-} configurations between implicit and explicit solvent is attributed to differences in structure observed between solvent conditions.

Comparison of the distribution of molecular configurations between citrate^{3-} and H_2citrate$^-$ in explicit solvent suggests that the tall configurations [43] previously reported to be on 4 nm cit-AuNPs based on ^{13}C SSNMR indicate the presence of either citrate^{3-} or H_2citrate$^-$, but larger contribution by H_2citrate$^-$. The bridge configurations [43] are exclusive to and indicate the presence of H_2citrate$^-$ (Figure 36). The oxygen atoms in the central carboxylate and hydroxyl groups of citrate are solvent-exposed in the tall and bridge configurations. Of the 0-, 1-, and 2-arm configurations observed in the

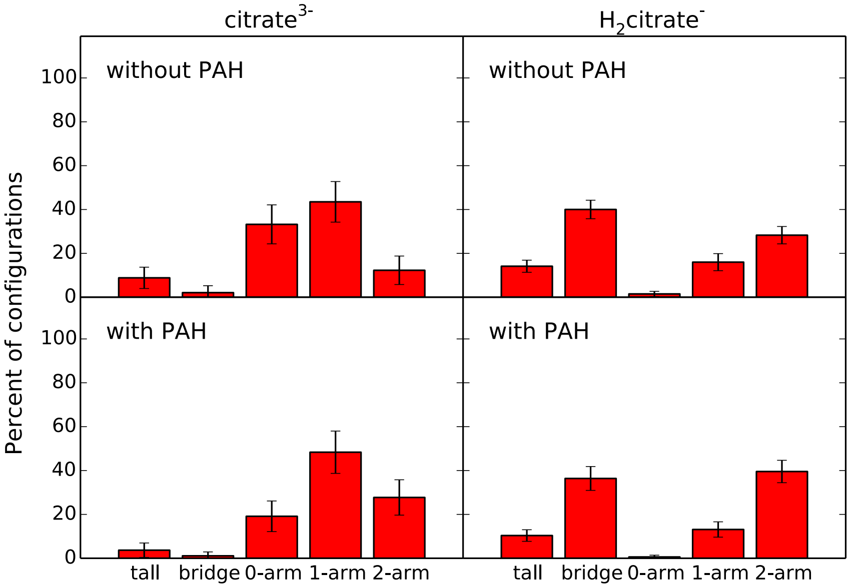

Figure 36: Distribution of molecular configurations in surface-bound citrate^{3-} and H_2citrate$^-$ on 4 nm AuNPs in explicit solvent without and with PAH adsorbed.

simulations, we determined whether a central carboxylate oxygen, the central-hydroxyl oxygen, or both are bound to the AuNP surface. We find that all hydroxyl oxygens in citrate^{3-} are bound to the surface, exposing the carboxylate groups to solvent to coordinate with Na^+ ions and that a small percentage of the hydroxyl oxygen in H_2citrate$^-$ is free (Figure A6.6). These configurations are in agreement with previous simulations of citrate^{3-} adlayers on an Au(111) surface [177] and with ATR-FTIR experiments [42], which found that the hydroxyl group is free below pH 9, and that citrate^{3-} binds to the AuNP surface *via* both hydroxyl and carboxylate groups above pH 11.14.

Upon adsorption of PAH, we observe a decrease in the surface-bound layer of the least stable citrate^{3-} configurations, tall and 0-arm, which only have one carboxylate or hydroxyl group bound. For H_2citrate$^-$, there is a slight decrease in bridge, tall, and 1-arm configurations and an increase in 2-arm configurations. The intermolecular hydrogen bonding between 2-arm H_2citrate$^-$ configurations stabilizes not only the adsorbed citrate anions within the citrate layer but also the interface between the citrate monolayer and adsorbing cationic molecules.

We performed *in situ* ATR-FTIR on multilayered PAH-cit-AuNPs to understand the coordination between citrate within the anionic citrate layer and between the anionic citrate layer and adsorbing polycation layer. Figure 37 shows ATR-FTIR spectra of PAH-cit-AuNPs in solution and after drying. In the region between 3600 and 2800 cm^{-1}, the peak at 3440 cm^{-1} is assigned to the O–H stretching in water clusters that are hydrogen bonded to carboxylic acid groups [181]. After the sample of PAH-cit-AuNPs is dried, this peak for the water clusters disappears, and the peak at 3385 cm^{-1} is assigned to N–H stretching in PAH [182]. The small peaks at 3041 and 2600 cm^{-1} indicate O–H stretching between hydrogen-bonded carboxylic acid groups [42, 183], which shift slightly after drying the sample. The peak at 2937 cm^{-1} suggests either O–H stretching from the carboxylic acid group in citrate or a C–H stretch [183].

In the fingerprint region, characteristic peaks at 1734 and 1704 cm^{-1} for carbonyl stretches in carboxylic acid dimers were isolated by Park and Shumaker-Parry [42] after sealing surface-bound H_2citrate$^-$ hydrogen bonded to a dangling H_2citrate$^-$ using long-chain alkanethiols. Our simulations show that the dangling H_2citrate$^-$ layer is displaced upon adsorption of PAH and, thus, this peak is not observed in our FTIR spectra of PAH-cit-AuNPs. The peaks between 1277 and 1261 cm^{-1} are assigned to C–OH stretching in the carboxylic acid group of H_2citrate$^-$ [183, 184]. The peak at 1614 cm^{-1} that shifts to 1603 cm^{-1} in the dried sample is assigned to ν(C=OO$^-$) from a salt-bridge formation between a carboxylate group in citrate and $NH_3{}^+$ group from PAH, as was previously observed in FTIR spectra of the amino acid glycine ($NH_3{}^+CH_2COO^-$)

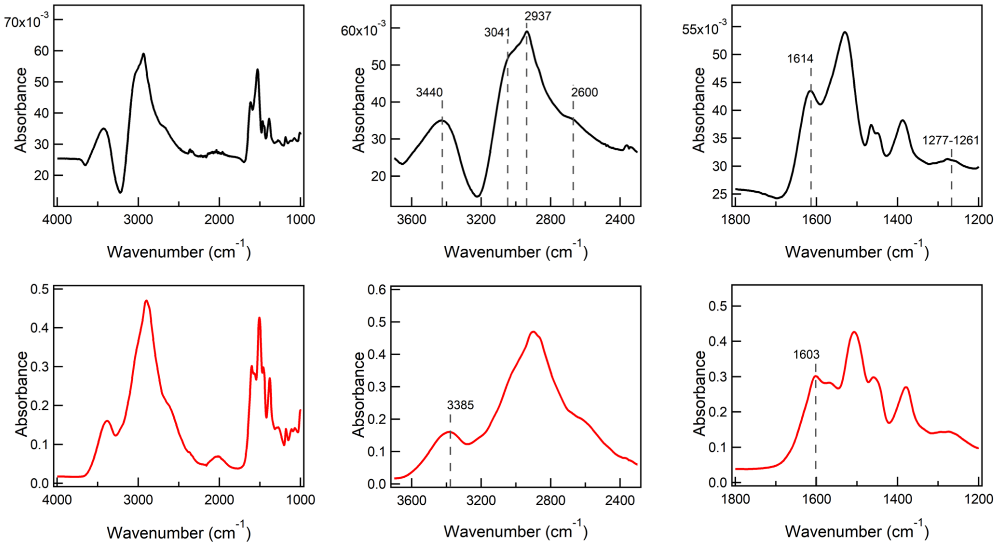

Figure 37: ATR-FTIR spectrum of PAH-cit-AuNPs in solution (top row) and dry (bottom row): the full (from 4000 to 1000 cm^{-1}), OH region (from 3700 to 2300 cm^{-1}), and fingerprint region (from 1800 to 1200 cm^{-1}) spectra are shown from left to right.

[183]. These peak assignments are in agreement with simulations showing that 40% of H_2citrate$^-$ on the AuNP surface is in the bridge configuration with terminal carboxylic acid groups bound to the surface, leaving the central carboxylate group free to interact with PAH (Figure 36). ATR-FTIR experiments combined with molecular dynamics simulations on multilayered PAH-citrate-coated AuNPs further show the importance of H_2citrate$^-$, particularly the bridge configuration, in stabilizing the citrate layer *via* hydrogen bonding of terminal carboxylic acid groups and the interface between the citrate layer and adsorbing polycation *via* salt-bridge formation between the central carboxylate group of citrate and amine group of PAH. This analysis on the coordination of the polycation PAH with amine terminal groups can be broadly applied to study association of protein coronas on cit-AuNPs.

6.4 Conclusion

We characterize the structure, stability, and density of citrate^{3-} and H_2citrate$^-$ on AuNPs, using molecular dynamics simulations. For structure, we find the distribution of tall, bridge, and 2-arm configurations, which are analogous to binding modes of citrate reported in the literature [42, 43].

Through implicit-solvent simulations, we confirm that the population of tall configurations increases with increasing packing density [43] and that the distribution of configurations sampled and packing density are independent of AuNP size. Both citrate^{3-} and H_2citrate$^-$ can be in the tall configuration, as shown in explicit solvent, but this configuration is more significantly adopted by H_2citrate$^-$. For citrate^{3-}, the tall configuration can serve to maximize charge separation at high surface charge density. For H_2citrate$^-$, the tall configuration maximizes packing, stabilizes the monolayer, and promotes bilayer formation. We find that the bridge configuration is only adopted by H_2citrate$^-$ and suggest its significance in stabilizing the monolayer and increasing packing. There is a significant presence of the 2-arm configuration compared to other configurations for H_2citrate$^-$ in agreement with previous ATR-FTIR experiments [42], as the terminal carboxylic acid groups of H_2citrate$^-$ in this configuration participate in intermolecular hydrogen bonding to stabilize the AuNP surface. However, there is a greater cumulative distribution of 1-arm, tall, and bridge configurations that maximizes packing, thereby yielding a greater density than previously predicted [42].

We use a combination of molecular dynamics simulations and *in situ* ATR-FTIR experiments to characterize the citrate layer of 4 nm PAH-cit-AuNPs. ATR-FTIR experiments confirm the presence of H_2citrate$^-$ within PAH-cit-AuNPs and agree with configurations between citrate molecules and between citrate and PAH predicted by simulations. We find that the H_2citrate$^-$ layer is highly stable upon PAH adsorption in simulations. In particular, there is a high population of bridge configurations that enables intermolecular hydrogen bonding between citrate *via* terminal carboxylic acid groups and salt-bridge formation between the free central carboxylate group in citrate and the amine group in PAH. In contrast, the citrate^{3-} layer is disrupted, and removal of citrate^{3-} from the AuNP surface is observed in the presence of an adsorbing cationic molecule, highlighting the differences in the stability of citrate^{3-} and H_2citrate$^-$ layers, particularly at charged interfaces. The similarity of the distributions between H_2citrate$^-$ and citrate^{3-} configurations across AuNP sizes in implicit solvent, of the distributions of H_2citrate$^-$ configurations between implicit and explicit-solvent conditions, and in the structure of citrate^{3-} layers on 4 nm AuNPs and on planar Au(111) surfaces [177] suggests similar structure of citrate layers in larger-sized nanoparticles and local response to adsorbing charged molecules at the site of adsorption. For larger-sized nanoparticles, the adsorption of multiple polycations or protein coronas must also be considered, and we obtained an all-atom structure for the H_2citrate$^-$ layer and charge density useful for bottom-up coarse-graining simulations of these larger-scale systems.

We determine the density of citrate^{3-} on the AuNP surface to be 2.7×10^{-10} mol/cm^2 and the surface charge density to be 8.1×10^{-10} mol/cm^2, spatially distributed across 17.5 Å radially from the AuNP surface. However, this spatial charge distribution fluctuates upon adsorption of charged molecules. We determine the density of bilayered H_2citrate$^-$ to be 3.3×10^{-10} mol/cm^2. Upon PAH adsorption, the density of monolayered H_2citrate$^-$ remains consistent at 2.8×10^{-10} mol/cm^2 with H_2citrate$^-$ distributed nonuniformly in a face-dependent manner, and total density and surface charge density decrease to 3.0×10^{-10} and 3.0×10^{-10} mol/cm^2, respectively, due to some displacement of the dangling, second H_2citrate$^-$ layer by PAH. These values of citrate density and surface charge density are significantly lower than predicted from experimental characterization in dried samples of cit-AuNPs [12, 162]. The stability of H_2citrate$^-$ layers justifies the use of fixed-charge models for the representation of the citrate layer in simulations. This also provides an all-atom level determination of the distribution of configurations and coordination modes of citrate predicted by experiment in as-synthesized, functionalized, and transformed cit-AuNPs.

Chapter 7

Bottom-Up Coarse-Graining of Structurally Complex Nanoparticles and Lipid-Bilayer Systems

7.1 Introduction

In Chapters 4 and 5, we showed that typical synthesized or engineered nanoparticles (NPs), such as alkanethiol- and polyelectrolyte-coated gold nanoparticles (AuNPs), have non-uniform spatial charge and hydrophobic-group distributions on their surfaces [24, 23]. We expect this non-uniformity to play an important role in interactions of AuNPs with lipids, which have distinct spatially distributed hydrophobic head- and hydrophilic tail-groups. Previous studies have revealed that lipid extraction by NPs [26] and NP translocation through lipid bilayers [130] require high energy barriers. Nanoparticle transformations at the nanoparticle-lipid bilayer interface are, thus, rare events that are difficult to observe or sample at the ns-μs timescales accessible by molecular dynamics simulations, and coarse-grained simulations are required. Top-down coarse-grained models of NPs have focused on NPs with spatially uniform displays of their ligands and charged head groups [172, 174, 185, 186, 187]. Through our bottom-up approach, we create structurally benchmarked NP models that address the non-uniform layering on NP surfaces and lipid-vesicle models of various sizes.

We use dissipative particle dynamics (DPD) for our coarse-grained simulations. DPD is a coarse-grained simulation method developed to predict the hydrodynamic behavior of complex fluids and soft matter at long time- and length-scales [153, 154, 188]. Similar to the MARTINI force field [152], the DPD coarse-graining scheme that we implement groups roughly three neighboring heavy atoms with similar chemical properties into larger beads of equal volume, reducing the atom count and increasing accessible length-scales, accordingly. DPD uses a soft, linearly-repulsive conservative force, $\mathbf{F}_{ij}^{C}$, for pairwise nonbonded interactions between any bead i and neighboring bead j within a cutoff distance r_c, allowing for larger timesteps and for simulations to reach time-scales inaccessible to all-atom molecular dynamics (MD) and longer time-scales compared to MARTINI coarse-grained simulations:

$$\boldsymbol{F}_{ij}^{C} = \begin{cases} a_{ij}\left(1 - r_{ij}/r_c\right)\hat{\boldsymbol{r}}_{ij}, & r_{ij} < r_c \\ 0, & r_{ij} \geq r_c \end{cases} \quad (1)$$

where a_{ij} is a parameter that defines the degree of repulsion between bead types. Further, DPD is flexible in the number of heavy atoms grouped and the volume per bead and can be readily re-parameterized accordingly [189, 190, 191, 192, 193]. Combining the conservative force with a random force and dissipative force [154, 188] and tuning the force contributions from bond stretches and angle bends between neighboring beads, DPD simulations can capture the structural properties of lipid membranes [192, 194, 195], the swelling behavior of hydrogels [196], and the rheology of red blood cells [193, 197]. In these applications, charged groups and water molecules are modeled as charge-neutral hydrophilic beads with the repulsive parameter a_{ij} tuned to reproduce the separation of hydrophilic and hydrophobic phases in bulk soft matter.

Increasingly, DPD is being used to model and understand local interactions at the interface of nanoscale materials and lipid-bilayer systems, where charge and local pH effects influence the interactions [22, 143]. Both MARTINI and DPD coarse-grained simulations have been used in parallel to determine design rules for the surface chemistry of nanoparticles to control nanoparticle assembly and penetration into lipid membranes [130, 131, 134, 173, 174, 186, 198, 199]. Vesicles made up of 270-2300 lipids and membrane-wrapped nanoparticles [200] have also been modeled as potential vectors for biologically noninvasive transport and delivery of drug molecules and nanoparticles [199, 201, 202, 203]. These simulations are inherently mesoscale: they predict molecular mechanisms of nanomaterial function and the physiological processes of lipid bilayers more generally, such as vesicle formation and fusion to membranes [204, 205, 206], that are difficult to validate bottom-up from the atom-scale resolution using MD simulations [22] and top-down by experiment [6].

Moreover, the DPD force-field parameters developed for our NP and lipid-vesicle models are described in Section 7.2. The structural benchmarking of NP models is discussed in Section 7.3.1. We employ a suite of all-atom MD, MARTINI, and DPD simulations with the inclusion of electrostatic interactions [207] to compare the structure and stability of vesicles across a range of sizes at varying particle resolution in Section 7.3.2.

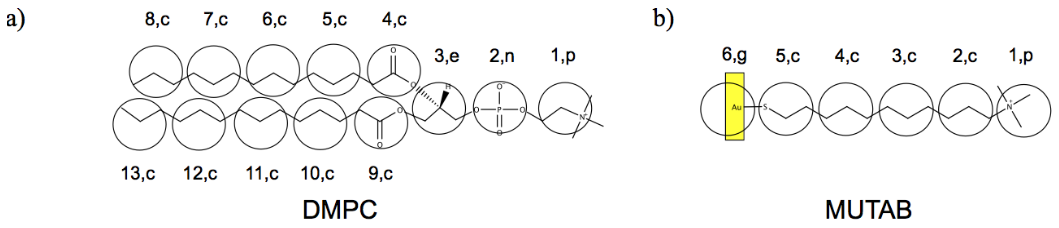

Figure 38: Coarse-graining scheme for a) lipids and b) ligands overlaid on the molecular structures with DPD beads labeled by "bead number, bead type". The bead types are the positively charged quaternary ammonium group (p), negatively charged phosphate group (n), glycerol group ester-linked to the lipid tails (e), CH_2 and CH_3 groups in the lipid tails and ligand chains (c), and gold (g).

7.2 Materials and Methods

7.2.1 Simulation Setup

For coarse-grained DPD simulations, three heavy atoms are mapped to one coarse-grained bead with a bead volume of 90 Å^3. This mapping scheme is illustrated in Figure 38. Reduced units are used with the pairwise-interaction cutoff distance, r_c, set to 1.0 for distance units, and the mass of each coarse-grained bead and time unit τ are also set to unity. The unit of energy, $\varepsilon = k_B T$ (at $T = 300$ K), is set to unity, and thereby, the reduced temperature $T^* (= k_B T/\varepsilon) = 1$. Harmonic potentials are used to describe the bond stretch between two beads, i and j, and the angle bend between three beads i, j, and k around their equilibrium values in the form $U_{bond} = K_{ij}(r_{ij} - r_{eq})^2$ and $U_{angle} = K_{ijk}(\theta_{ijk} - \theta_{eq})^2$, respectively. For nonbonded interactions, the DPD conservative force $\mathbf{F}_{ij}^{C}$ (Eq. 1) and an electrostatic force $\mathbf{F}_{ij}^{E}$ (Eq. 2) [207] are used and combined with

$$\boldsymbol{F}_{ij}^{E} = \frac{q_i q_j}{4\pi\varepsilon\varepsilon_0}\begin{cases}\dfrac{1}{{r_{ij}}^2}\sin^6\left(\dfrac{2\pi r_{ij}}{4D}\right), & r_{ij} < D\\[2ex] \dfrac{1}{{r_{ij}}^2}, & D \le r_{ij} < r_c\end{cases} \qquad (2)$$

random and dissipative forces [154] implemented into the DPD thermostat in LAMMPS [116]. For the electrostatic force, charged beads are assigned a $+1$ or -1 charge, and D is set to 0.65, as previously described [207]. The relative permittivity, ε, of the water solvent is 78.3, and ε_0 is the vacuum permittivity.

A bead density of $\rho = 3$ is used for simulations; that is, the total number of DPD beads in the system is equal to three times the box volume (in units of r_c^3). The nonbonded interaction parameter, a_{ij}, between solvent beads is set to 25 in reduced energy units to reproduce the compressibility of water at 300 K. With this bead density and solvent parameter, r_c is equivalent to 6.46 Å in real units [192], and this conversion is used to present the results. The parameters used for nonbonded, bond-stretch, and angle-bend interactions are presented in Tables 2 and 3.

	p	n	e	c	g	water	ions
p	35	35	35	80	80	25	25
n		35	35	80	80	25	25
e			35	80	80	25	25
c				25	80	80	80
g					25	80	80
water						25	25
ions							25

Table 2: DPD nonbonded parameters, a_{ij}, (Eq. 1) between bead types, as described in Figure 38.

Bond Stretch

Bond type		K_{ij} (k_BT)	r_{eq} (r_c)
	MUTAB- and MUA-AuNPs		
1	1-2, 2-3, 3-4, 4-5, 5-6	100	0.7
	DMPC lipids		
1	1-2, 2-3 3-4, 4-5, 5-6, 6-7, 7-8 3-9, 9-10, 10-11, 11-12, 12-13	100	0.7

Angle Bend

Angle type		K_{ijk} (k_BT)	θ_{eq} (deg)
	MUTAB-and MUA-AuNPs		
1	1-2-3, 2-3-4, 3-4-5, 4-5-6	6.0	180.0
	DMPC lipids		
1	4-5-6, 5-6-7, 6-7-8 9-10-11, 10-11-12, 11-12-13	6.0	180.0
2	2-3-4, 2-3-9, 3-4-5, 3-9-10, 4-3-9	3.0	120.0
3	1-2-3	1.0	180.0

Table 3: DPD bond-stretch and angle-bend parameters between bead numbers, as described for DMPC lipids and MUTAB ligands in Figure 38. MUA is the anionic analog of MUTAB. “1-2” denotes the bond between bead 1 and bead 2. “1-2-3” denotes the angle between bonds “1-2” and “2-3” with central bead 2 as the vertex of the angle.

7.2.2 Coarse-Grained Nanoparticle and Lipid-Vesicle Models

The three heavy atoms to one coarse-grained bead mapping and bead volume of 90 Å^3 result in a ligand density of 4.8 molecules/nm^2 on a 4 nm spherical shell for the NP in agreement with experiments [23]. The alkanethiol ligands were grafted uniformly on the spherical NP shell, and the interactions of NPs and zwitterionic 1,2-dimyristoyl-sn-glycero-3-phosphocholine (DMPC) lipids were modeled using force-field parameters modified from those developed by Smit and co-workers [192] for DMPC lipids (Tables 2 and 3) with electrostatic interactions [207] incorporated (Eq. 2).

We constructed 288-, 576-, 1500-, and 4000-DMPC lipid vesicle models by preparing planar membranes with equal number of lipids in the upper and lower leaflets and surrounding all sides, including the hydrophobic edges, with water using Packmol [115]. We ran ten simulations for each condition, and the membranes self-assembled into vesicles [191].

7.3 Results and Discussion

7.3.1 Structural Benchmarking of Non-Uniformity in Self-Assembled Monolayers and Polycations on Gold Nanoparticles

The DPD force-field angle parameters were tuned for alkanethiol ligands (Table 3). From an initial uniform spatial distribution of MUTAB ligands, the ligand layer self-assembled into spatially segregated ordered domains, as observed in the all-atom molecular dynamics simulations reported in Chapter 4 (Figure 39).

Likewise, we took a bottom-up approach to create DPD coarse-grained models for polyelectrolyte wrappings on citrate-coated AuNPs described in Chapters 5 and 6. We distributed negatively charged beads on the spherical NP shell at the H_2citrate$^-$ density determined in Chapter 6 to represent the citrate-coated AuNP surface. We implemented the coarse-grained mapping scheme in Section 5.2.3 of Chapter 5 and nonbonded parameters for hydrophobic (“c”) and hydrophilic beads (“p”) (Table 2) and tuned angle parameters along the polymer backbone to reproduce the adsorption of PAH_{200} onto AuNPs with hemispheric NP coverage and heterogeneous, dynamic segments on the NP surface (Figure 40).

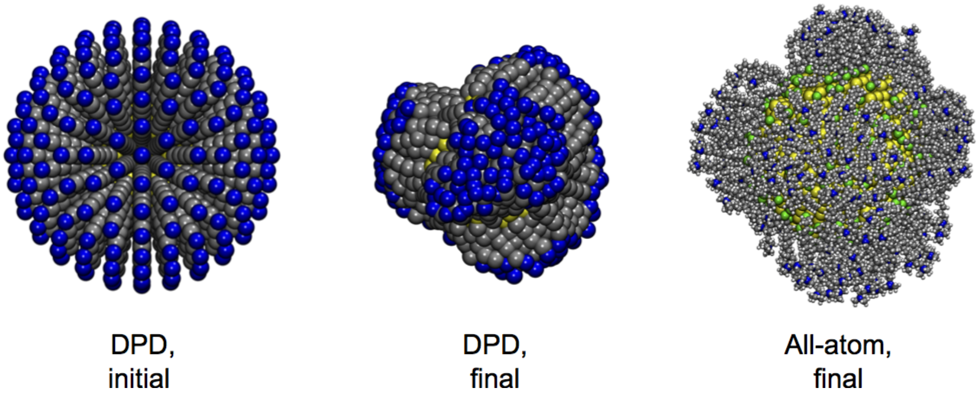

Figure 39: Self-assembly of a DPD coarse-grained MUTAB alkanethiol monolayer into spatially non-uniform ordered domains observed in all-atom simulations.

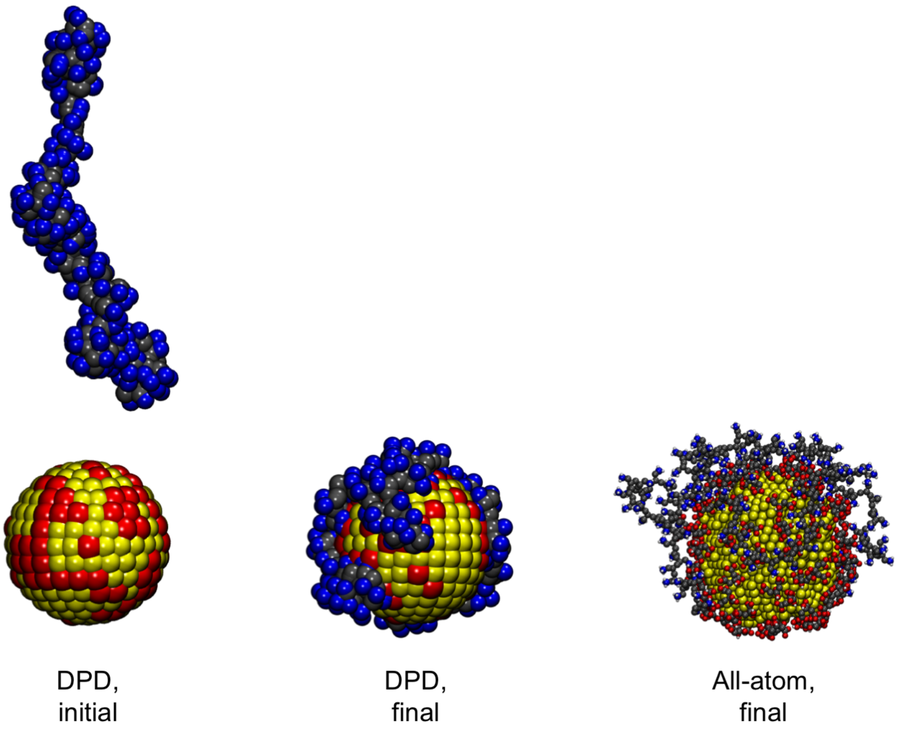

Figure 40: Adsorption of DPD coarse-grained PAH_{200} onto AuNPs with incomplete hemispheric coverage and dynamic, looping segments observed in all-atom simulations.

7.3.2 Correspondence and Predictability in Vesicle Size and Structure across All-Atom, MARTINI, and Dissipative Particle Dynamics Simulations

The number of lipids in the inner layer and outer layer of a vesicle and the number of water molecules inside the vesicle were counted from the last frame of each vesicle self-assembly simulation and averaged across all simulations. The assembly of planar membranes into vesicles occurs on the time-scale of hundreds of nanoseconds to microseconds [191], which is generally not accessible by all-atom molecular dynamics (MD) simulations.

Therefore, we reverse engineered an all-atom DMPC lipid vesicle from the structural characteristics–the average number of lipids in each layer and water inside the vesicle–of the smallest 288-DMPC lipid vesicle assembled from the DPD coarse-grained simulations. All-atom DMPC lipids and TIP3P water molecules were packed, using Packmol [115], to form an initial spherical vesicle. All-atom MD simulations were run using LAMMPS [116] and the CHARMM36 force field [208] and equilibrated at constant NPT under 1 atm at 300 K with a 2 fs timestep. Both the all-atom and DPD 288-lipid vesicles equilibrated to non-spherical structures with planar regions along the vesicle surface (Figure 41). This deviation from a spherical vesicle structure is attributed to the high bending resistance of smaller vesicles with high surface curvatures [209, 210].

With greater than 576 lipids, vesicles become spherical, and the spherically symmetric structural properties relative to the vesicle's center of mass, as well as dynamical properties, can be determined as a function of vesicle size. For example, we calculated the lipid tail end-to-end distance per lipid tail in each vesicle by taking the difference in the radial coordinates (relative to the vesicle COM) of the lipid glycerol bead and final tail bead. Negative values represent lipids in the inner layer, and positive values represent lipids in the outer layer of the vesicle. We calculated the frequency of lipid tail

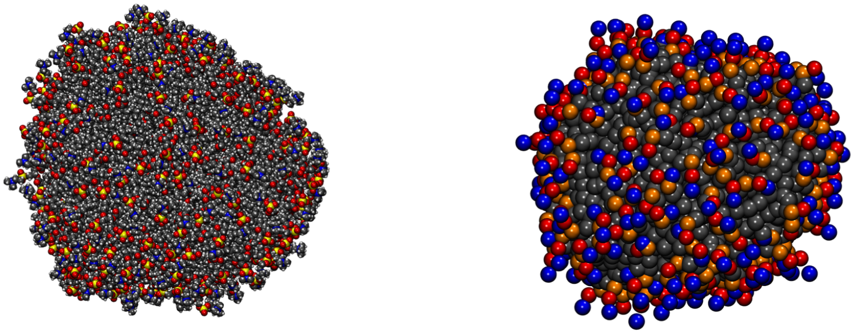

Figure 41: Representative snapshots of 288-DMPC lipid all-atom (left) and DPD coarse-grained (right) vesicles. For the all-atom vesicle, nitrogen atoms are shown in blue, phosphorus atoms in yellow, oxygen atoms in red, carbon atoms in gray, and hydrogen atoms in white. For the DPD vesicle, coarse-grained ammonium-group beads are in blue, phosphate groups in red, glycerol beads in orange, and lipid-tail beads in gray.

end-to-end distances and normalized by the total number of frames sampled such that a value of 1 represents one instance in each frame (Figs. 42 and A7.1 in the Appendix).

The distribution of lipid tail end-to-end distances indicates the local packing of lipids in the vesicle. Figure A7.1 shows vesicle size- dependent lipid packing. As the number of lipids in the vesicle (*i.e.* vesicle size) decreases, there is a higher frequency of smaller end-to-end distances to induce curvature. Our collaborators, Cui and co-workers, provided preliminary data from vesicle self-assembly simulations, starting from 4000 lipids and using the finer-grained MARTINI lipid models [152], to benchmark the DPD coarse-grained models. The distribution of lipid tail end-to-end distances is in agreement between MARTINI and DPD vesicles (Figure 42).

The radial distribution function, *g(r)*, between the the vesicle center of mass and the ammonium, phosphate, glycerol, lipid-tail groups were computed for each vesicle size (Figs. A7.2, A7.3, and A7.2). Vesicles with 576, 1500, and 4000 lipids yield sizes of ~10, 16, and 24 nm in diameter, respectively. They also have a membrane thickness of 4 nm in agreement with experimental and simulated values [191].

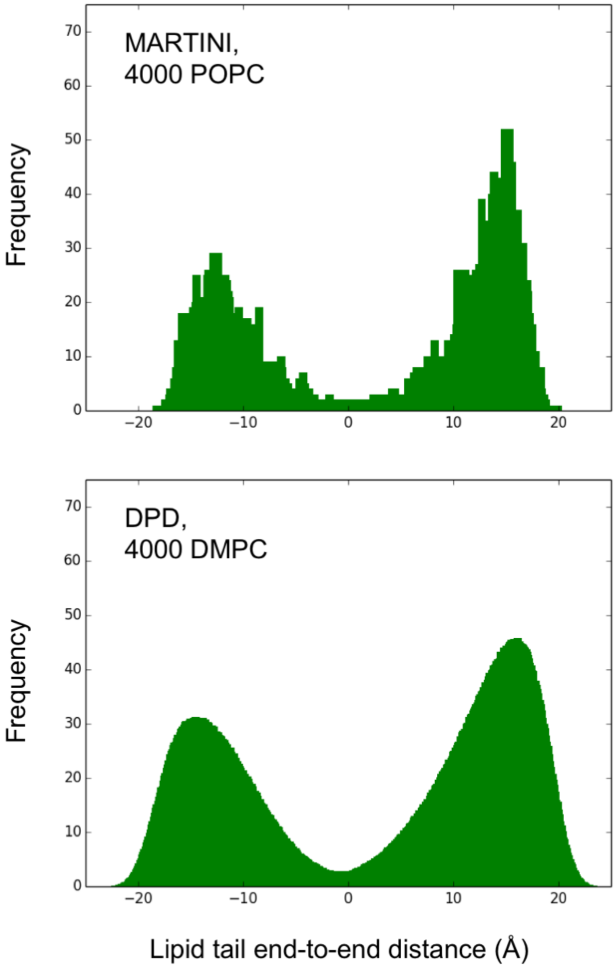

Figure 42: Distribution of lipid tail end-to-end distances in 4000-lipid, 25 nm MARTINI and DPD coarse-grained vesicles.

The average number of lipids counted in the inner layer of each vesicle and size of the inner layers determined from the $g(r)$'s were used to calculate the area per lipid (Figure 43). The area per lipid in the inner layer of each vesicle is consistently 0.66 nm^2 in agreement with experimental values for DMPC lipids [191], suggesting that the inner layer dictates the size of vesicles with a predictable size-independent lipid count. The number of lipids in the outer layer of vesicles, however, should be size-dependent with more lipids in the outer layer at smaller vesicle sizes and higher curvature and with

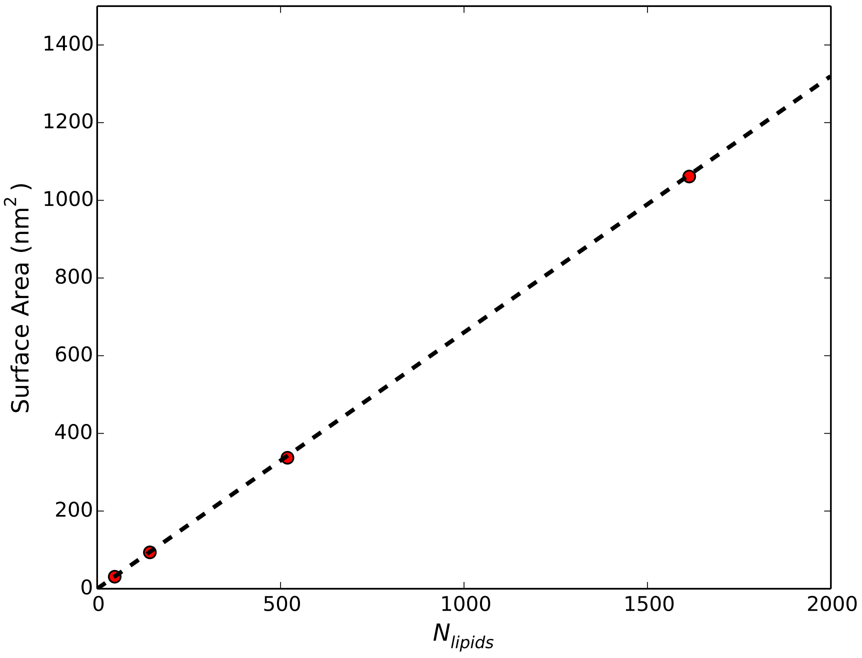

Figure 43: Average number of lipids (red dots) and surface area for the inner layer of vesicles self-assembled from 288-, 576-, 1500- and 4000-lipid planar membranes. The black dashed line fits the equation Area = 0.66*N_{lipids}, in agreement with the area per lipid of 0.66 nm^2/lipid determined experimentally for DMPC lipids [191].

roughy equal number in each layer for larger vesicles and smaller curvature. Stelter and Keyes have suggested Equation 3 that follows the size-dependent lipid count in the outer layer, N_{outer}:

$$(N_{outer} - N_{inner})/N_{inner} = b \exp(\text{-}cR^d) \qquad (3)$$

where N_{inner} can be determined for any desired inner vesicle radius R given the area per lipid (*e.g.* 0.66 nm^2/DMPC lipid) and $b = 11.026$, $c = 1.537$, and $d = 0.296$ are fitted parameters [200]. Using Eq. 3, we constructed a stable 60 nm (in diameter) vesicle (Figure 44)–the smallest isolatable vesicle size reported in the literature with which the membrane dynamics can be probed *via* neutron spin-echo spectroscopy [211]. Thereby, the 60 nm vesicle model can be used in future work to benchmark our DPD force-field parameters for the dynamical properties of vesicles.

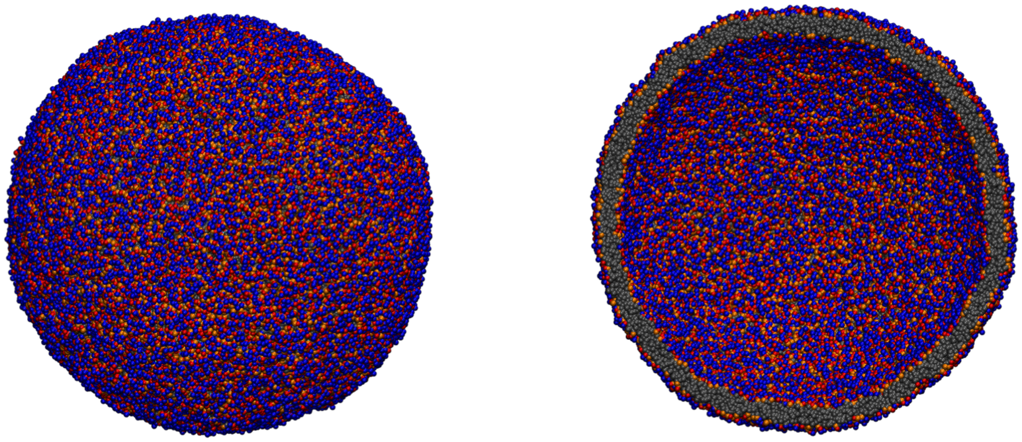

Figure 44: Representative snapshot (left) and cross section (right) of a 60 nm DPD coarse-grained vesicle.

7.4 Conclusion

We have used all-atom and MARTINI simulations to benchmark both the size-dependent structural properties of vesicles and the non-uniform structure of self-assembled monolayers and polyelectrolyte wrappings on AuNPs, constructed using our newly developed DPD force-field parameters (Tables 2 and 3). Together, these NP and lipid vesicle models can be implemented in coarse-grained DPD simulations to determine the mechanisms of NP transformations and biological impacts.

Chapter 8

Non-Uniformity in Nanoparticle Surface Chemistry Drives Lipid Corona Formation

8.1 Introduction

As shown in Chapters 4 and 5, alkanethiol- and polyelectrolyte-coated gold nanoparticles (AuNPs) each have unique surface layering and distributions of hydrophobic and charged groups due to both the ligand structure and method of functionalization. Alkanethiol ligands are grafted and form a monolayer on the AuNP surface. Depending on the alkyl chain length and AuNP surface curvature, alkanethiol ligands can segregate into ordered domains, or ligand islands, creating defects in the monolayer and exposing hydrophobic ligand chains on the edges of ligand islands [23, 110]. Polyelectrolytes electrostatically adsorb onto anionic AuNP surfaces to form solvent-exposed loops [24], and can detach [135]. Such differences could explain the different toxicological responses in bacteria to alkanethiol- *vs.* polycation-coated AuNP exposure [11] and transformations observed experimentally upon interaction with lipid vesicles [37].

In particular, the experiments that probe interactions of AuNPs with model one-or two- component lipid-vesicle systems are at the scale and complexity with which we can decipher the mechanistic differences in AuNP transformations as a function of the surface chemistry, using coarse-grained simulations. These experiments, in which AuNPs functionalized with either the alkanethiol MTAB or the polyelectrolyte PAH were retrieved after incubation with lipid vesicles, showed that both AuNPs acquired lipids after retrieval. However, the lipid-acquired MTAB-AuNPs did not aggregate after retrieval, but PAH-AuNPs did, suggesting that the different surface chemistries of the AuNPs lead to different structural transformations (*e.g.* lipid-corona structures and nanoparticle aggregation) [37]. Here, we, therefore, implement coarse-grained MARTINI and dissipative particle dynamics (DPD) simulations to explain lipid corona formation and transformations of lipid-acquired AuNPs at the molecular level.

8.2 Lipid Self-Assembly on Polycation-Coated Gold Nanoparticles

The all-atom 200-mer polycation, PAH_{200}-coated AuNP structure determined in Chapter 5 was used to benchmark a polarizable MARTINI (POL-MARTINI) model for PAH-AuNPs developed by our collaborators [26]. The POL-MARTINI simulations of lipids randomly distributed throughout the simulation box with the PAH-AuNP fixed at the center revealed that lipids self-assemble to form membrane patches on PAH-AuNPs.

We take the DPD coarse-grained PAH-AuNP and lipid models developed in Chapter 7 to simulate directly the transformations at the interface between of PAH-AuNPs and a lipid membrane. The exposed, polymeric backbone allows PAH-AuNPs to embed into the hydrophobic layer of the membrane (Figure 46). Lipids are associated with the bilayered structure intact, consistent with the lipid self-assembly simulations. Similar

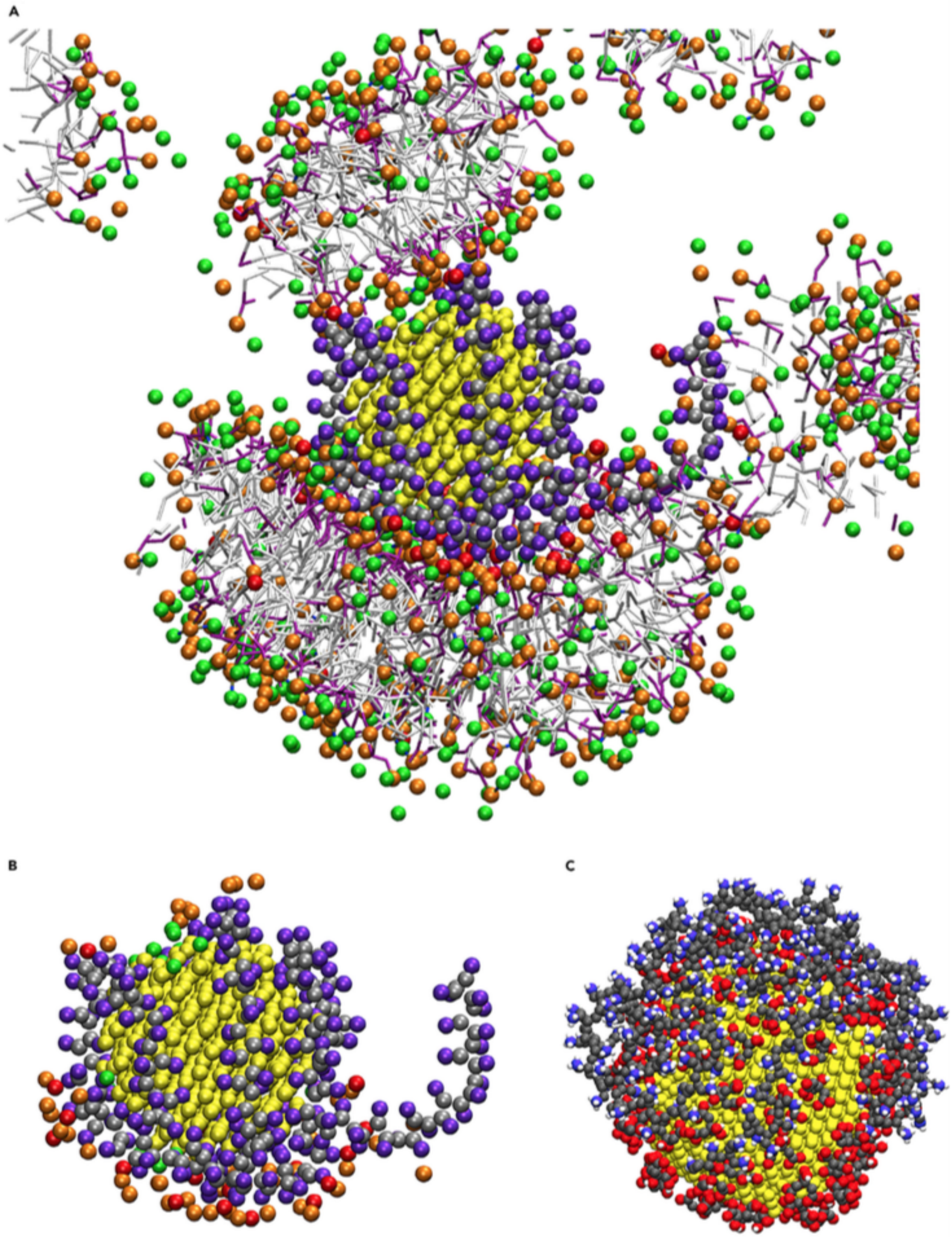

Figure 45: (A) The final snapshot after 400 ns of simulations using the POL-MARTINI coarse-grained model for lipid self-assembly on a AuNP wrapped in a single PAH polymer of 160 monomers. Lipid tails are shown as white and purple lines. (B) A zoomed-in view of just the phosphate (orange), PG head group glycerol (red), and choline (green) groups within 6 Å of the cationic side chain of PAH (purple and gray) or Au (yellow). (C) Final snapshot after 52.5 ns of an all-atom simulation of PAH deposition on a citrate-AuNP. Water and counterions are removed for clarity.

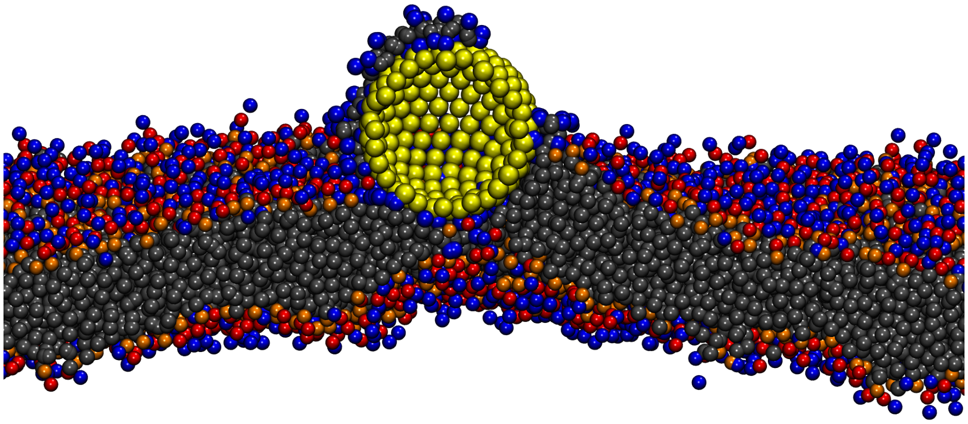

Figure 46: Cross section of PAH_{200}-AuNP embedded in membrane.

embedding of PAH-AuNPs into bacterial membranes has been captured in transmission electron micrographs of PAH-AuNPs [11]. Thus, we demonstrate that terminal cationic groups in the polycation PAH promote electrostatic attraction with anionic phosphate groups in lipid bilayers. Additionally, the exposed hydrophobic groups of the polymeric backbone are critical in associating with lipid-bilayer systems and driving lipid-corona formation.

8.3 Defects in Self-Assembled Monolayers on Nanoparticles Prompt Phospholipid Extraction and Bilayer Curvature-Dependent Transformations

8.3.1 Introduction

As mentioned in Chapter 4, nanoparticles (NPs) are typically functionalized with ligands to obtain colloidal stability and uniform dispersion in aqueous suspensions or thin films [212]. The self-assembly of alkanethiol monolayers on NP surfaces is a common means of functionalization [93]. Both experiment and simulation have helped identify certain ligand structures and properties that trigger events initiated at the interface between AuNPs and lipid bilayers such as AuNP binding, AuNP translocation, and cell lysis. All-atom molecular dynamics (MD) simulations [132, 133] have shown that cationic alkanethiol-coated AuNPs interact more strongly with planar membranes than anionic alkanethiol-coated AuNPs because the cationic ligands can penetrate deeper into the membrane surface where the lipid-head phosphate groups are located. At larger biologically relevant scales, experiments observing reduced bacterial colony count and cell lysis have demonstrated that cationic AuNPs are generally more toxic potentially due to stronger association of cationic AuNPs with lipid bilayers [11, 8]. Interestingly, MD simulations of lipid bicelles [130] and MARTINI coarse-grained simulations of membranes [134] with 2 nm (in diameter) AuNPs protected by mixed ligand layers of anionic alkanethiols and uncharged methyl-terminated alkanethiols have shown that anionic AuNPs can also insert into these zwitterionic lipid-bilayer systems. These results suggest that association of NP ligands with lipid bilayers is independent of the ligand charge provided that parts of the hydrophobic alkyl chains in both the ligands and the lipids are solvent-exposed and in proximity to interact.

In essence, the morphology of the self-assembled monolayer (SAM) of ligands on NPs drives the interaction of NPs with amphiphilic biomolecules. Simulations of the nano-bio interface have largely focused on defect-free SAMs on NPs for functionalized NP models. That is, the force-field parameters for NP ligands have been tuned [185, 186], or mixtures of charged and uncharged ligands, each with different lengths, have been used [130, 131, 134, 213] to generate SAMs with uniform spatial distribution of ligands on NPs. The even distribution of hydrophilic and hydrophobic coarse-grained beads on a spherical NP surface also represents defect-free SAMs on NPs [172, 174, 187]. In a recent study highlighted in Chapter 4, we used a combination of solution nuclear magnetic resonance (NMR) spectroscopy and MD simulations to determine the SAM structure of the alkanethiol (11-mercaptoundecyl)trimethylammonium bromide (MUTAB) and of the 16-carbon variant (MTAB) and the nature of defects in SAMs when varying ligand density and AuNP size with correlation to corresponding changes in NMR chemical shifts of the terminal quaternary ammonium headgroup protons [23]. Long-chain alkanethiols assemble into ligand islands particularly on smaller NP core sizes less than 8 nm with greater NP surface curvature due to the competition between hydrophobic ligand chain packing and free volume available in space per ligand, leaving large defects or voids between ligand islands (Figure 47A). This ligand-island morphology on AuNPs has previously been revealed *via* MD simulations by other groups [110, 111, 114] and is predicted to form among ligands with alkyl chain length of more than four –CH2 groups [110]. This ligand-island morphology has also been observed both experimentally and computationally in NPs of other metal cores: CdSe [120], PbS [214], and silver [215].

Here, we used and dissipative particle dynamics (DPD) simulations with the corresponding bottom-up coarse-grained NP models to reveal a mechanism for NP insertion, lipid extraction, and bilayer thinning driven by large defects in SAMs on smaller NPs (Figure 47). Lipid extraction from zwitterionic vesicles by 14 nm MTAB-coated AuNPs has been observed experimentally [37], suggesting that even larger NPs with nearly saturated and uniformly distributed terminal headgroup ligand layers alongside smaller defects [23] strongly incorporate with lipid bilayers at long experimental time-scales. The persistence of defects in alkanethiol monolayers on NPs and planar metal films is also inevitable due to small molecule adsorbates and surface impurities, facets and unevenness of the metal surface itself, and the assembly of ligands on such surfaces [25, 93, 160]. To our knowledge, reports on the influence of

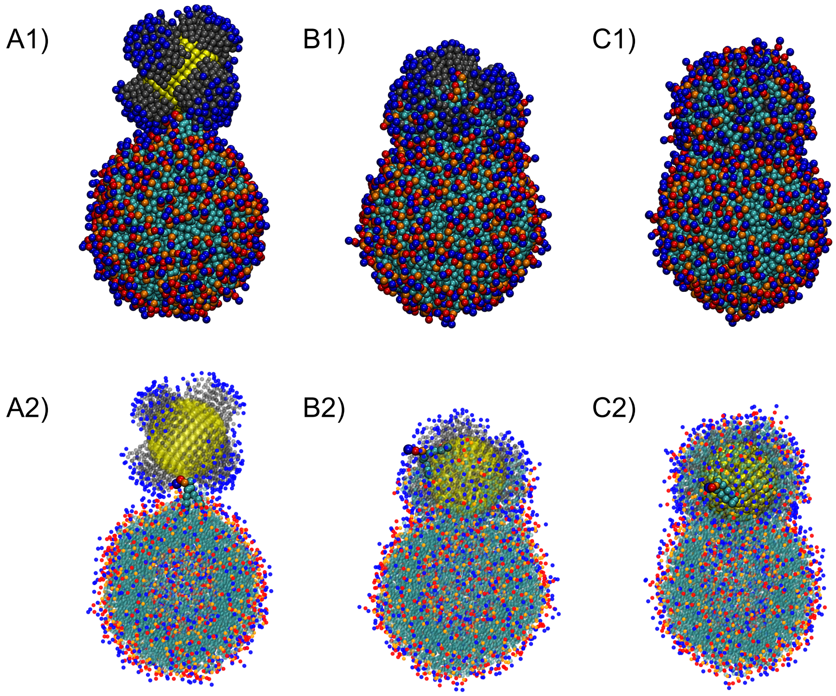

Figure 47: Mechanism for nanoparticle (NP) insertion and lipid extraction onset by a protruding lipid (shown in solid beads in row 2): A) Lipid-tail protrusion, which we set as $t = 0$ for our results, enables interaction with exposed hydrophobic chains on the edges of ligand islands; B) A ligand island inserts into the vesicle, and surrounding defects become sites for lipid extraction, shown after 20,000 timesteps; C) The nanoparticle has inserted, and the ligand layer is saturated with lipids, shown after 200,000 timesteps. In row 1, all coarse-grained beads are shown to scale with gold beads in yellow, hydrophobic beads of the NP ligands in gray, hydrophobic beads of the lipids in cyan, lipid glycerol groups in orange, lipid phosphate groups in red, and quaternary ammonium groups of both the lipids and NP ligands in blue. In row 2, all beads, except for the initial protruding lipid, are made transparent with smaller bead size, and water beads are removed for clarity.

SAM defects on the acquisition of biomolecular coronas by NPs are limited because defect formation is inherently difficult to isolate and control through experiments. MD simulations have enabled modeling of designed defects in SAMs on planar films to show how adsorption into defects can significantly alter the native conformation of proteins [216]. Our results here demonstrate that even commonly synthesized NPs can undergo significant defect-triggered transformations, particularly lipid extraction and corona formation on NPs, at the NP-bilayer interface with biological consequences.

8.3.2 Materials and Methods

Coarse-grained models of 4 nm AuNPs functionalized with the cationic ligand MUTAB- or its anionic analogue 11-mercaptoundecanoic acid (MUA) and DMPC-lipid vesicles, as discussed in Chapter 7, were simulated together to understand vesicle size and curvature effects on transformations at the nano-bio interface.

For each simulation, the gold core of the NP moves as a rigid body with its center of mass initially attached to a spring at the center of the simulation box, allowing it to move up to 2 nm (the NP radius) from this position. The vesicle is free to move in the simulation box. Box sizes are chosen such that half of a box length is the sum of the radius of the NP, the diameter of the vesicle and a 13 Å water cushion. Thereby, the NP does not interact with the periodic image of the vesicle. Counterions are included so that the salt concentration of the box is 0.1 M. The system size is shown in Table A8.1 in the Appendix.

We observed that lipid-tail protrusion is the first step in the insertion of NPs into bilayers (Figure 47A), as previously identified with 2 nm AuNPs on curved edges of bicelles [130] and on planar membranes [134]. At the first onset of lipid-tail protrusion, simulations are restarted with constraints on the NP removed. We ran a series of simulations of up to 10,000,000 timesteps and obtained five trajectories each of MUTAB- and MUA-NPs with a 12 nm vesicle and three trajectories of MUTAB-NP with a 25 nm vesicle, in which a protruding lipid tail comes in contact with a NP ligand chain.

Packmol [115] was used to generate the initial configurations for each simulation. All simulations were run using LAMMPS [116] at a timestep of 0.02τ, with a timestep on the order of 100 ps [174, 187, 217], at constant NVE. The DPD thermostat was set to the reduced temperature $T^* = 1$. Short- and long-ranged electrostatic interactions are calculated through the particle-particle particle-mesh (PPPM) method, and the short-ranged interactions are obtained explicitly with the electrostatic force within the cutoff distance, r_c in reduced units, as described in Chapter 7.

8.3.3 Results and Discussion

We find that SAM defects on NPs not only prompt NP insertion into bilayers, but also become sites for lipid extraction from bilayers (Figs. 47B, A8.4, A8.5, A8.6). At the end of each trajectory, we identified a ligand that had inserted into the vesicle and tracked its distance from the center of mass (COM) of the vesicle (vesicle COM) over time, starting from the initial lipid-tail protrusion event set as $t = 0$ (Figure 48A). The ligand is initially oriented ∼63-84 Å away from the vesicle COM, or ∼3-24 Å from the 12 nm vesicle surface, exposing the hydrophobic chains on the edges of its associated ligand island toward the vesicle. The converged distance between the tagged ligand and vesicle COM fluctuates around an average of 24.9 Å. The NP appears to remain inserted and extracts lipids *via* the shuttling of lipids near the site of ligand-island insertion to SAM defects around the ligand island; it does not acquire lipids by the detaching and tumbling of NPs along the vesicle. At the coarse-grained level of these simulations, a timestep cannot be rigorously mapped to real time units [22]. An effective coarse-grained time can be obtained by matching the lateral diffusion coefficient of lipids in DPD simulations with experimental values. The resulting estimate of the DPD timestep is on the order of 100 ps [174, 187, 217]. The time to NP insertion is 25,000-75,000 timesteps, or on the order of 2.5-7.5 μs (Figure 48A) and to the saturation of SAM defects with ∼92 lipids extracted from the vesicles is 100,000 timesteps, or on the order of 10 μs (Figure 48B). The fluctuations around the average number of lipids extracted suggest that lipids can still move between the membrane and the SAM, once the NP has inserted. The corresponding results with the 25 nm vesicle are in the Appendix (Figure A8.3), showing a similar time to NP insertion and coordination number of ∼93 lipids due to the fixed ligand density on NPs.

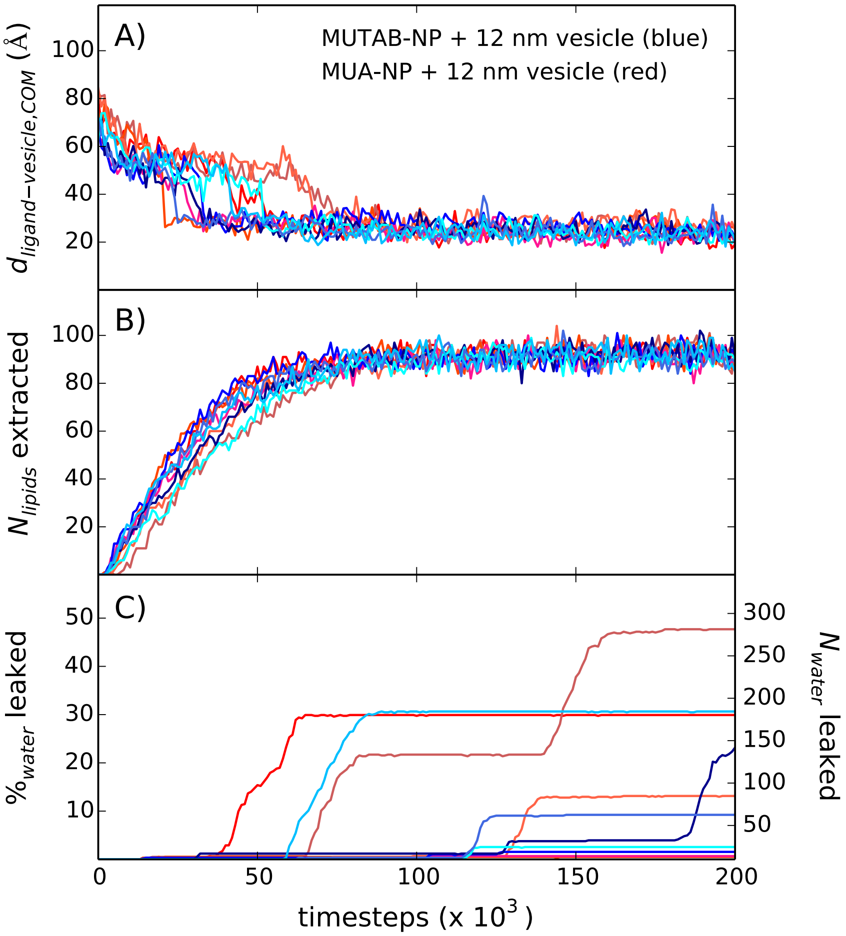

Figure 48: A) Distance between NP ligand and vesicle COM, $d_{ligand-vesicle,COM}$ *vs.* time. B) Number of lipids extracted *vs.* time. C) Percent of water and number of water beads leaked from vesicles *vs.* time. Note that each trajectory started with 585 water molecules inside the vesicle core. In each panel, the results from five trajectories with cationic MUTAB-NPs and 12 nm vesicles are shown in blue and from five trajectories with anionic MUA-NPs and 12 nm vesicles in red. The lipid-tail protrusion event is set as 0 timesteps.

The number of lipids extracted and the percent of water leaked from vesicles were determined by first computing the radial distribution functions, *g(r)*'s, between the NP COM and lipid glycerol beads and between the vesicle COM and glycerol beads, respectively (Figs. A8.1 and A8.2). We used the distance at the half-maximum after the respective peak in the *g(r)*'s as cutoffs to count the gain in lipids within the cutoff around the NP COM, excluding the portion of the NP inserted in the vesicle, and loss of water within the cutoff around the vesicle COM. We observe no consistency in the percent of water leaked upon NP insertion and attribute high leakage ($> 10\%$) to deformations in 12 nm vesicles due to the metastability and high bending moduli of smaller vesicles with greater curvature [209, 210, 218, 219]. Leakage of 0-60 water beads is more consistent with results from simulations using the larger 25 nm vesicles (Figs. 48C and A8.3). Even in the dilute limit of a single NP and vesicle, we found that NP association can lead to water leakage in agreement with experiments involving fluorophore release from vesicles [8, 220].

We also find that ligand-island insertion, lipid extraction, and ligand length collectively cause bilayer curvature-dependent transformations. We calculated the absolute value of the difference in the radial coordinates relative to the vesicle COM of the glycerol bead and final tail bead, and took the average value between the two tails per lipid to determine the lipid tail end-to-end distance, r_{ee}, for each lipid in the vesicle. The distribution of r_{ee}, in essence, captures the local packing and tilting of lipids throughout the vesicle in response to NP exposure (Figure 49). Vesicles in the size range of ∼10 nm are generally metastable and readily fuse with other vesicles to make larger ones [218, 219]. Moreover due to the high bending resistance of highly curved vesicles [209, 210], we find that the 12 nm vesicle buckles and the bilayer becomes more

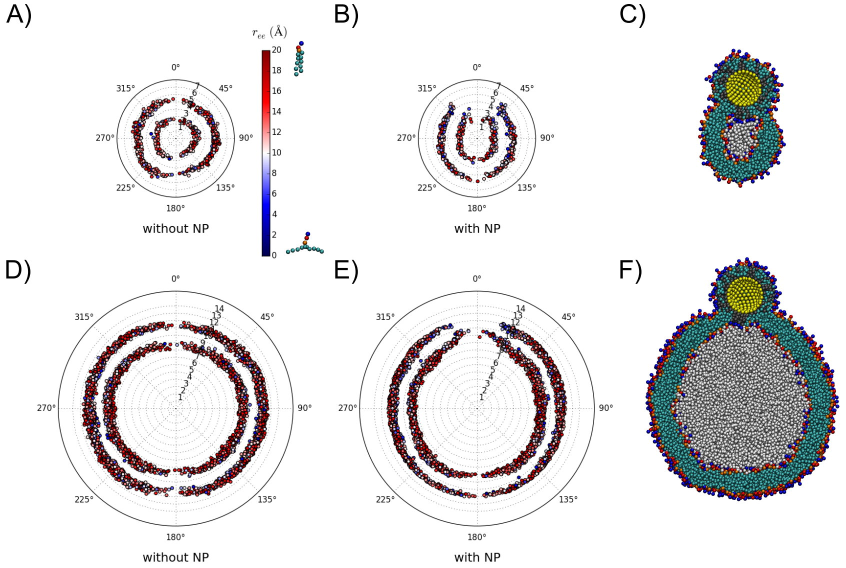

Figure 49: Distribution of lipid glycerol groups and the average lipid tail end-to-end distance, r_{ee}, for each lipid for 12 nm (in panels A and B) and 25 nm (in panels D and E) vesicles without the presence of MUTAB-NP and in the presence of MUTAB-NP 200,000 timesteps after the lipid-tail protrusion event upon NP exposure. The trajectory snapshots in panels C and F show the corresponding cross sections of the NP inserted in the vesicles. The color of a given point in panels A-B and D-E indicates the r_{ee} as per the colorbar shown next to panel A. A high r_{ee} is indicative of lipid tails oriented perpendicular to the plane of a bilayer, and a small r_{ee} is indicative of lipid tails oriented parallel to the plane of a bilayer. Vesicles are oriented with the COM at 0 nm and the NP insertion site at the 0° pole. Lipid distribution is plotted in 1 nm radial ticks relative to the vesicle COM invariant of the equatorial angle, and therefore, there are fewer points sampled at the poles compared to the equator.

planar (Figs. 49A,B, A8.7, and A8.8). Figure 49C,F illustrates the reconfiguration of the lipid bilayer around the inserted ligand island and surrounding defects. The bilayer becomes thinner at the NP insertion site, as quantified by an increase in blue markers signifying smaller r_{ee} and a shift in the distribution of lipids in the inner layer from 3 to 4 nm away from the 12 nm vesicle COM and from 9 to 11 nm away from the 25 nm vesicle COM (Figs. 49, A8.7, A8.8, and A8.9). This thinning is common to both the 12 nm and the larger 25 nm vesicle though the latter is subject to less deformation due to the fact that it is necessarily less curved *a priori*. In both cases, the bilayer thins such that hydrophobic contact between the lipid bilayer (ten hydrophobic beads across) and ligand chains (four hydrophobic beads) is maximized and that the hydrophilic terminal groups of the ligands penetrate to the water inside the vesicle. Longer time-scale results after 1,000,000 timesteps are presented in the Appendix (Figs. A8.7, A8.8, and A8.9), showing that these are converged structural transformations.

8.4 Conclusion

We have demonstrated that commonly synthesized alkanethiol-coated NPs can extract lipids upon NP insertion into bilayers and lead to bilayer curvature-dependent deformations, such as bilayer buckling and planarization, which all need to be considered when characterizing NPs and bilayers at their interface. Although the ligand charge affects the probability of NP association with bilayers–cationic NPs are more likely to insert into defect-free supported bilayers [130, 132, 133]–deformations at the nano-bio interface are dependent on ligand structure, such as alkyl chain length. The ligand islands that form on the AuNPs surface at greater surface curvatures and with longer ligands insert into bilayers with the defects in the surrounding alkanethiol monolayer becoming sites of lipid extraction. Polycation-coated AuNPs interface differently with lipid-bilayer systems due to the greater spatial distribution of hydrophobic groups *via* the exposed polymeric backbones, which prompt embedding of the AuNP into bilayers. We have thereby determined the molecular-level basis for the different lipid coronas acquired by AuNPs from their initial surface chemistry.

Chapter 9

Conclusions and Outlook

9.1 Concluding Remarks

Through bottom-up simulation approaches, we have shown that typical synthesized or engineered nanoparticles (NPs) have non-uniform surfaces. These NPs can undergo significant transformations at the nano-bio interface due to heterogeneous spatial charge and hydrophobic group distributions, such as in polyelectrolyte wrappings and in defects within self-assembled alkanethiol monolayers. We suggest that this precise distribution on NPs dictates their transformations and biological impact.

9.2 Nanoparticle Design Rules

Controlling NP transformations in complex biological environments and, thereby, minimizing biological impact require understanding of and synthetic control over the structure and reactivity of the NP surface. We have learned that for alkanethiol-coated ligands, the self-assembled monolayer (SAM) structure of alkanethiols on AuNPs can be tuned by varying ligand structure and AuNP size [23]. By a combination of using ligands with bulky terminal charged groups, decreasing alkyl chain length, and increasing AuNP size, the headgroup layer in SAMs can be saturated, resulting in uniform ligand and spatial charge distribution on AuNPs. This prevents lipid corona formation, as there would be no hydrophobic groups exposed in the SAMs to extract lipids or penetrate lipid bilayers through interactions with phospholipid tails.

However, defect-free design of SAMs on AuNPs does not prevent the formation of protein coronas. The acquisition of extracellular protein coronas by NPs is largely driven by electrostatic attraction between the NP surface charge and oppositely charged solvent-accessible amino acid residues on proteins [17]. Work by us and other groups have shown understanding of and increasing control over the orientation of proteins on AuNPs and the desorption of proteins [17, 32, 221]. The challenge still remains to minimize protein agglomeration on charged ligand-coated NPs and deformation in protein structure upon the adsorption of proteins onto NPs.

The layer-by-layer design of polyectrolyte-coated AuNPs enables promising applications in sensing [126], imaging [127], and drug-delivery [128, 129]. However, commercially available polyectrolytes, such as poly(allylamine hydrochloride), are variably long and non-uniformly layer on the AuNP surface [24]. Again, the charged surface of polyelectrolyte-coated AuNPs prompts protein corona formation, and the exposed polymeric backbone enables penetration into lipid membranes. Greater fundamental understanding of this class of engineered AuNPs is required through a bottom-up approach. Design rules can be developed for multilayered NPs by controlling polyelectrolyte length and monomer structure, their influence on overall polyelectrolyte structure and polyelectrolyte layering on NPs per polyelectrolyte per layer to improve the feasibility and sustainability of their applications.

9.3 Future Work

Coarse-grained simulations will be a valuable tool in testing design rules and revealing mechanisms of long time-scale transformations for engineered NPs at biological interfaces. This thesis highlights work on the dilute limit of nano-bio interactions with a single NP and single protein or simple lipid-bilayer system. Moreover, the transformations studied have focused on structural changes at the smallest nanometer scale, whether on the NP or at the local site of NP insertion into lipid bilayers.

Through simulations with lipid membranes, we can also characterize the membrane dynamics in response to nanoparticle exposure and attachment. All-atom molecular dynamics simulations have previously revealed the correlated motion of lipids and their nearest neighbors that persists for tens of nanometers as lipids diffuse laterally across a membrane [222]. Single-molecule fluorescence microscopy [26] and atomic force microscopy [223] experiments have shown that polycation-coated NPs can disrupt ordered lipid domains and increase membrane fluidity. Furthermore, through coarse-grained dissipative particle dynamics simulations of NP-membrane interactions, we can go beyond measurements of local structural changes at a NP attachment site and observe persistent dynamical changes across membranes, which can alter the partitioning and mobility of lipid domains and the structure and function of transmembrane proteins [222].

Future directions include calculating dynamical changes at the nano-bio interface that persist at long time-scales and span length-scales across a lipid membrane, modeling nanoparticle suspensions to understand nanoparticle cooperativity effects in inducing transformations at the nano-bio interface, and further, tackling the complexity of these systems.

Appendix

A3. Preferential Binding of a Peripheral Membrane Protein to a Uniformly Anionic Gold Nanoparticle

Simulation of Cyt *c* in Solvent

In order to benchmark the behavior of cyt *c* in the simulations when not in the presence of the AuNP, a numerical control experimental was run. Namely, we prepared an equilibrated configuration with cyt *c*, but no NP present, and solvated it with TIP3P waters using the same procedures as for the cyt *c* with MPA-AuNP systems. A 200 nanosecond trajectory was then integrated using the same protocol as that for the MPA-AuNP systems. Figure A3.1 displays the radius of gyration of the cyt *c* over this long trajectory. The specific values at any given time are particular to the trajectory. However, the average value and degree of fluctuations are statistically relevant. As noted in Chapter 3, the average value is consistent with the experimentally reported value of 13.6 Å [76].

Relative Orientation of Cyt *c* in Close Proximity to MPA-AuNPs

Figure A3.2 provides the distance between the selected sites of cyt *c* and MPA-AuNP in three trajectories starting from configurations with the three initial faces toward the nanoparticle not shown in Chapter 3. In each of these three cases, cyt *c* begins with a particular binding site–either site N, A, or L for trajectories 1, 2 or 5, respectively. In the case of trajectories 2 and 5, cyt *c* remains in that relative orientation for the entirety of the 200 nanosecond trajectories, as also shown in Figures A3.3 and A3.4, respectively. In the case of trajectory 1, cyt *c* appears to not be relaxed at the end of the trajectory and moving toward an orientation in which site N would not be facing the nanoparticle. Thus, these three trajectories merely indicate that the dynamic orientations with site A and L facing the MPA-AuNP are metastable up to, at least, timescales on the order of 200 nanoseconds.

Cytochrome c Secondary and Tertiary Structure Conformations

Figure A3.5 provides the radius of gyration for trajectories 1, 2, and 5, complementing the data provided for trajectories 3, 4, and 6 in Figure 9 of Chapter 3.

The RMSD's of the trajectories for cyt *c* and the heme group relative to their initial structures are shown here in Figure A3.6. As summarized in Chapter 3, they provide little new insight in the dynamics of the proteins in so far as they agree fully with the interpretation gained from analysis of the radius of gyration.

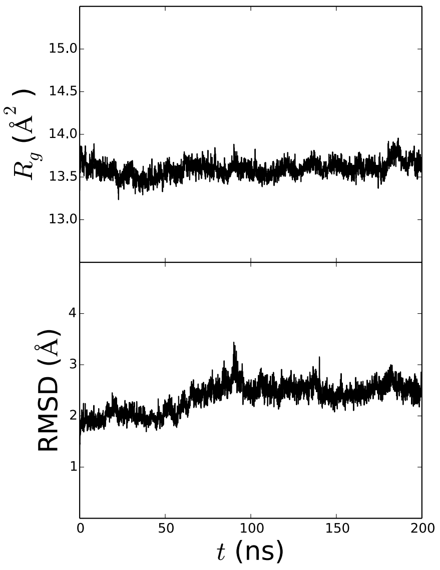

Figure A3.1: The radius of gyration (R_g) and root mean square deviation (RMSD) as a function of time for cyt *c* in a periodic box of TIP3P water for 200 ns. The RMSD of cyt *c* is aligned to the final frame at the end of the 200 ns trajectory.

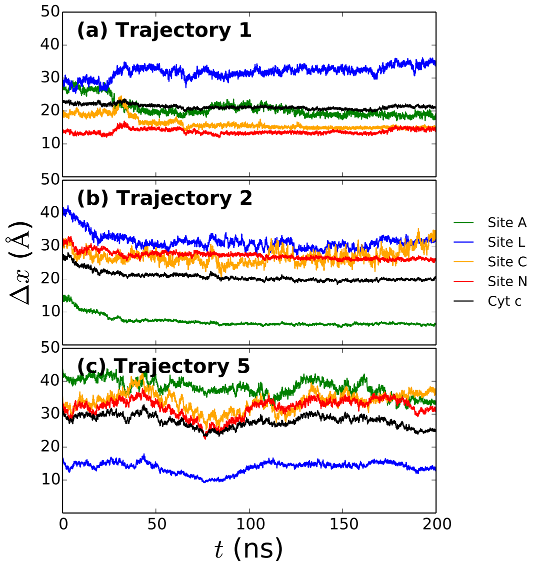

Figure A3.2: The distance Δx between the COM positions of the cyt *c* binding sites and the MPA-AuNP surface were monitored for trajectories 1, 2, and 5. The green, blue, orange, red, and black curves are the measured distances between the bare AuNP surface and the COM of site A, site L, site C, and site N or the cyt *c* COM, respectively.

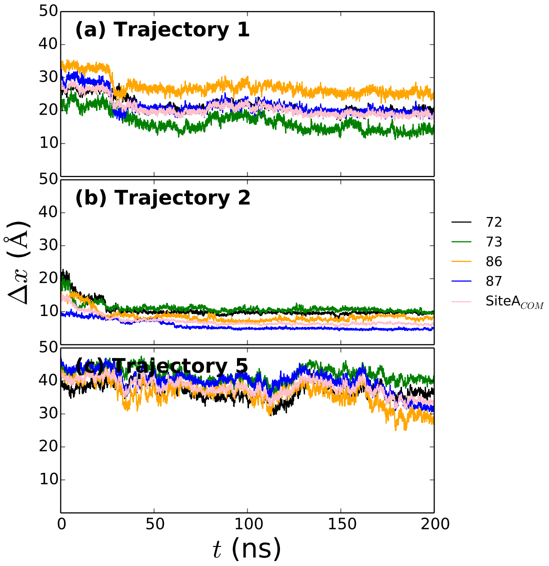

Figure A3.3: The distance Δx between the specific groups of amino acids–residues K72, K73, K86, and K87, and the COM of site A–in the anionic phospholipid binding site A of cyt c and the surface of the MPA-AuNP for trajectories 1, 2, and 5.

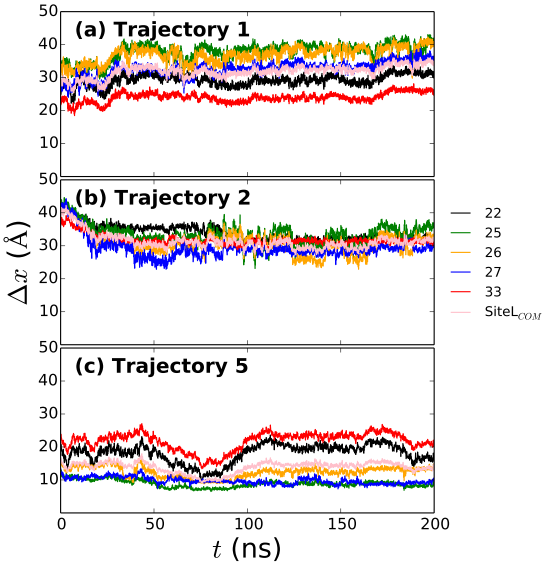

Figure A3.4: The distance Δx between the specific groups of amino acids–residues K22, K25, K26, K27 and K33, and the COM of site L–in the anionic phospholipid binding site L of cyt c and the surface of the MPA-AuNP for trajectories 1, 2, and 5.

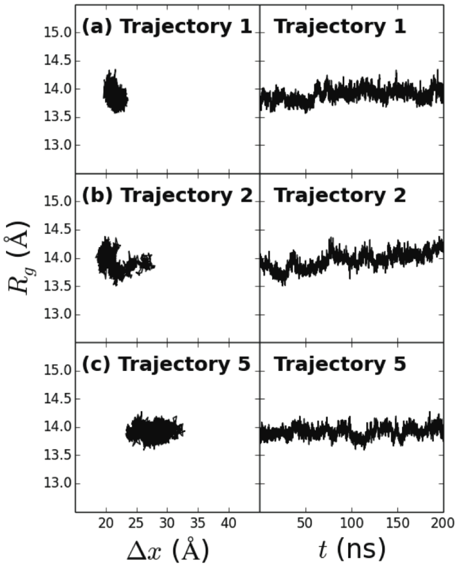

Figure A3.5: The radius of gyration R_g of cyt *c* *vs.* time along each 200 ns MD trajectory (right panels) as a function of the distance Δx between the cyt *c* COM and the surface of the MPA-AuNP (left panels).

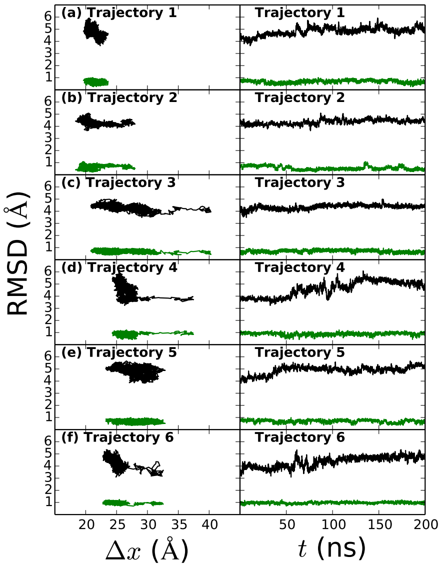

Figure A3.6: The RMSD of cyt *c* (black) and its heme group (green) *vs.* time along each 200 ns MD trajectory (right panels) is also shown as a function of the distance Δx between the cyt *c* COM and the surface of the MPA-AuNP (left panels). In all cases, the RMSD of cyt *c* is aligned to the equilibrated structure from MD simulations of cyt *c* in a box of TIP3P for 200 ns.

A4. The Effect of Surface Curvature and Ligand Structure on Ligand Environment in Self-Assembled Monolayers on Gold Nanoparticles

The convergence of the simulations was verified by monitoring the tilt angle of each of the MUTAB ligands as a function of time over the preparation through production stages: (1) The tilt angle for each MUTAB ligand is the angle between the vector normal to the nanosphere at the position of the sulfur atom and the vector connecting the nitrogen atom in the MUTAB headgroup to sulfur. We calculated the average tilt angle of ligands throughout five trajectories to track equilibration of MUTAB self-assembled on 4 nm AuNSs at 4.0 ligands/nm^2 density. The average tilt angle of 12° for the initial starting configurations with all ligands oriented nearly normal to the AuNS surface is shown at time, $t = 0$ ns, for reference (Figure A4.1). The next immediate point is of the average tilt angle from the starting configurations of simulations at 300 K, once the ligands are bound to the AuNS surface. Simulations at 400 K were then run to enhance the sampling of ligand-chain conformations, and convergence in the average tilt angle is observed during the subsequent 10 ns equilibration run at 300 K. For the other conditions at lower surface curvatures and greater ligand densities, the simulation times are more than sufficient for equilibration. The radial distribution functions, *g(r)*'s for individual equilibrated trajectories used to compute the averages (Figs. 19 and 20 in Chapter 4) are shown in Figs. A4.2 and A4.3.

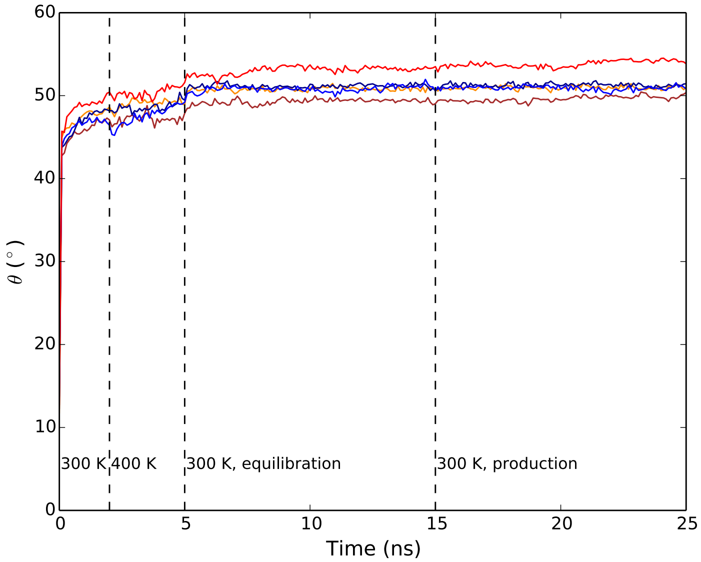

Figure A4.1: Average tilt angle θ of MUTAB ligands *vs.* time for five trajectories of MUTAB ligands self-assembled on 4 nm AuNSs at 4.0 ligands/nm^2 density, which include an initial 2 ns equilibration at 300 K, a 3 ns simulation at 400 K, 10 ns equilibration at 300 K, and 10 ns production run at 300 K.

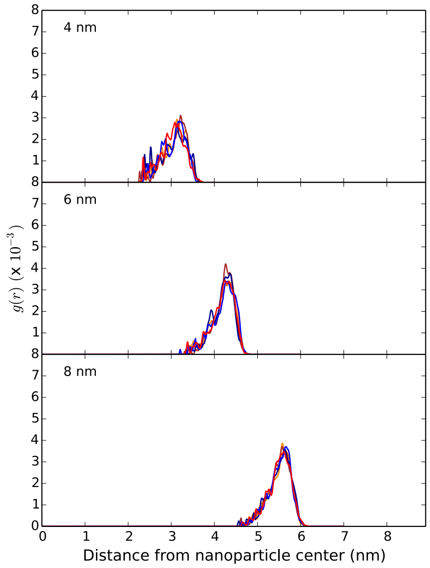

Figure A4.2: Radial distribution function, *g(r)*, between the nanoparticle center of mass for 4-, 6-, and 8-nm AuNSs and the nitrogen atoms of MUTAB at a ligand density of 4.0 molecules nm^{-2}. Trajectories are distinguished by color.

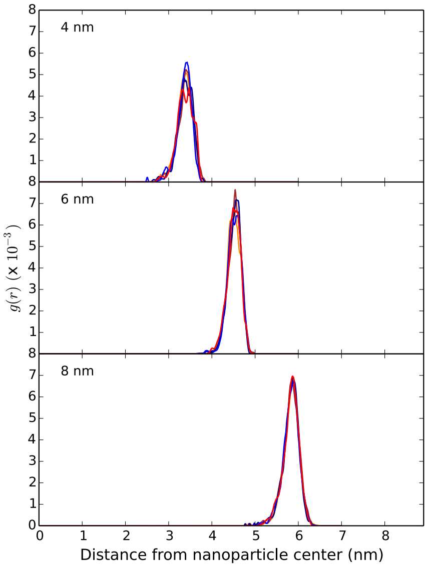

Figure A4.3: Radial distribution function, *g(r)*, between the nanoparticle center of mass for 4-, 6-, and 8-nm AuNSs and the nitrogen atoms of MUTAB at a ligand density of 6.0 molecules nm^{-2}. Trajectories are distinguished by color.

A5. Adsorption Dynamics and Structure of Polycations on Citrate-Coated Gold Nanoparticles

In Table A5.1, we provide the force-field parameters used in our simulations. Simulation parameters and other settings are provided in Table A5.2. Supporting figures include the initial configurations in Figure A5.1, snapshots of loop, tail, and train structural motifs observed in our simulations in Figure A5.2, and the radial distribution functions for each trajectory in Figs. A5.3 and A5.4. Structural characterization of polycations adsorbed onto gold nanoparticles for additional trajectories d-e (Figure A5.1) in implicit solvent not shown in Chapter 5 are provided in Figs. A5.5 and A5.6.

Nonbonded Interactions (LJ and Coulomb)			
PAH (atom or group)	q (e^{-})	σ (Å)	ε (kcal mol^{-1})
CH$_3$	0.0	3.79	0.18
CH$_2$	0.0	3.95	0.14
CH	0.0	4.23	0.13
CH$_{2,amm}$ (C-NH$_3^+$)	0.31	3.95	0.14
N	-0.30	3.25	0.17
H	0.33	0.0	0.0
citrate (atom or group)			
CH$_2$	0.0	3.905	0.118
C1 (COO$^-$)	0.60	3.75	0.105
O1 (COO$^-$)	–0.80	2.96	0.210
C2 (CR$_3$)	0.265	3.5	0.066
O2 (OH)	–0.683	3.12	0.170
H1 (OH)	0.418	0.0	0.0
Au	0.0	2.629	5.29^a, 1.55^b
Na	1.0	4.07	0.0005
Cl	–1.0	4.02	0.71

[a] For construction of gold-nanoparticle cores

[b] For simulations of citrate and PAH adsorption

Bond Stretch		
bond	r_{ij} (Å)	K_{ij} (kcal mol^{-1} Å^{-2})
PAH		
CH$_{2,3}$-CH, CH-CH$_{2,amm}$	1.53	268.0
CH$_{2,amm}$-N	1.448	382.0
N-H	1.00	434.0
citrate		
C1-O1	1.208	777.0
C1-CH$_2$	1.492	302.0
C2-CH$_2$	1.529	268.0
C2-O2	1.41	320.0
O2-H1	0.945	553.0

Angle Bend		
angle	θ_{ijk} (deg)	K_{ijk} (kcal mol^{-1} rad^{-2})
PAH		
CH$_{2,3}$-CH$_2$-CH$_{2,amm}$	112.7	58.35
CH$_{2,amm}$-N-H, H-N-H	109.5	35.0
citrate		
O1-C1-O1	120.0	67.5
C1-CH$_2$-C2	107.8	32.4
CH$_2$-C2-CH$_2$	112.7	58.35
C1-C2-O2	109.5	50.0
C2-O2-H1	108.5	55.0

Torsion			
dihedral	V_1 (kcal mol^{-1})	V_2 (kcal mol^{-1})	V_3 (kcal mol^{-1})
PAH			
C-C-C-C	3.48	0.314	0.558
C-C-C-N	5.464	-0.458	0.97
C-C-N-H	0.0	0.0	0.694
citrate			
O1-C1-CH$_2$-C2	0.0	0.820	0.0
C1-CH$_2$-C2-CH$_2$	–3.185	–0.825	0.493
C1-CH$_2$-C2-O2	1.711	–0.5	0.663
(C1, CH$_2$)-C2-O2-H1	–0.356	0.174	0.492
O1-C1-CH$_2$-O2	9.066	0.0	0.0

Table A5.1: Force-field parameters for PAH, citrate, gold, and counterions.

system	number of atoms	box size (Å)	total simulation time (ns)
Citrate-AuNP + 1 PAH_{200}, implicit solvent	5253	135.0 × 135.0 × 285.0	34.5 - 54.0
Citrate-AuNP + 2 PAH_{200}, implicit solvent	6853	135.0 × 135.0 × 285.0	71.0 - 80.1
Citrate-AuNP + 1 PAH_{200}, explicit solvent	538653	135.0 × 135.0 × 285.0	120.0

Table A5.2: The characteristic parameters and settings used in the simulations for the model systems discussed in Chapter 5.

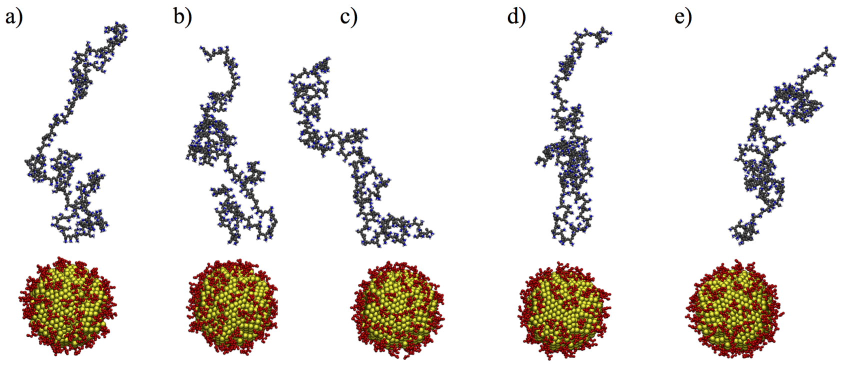

Figure A5.1: Initial configurations for PAH_{200} deposition on citrate-coated AuNPs in implicit solvent with citrate molecules shown in red, gold atoms in yellow, carbon atoms in gray, nitrogen atoms in blue, and hydrogen atoms in white. Counterions are removed for clarity. Configurations a-c were also used for corresponding simulations in explicit TIP3P solvent.

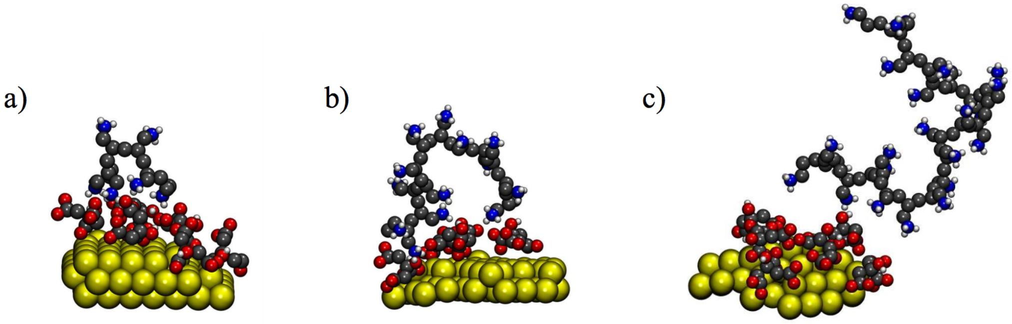

Figure A5.2: Trajectory snapshots of (a) 2-monomer, surface-bound trains that flank a 2-monomer solvent-exposed loop, resembling a kink; (b) a longer-length loop; and (c) a tail. Gold atoms are shown in yellow, carbon atoms in gray, oxygen atoms in red, hydrogen atoms in white, and nitrogen atoms in blue. Counterions and solvent molecules are removed for clarity.

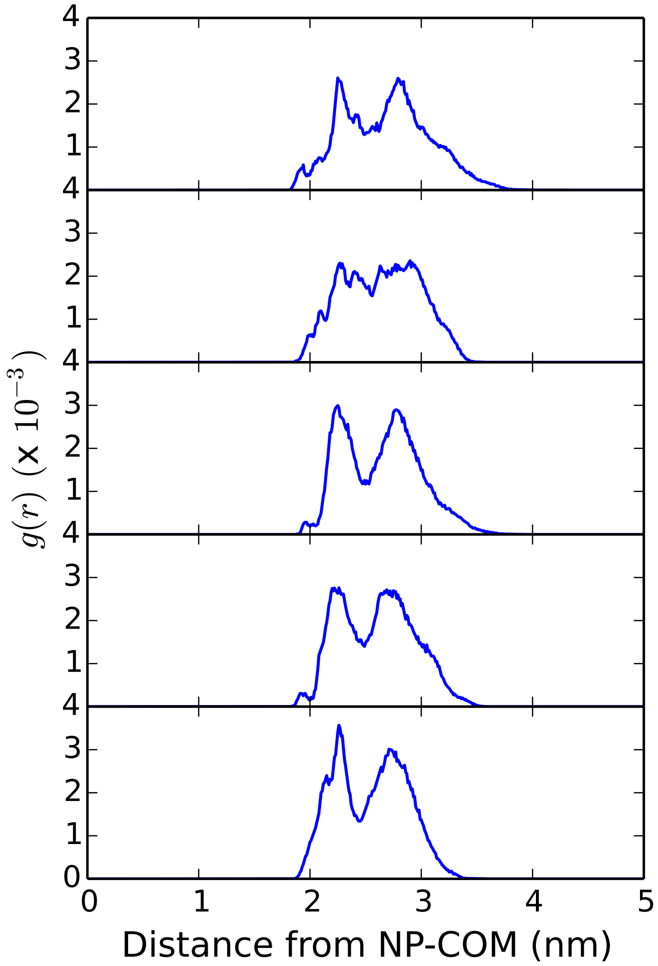

Figure A5.3: Radial distribution function, *g(r)*, between the nitrogen atoms of PAH_{200} deposited on a nanoparticle and the nanoparticle center of mass (NP-COM) for each trajectory in implicit solvent.

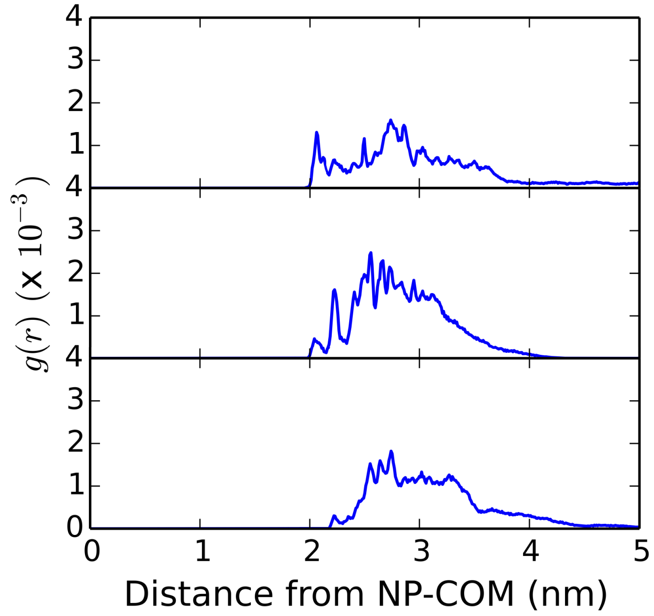

Figure A5.4: Radial distribution function, *g(r)*, between the nitrogen atoms of PAH_{200} deposited on a nanoparticle and the nanoparticle center of mass (NP-COM) for each trajectory in explicit TIP3P solvent.

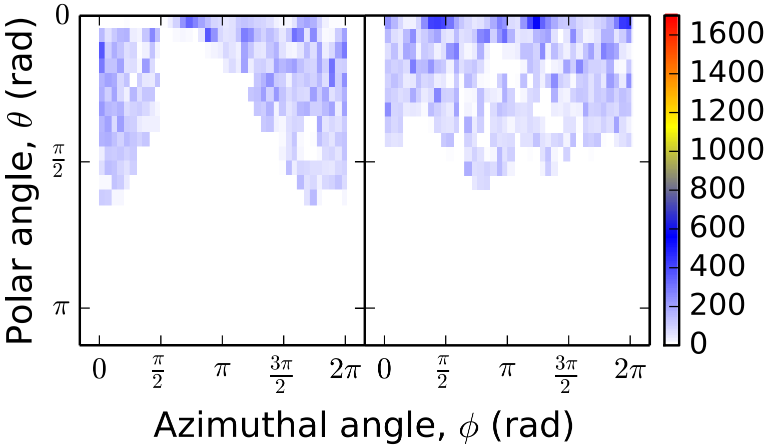

Figure A5.5: Surface coverage of nitrogen atoms of PAH_{200} from initial configurations d and e in implicit solvent. The azimuthal angle ranges from 0 to 2π radians along the equator of the nanoparticle. The polar angle ranges from 0 radians at the north pole to π radians at the south pole. The color scale shows the density of the nitrogen atoms.

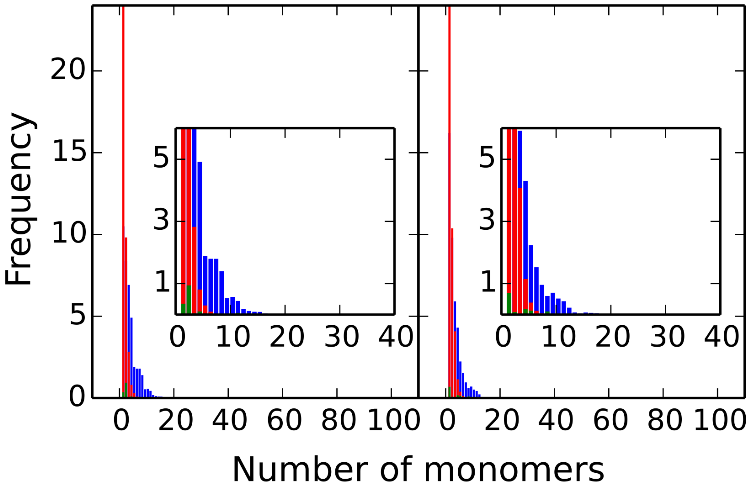

Figure A5.6: Histogram of the frequency of solvent-exposed loops, free tails, and surface-bound trains with n number of monomers within PAH$_{200}$ from initial configurations d and e in implicit solvent. The distributions are divided by the total number of frames sampled such that 1.0 indicates one instance in every frame.

A6. Density, Structure, and Stability of Citrate^{3-} and H_2citrate$^-$ on Bare and Coated Gold Nanoparticles

Simulation Parameters and Setup

To construct the 4, 6, and 8 nm AuNPs, we estimated the number of gold atoms required by dividing the volume of the approximately spherical nanoparticle by the volume of a gold atom with radius 1.44 Å. The gold atoms were randomly distributed at least 5.76 Å apart within a sphere with a radius that is 10 Å greater than the intended nanoparticle size, heated to 1400 K, and slowly cooled to and equilibrated at 300 K, using the parameters developed by Heinz and co-workers for a Lennard-Jones potential between metal atoms [112].

The chemical structures for H_2citrate$^-$ and a PAH monomer are provided in Figure A6.1. We used the OPLS-UA force field [144] for CH2 groups in the carbon backbone of citrate and PAH_{200} and the OPLS-AA force field [109] for all other atoms (Tables A6.1 and A6.2). Force-field parameters used to model PAH_{200} and methods on constructing PAH_{200} are specified in previous work [24] and in Section A5 of the Appendix (Table A5.1) . Either citrate^{3-} or H_2citrate$^-$ were randomly distributed throughout a simulation box along with Na^+ ions to neutralize and additional Na^+ and Cl^- counterions with the AuNP fixed at the center. The number of citrate and total system size for each simulation and additional details are described in Table A6.3.

For all simulations with citrate and PAH_{200}, the parameters for the Lennard-Jones potential between gold atoms were changed so that the gold-carbon parameters, following geometric mixing rules, matched those developed by Landman and co-workers [113, 114] for studies of alkane adsorption onto gold surfaces. Positions of gold atoms were kept fixed at the center of the simulation box. A drag force of 0.1 kcal/(mol Å) was applied to the oxygen atoms of the central carboxylate group of citrate toward the center of the AuNP using the LAMMPS [116] algorithm “fix drag” until these atoms fell within a specified cutoff distance from the AuNP surface as described in Chapter 6.

For simulations in explicit solvent, an unphysical, intramolecular hydrogen bond between a central-carboxylate oxygen and the hydroxyl hydrogen is known to form in simulations using standard force fields [145], unless this particular electrostatic interaction is significantly screened. We, instead, kept the central-carboxylate carbon, central carbon, and hydroxyl oxygen rigid with a fixed angle of 109.5° in all explicit-solvent simulations, which does not make a significant difference in the results presented. In order to keep the system size and computational cost low, we only added enough Na^+ ions to neutralize the citrate molecules, and box sizes were chosen so that the sodium-ion concentration was 0.4 M. The similarity of the H_2citrate$^-$ configurations across the varying solvent and salt conditions discussed in Chapter 6 suggests that these structural features on the nanoparticle surface are robust even to conditions far from the bulk. Additionally, the structure of citrate^{3-} layers constructed in 0.4 M Na^+ is also similar to the citrate^{3-} layers on AuNPs constructed in 0.15 M NaCl reported in the literature [176].

To understand the nature and stability of the citrate layer, we deposited PAH_{200} on cit-AuNPs equilibrated in explicit solvent. We used a PAH_{200} model that was previously constructed [24] and similarly followed the protocol to simulate PAH_{200} deposition onto cit-AuNPs. Specifically, PAH_{200} was initially aligned such that the end-to-end vector was tangent to the AuNP surface and positioned so that the closest atom in PAH was 10 Å away from the AuNP surface.

Packmol [115] was used to generate random initial configurations for the construction of the AuNPs, the adsorption of citrate anions onto AuNPs, and deposition of PAH_{200} on cit-AuNPs.

Molecular Dynamics Simulations of Cit-AuNPs and PAH-Cit-AuNPs

To measure the number of citrate anions adsorbed onto the AuNP surface in our simulations, we surveyed the number of citrate anions with an oxygen atom within various cutoff distances from surface gold atoms. We determined that an Au–O cutoff distance of 3.5 Å captures the citrate anions distinctly in the surface-bound monolayer on the AuNP surface (Figure A6.2).

Representative images of citrate^{3-} and H_2citrate^{-} maximally packed on 6- and 8-nm AuNPs in implicit solvent are shown in Figure A6.3. Representative snapshots from explicit-solvent simulations of PAH deposition on AuNPs coated with citrate^{3-} or H_2citrate^{-} are shown in Figs. A6.4 and A6.5, respectively. Figure A6.4 qualitatively shows the displacement and removal of citrate^{3-} anions from the AuNP surface upon PAH adsorption. Figure A6.5 qualitatively shows that the H_2citrate^{-} layer on AuNPs is highly stable in response to PAH adsorption. The changes in the surface density and spatial distribution of citrate anions on AuNPs are quantified in Chapter 6.

Using the Au–O cutoff distance of 3.5 Å, we quantified the number of surface-bound citrate and identified the specific oxygen-containing functional groups of these citrate–terminal carboxylate, central carboxylate, or central hydroxyl group–that are bound to the AuNP surface. Molecular configurations are defined according to which functional groups are surface-bound as described in Chapter 6. The 0-, 1-, and 2-arm configurations have at least one central group bound to the AuNP surface with 0, 1, and 2 terminal carboxylate groups surface-bound, respectively. Of these configurations, we examined what percent have the central carboxylate free and hydroxyl group bound, central carboxylate group bound and hydroxyl free, or both central groups bound to the AuNP surface (Figure A6.6). The analysis of molecular configurations of citrate^{3-} and H$_2$citrate^{-} from simulations is in agreement with ATR-FTIR experiments [42] on cit-AuNPs at highly basic pH and at pH below 9, respectively, as discussed in Chapter 6.

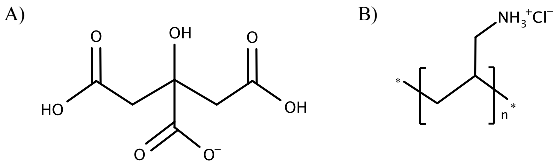

Figure A6.1: A) H_2citrate$^-$ with central carboxylate group and terminal carboxylic acid groups and B) PAH monomer.

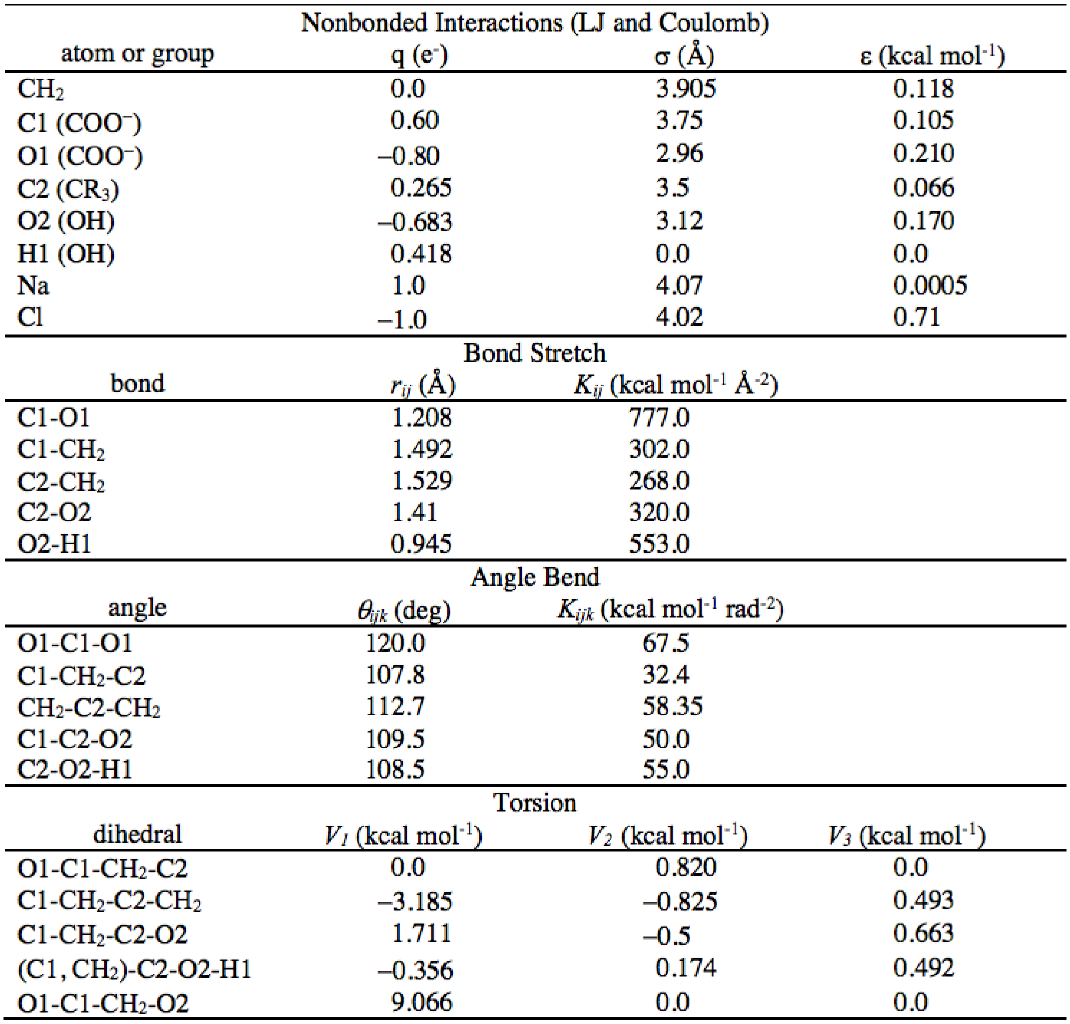

Nonbonded Interactions (LJ and Coulomb)			
atom or group	q (e^-)	σ (Å)	ε (kcal mol^{-1})
CH_2	0.0	3.905	0.118
C1 (COO^-)	0.60	3.75	0.105
O1 (COO^-)	–0.80	2.96	0.210
C2 (CR_3)	0.265	3.5	0.066
O2 (OH)	–0.683	3.12	0.170
H1 (OH)	0.418	0.0	0.0
Na	1.0	4.07	0.0005
Cl	–1.0	4.02	0.71
Bond Stretch			
bond	r_{ij} (Å)	K_{ij} (kcal mol^{-1} $Å^{-2}$)	
C1-O1	1.208	777.0	
C1-CH_2	1.492	302.0	
C2-CH_2	1.529	268.0	
C2-O2	1.41	320.0	
O2-H1	0.945	553.0	
Angle Bend			
angle	θ_{ijk} (deg)	K_{ijk} (kcal mol^{-1} rad^{-2})	
O1-C1-O1	120.0	67.5	
C1-CH_2-C2	107.8	32.4	
CH_2-C2-CH_2	112.7	58.35	
C1-C2-O2	109.5	50.0	
C2-O2-H1	108.5	55.0	
Torsion			
dihedral	V_1 (kcal mol^{-1})	V_2 (kcal mol^{-1})	V_3 (kcal mol^{-1})
O1-C1-CH_2-C2	0.0	0.820	0.0
C1-CH_2-C2-CH_2	–3.185	–0.825	0.493
C1-CH_2-C2-O2	1.711	–0.5	0.663
(C1, CH_2)-C2-O2-H1	–0.356	0.174	0.492
O1-C1-CH_2-O2	9.066	0.0	0.0

Table A6.1: Force-field parameters for citrate^{3-}.

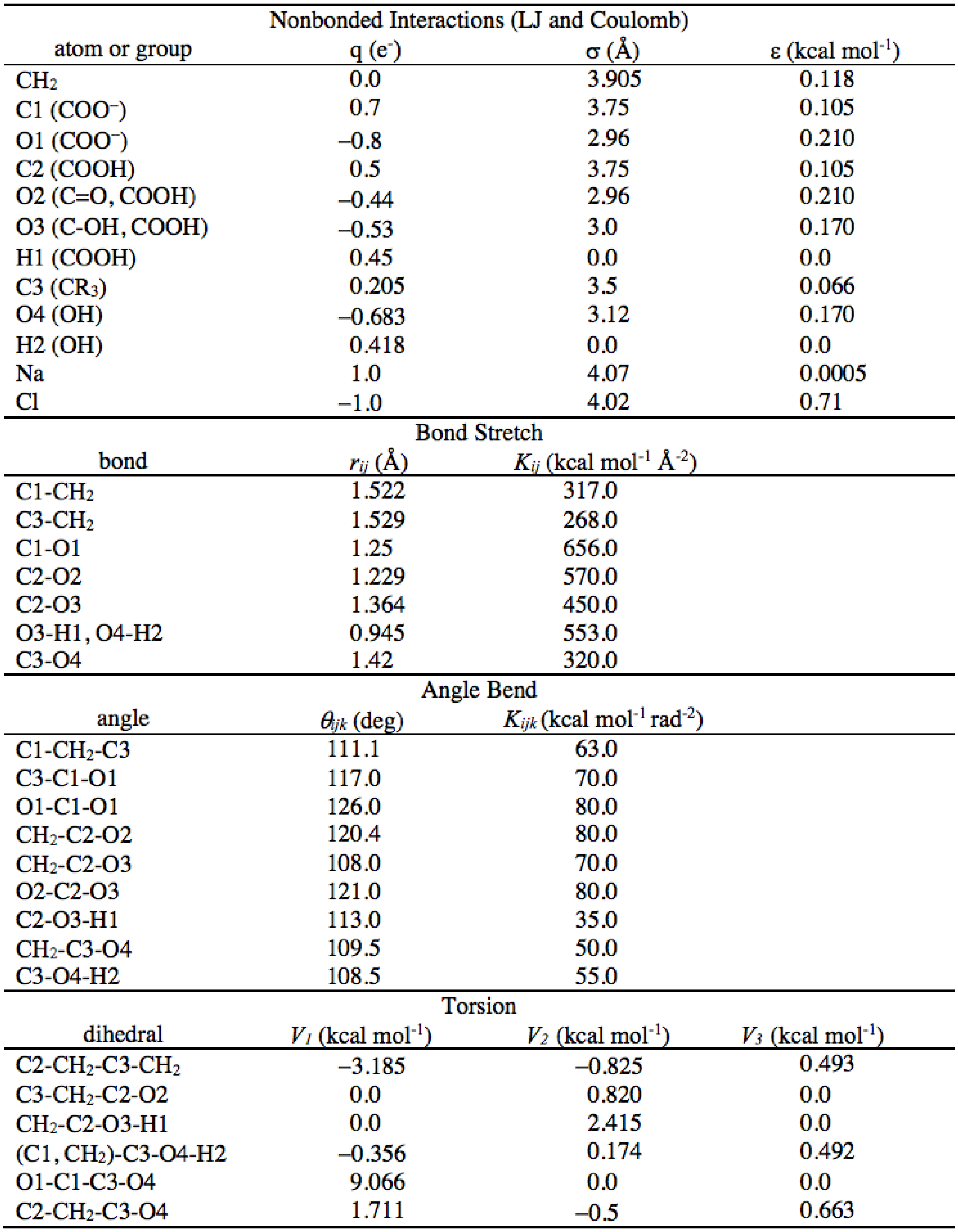

Nonbonded Interactions (LJ and Coulomb)

atom or group	q (e^-)	σ (Å)	ε (kcal mol^{-1})
CH_2	0.0	3.905	0.118
C1 (COO^-)	0.7	3.75	0.105
O1 (COO^-)	−0.8	2.96	0.210
C2 (COOH)	0.5	3.75	0.105
O2 (C=O, COOH)	−0.44	2.96	0.210
O3 (C-OH, COOH)	−0.53	3.0	0.170
H1 (COOH)	0.45	0.0	0.0
C3 (CR_3)	0.205	3.5	0.066
O4 (OH)	−0.683	3.12	0.170
H2 (OH)	0.418	0.0	0.0
Na	1.0	4.07	0.0005
Cl	−1.0	4.02	0.71

Bond Stretch

bond	r_{ij} (Å)	K_{ij} (kcal mol^{-1} $Å^{-2}$)
C1-CH_2	1.522	317.0
C3-CH_2	1.529	268.0
C1-O1	1.25	656.0
C2-O2	1.229	570.0
C2-O3	1.364	450.0
O3-H1, O4-H2	0.945	553.0
C3-O4	1.42	320.0

Angle Bend

angle	θ_{ijk} (deg)	K_{ijk} (kcal mol^{-1} rad^{-2})
C1-CH_2-C3	111.1	63.0
C3-C1-O1	117.0	70.0
O1-C1-O1	126.0	80.0
CH_2-C2-O2	120.4	80.0
CH_2-C2-O3	108.0	70.0
O2-C2-O3	121.0	80.0
C2-O3-H1	113.0	35.0
CH_2-C3-O4	109.5	50.0
C3-O4-H2	108.5	55.0

Torsion

dihedral	V_1 (kcal mol^{-1})	V_2 (kcal mol^{-1})	V_3 (kcal mol^{-1})
C2-CH_2-C3-CH_2	−3.185	−0.825	0.493
C3-CH_2-C2-O2	0.0	0.820	0.0
CH_2-C2-O3-H1	0.0	2.415	0.0
(C1, CH_2)-C3-O4-H2	−0.356	0.174	0.492
O1-C1-C3-O4	9.066	0.0	0.0
C2-CH_2-C3-O4	1.711	−0.5	0.663

Table A6.2: Force-field parameters for $H_2citrate^-$.

System	Number of Citrate	[NaCl] or [Na$^+$], (M)	Total Number of Atoms	Box Size (Å)	Total Simulation Time (ns)
Citrate^{3-}, 4 nm, Implicit	150	[NaCl] = 0.1	5123	250 × 250 × 250	24
H_2citrate$^-$ monolayer, 4 nm, Implicit	150	[NaCl] = 0.1	4823	170 × 170 × 170	20
H_2citrate$^-$ bilayer, 4 nm, Implicit	300	[NaCl] = 0.1	7127	210 × 210 × 210	40
Citrate^{3-}, 6 nm, Implicit	340	[NaCl] = 0.1	13965	320 × 320 × 320	24
H_2citrate$^-$ monolayer, 6 nm, Implicit	340	[NaCl] = 0.1	13285	224 × 224 × 224	24
H_2citrate$^-$ bilayer, 6 nm, Implicit	680	[NaCl] = 0.1	18433	274 × 274 × 274	40
Citrate^{3-}, 8 nm, Implicit	600	[NaCl] = 0.1	33433	390 × 390 × 390	24
H_2citrate$^-$ monolayer, 8 nm, Implicit	600	[NaCl] = 0.1	32233	270 × 270 × 270	24
H_2citrate$^-$ bilayer, 8 nm, Implicit	1200	[NaCl] = 0.1	45913	356 × 356 × 356	40
Citrate^{3-}, 4 nm, Explicit	90	[Na$^+$] = 0.4	119840	105 × 105 × 105	40
H_2citrate$^-$, 4 nm, Explicit	150	[Na$^+$] = 0.4	66311	85 × 85 × 85	40
Citrate^{3-} and PAH$_{200}$, 4 nm, Explicit	90	[NaCl] = 0.25	353253	125 × 145 × 175	25
H_2citrate$^-$ and PAH$_{200}$, 4 nm, Explicit	150	[NaCl] = 0.20	306086	110 × 145 × 170	25

Table A6.3: The characteristic parameters and settings used in the simulations for the model systems discussed in Chapter 6 by AuNP coating, AuNP size, and solvent condition.

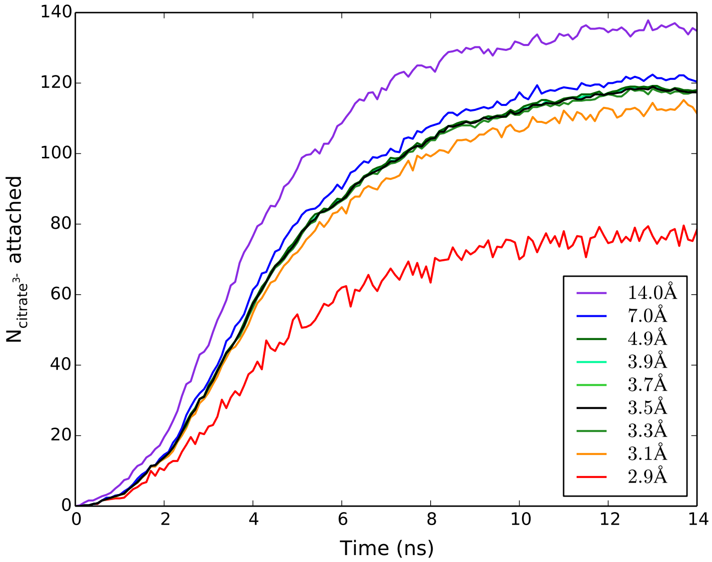

Figure A6.2: Number of citrate^{3-} adsorbed onto the AuNP *vs.* time in implicit solvent, according to distance between an oxygen atom on citrate and gold atoms. Au–O cutoff distances of 2.9 and 3.1 Å undercount the number of citrate adsorbed. Cutoff distances between 3.3 and 4.9 Å capture the monolayer of citrate on the AuNP surface. Cutoff distances of 7.0 and 14.0 Å capture free citrate. Each curve is an average of five trajectories.

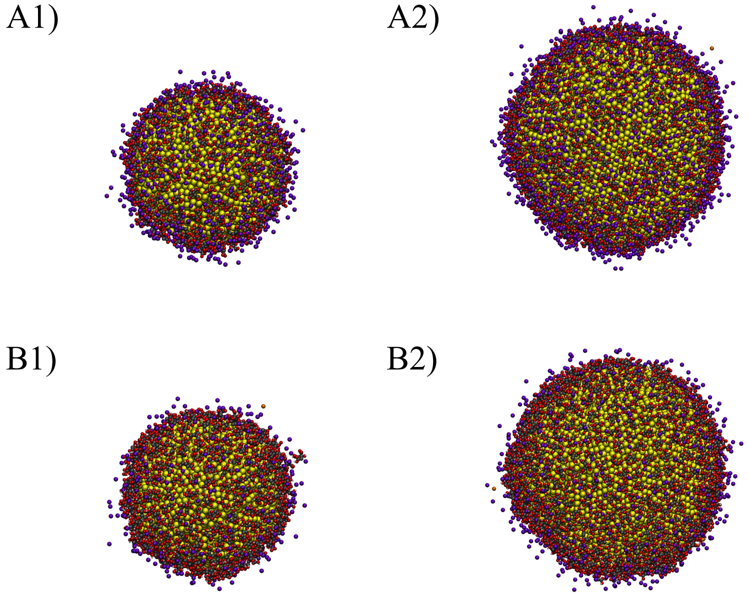

Figure A6.3: Representative snapshots of (A1) citrate^{3-} maximally packed on 6 nm AuNPs, (A2) citrate^{3-} maximally packed on 8 nm AuNPs, (B1) H$_2$citrate^{-} maximally packed on 6 nm AuNPs, and (B2) H$_2$citrate^{-} maximally packed on 8 nm AuNPs all in implicit solvent. Cit-AuNPs consist of gold (yellow), carbon (gray), oxygen (red), and hydrogen (white) atoms. Na^{+} ions are shown in purple and Cl^{-} ions are in orange. Counterions outside the solvent shell are removed for clarity.

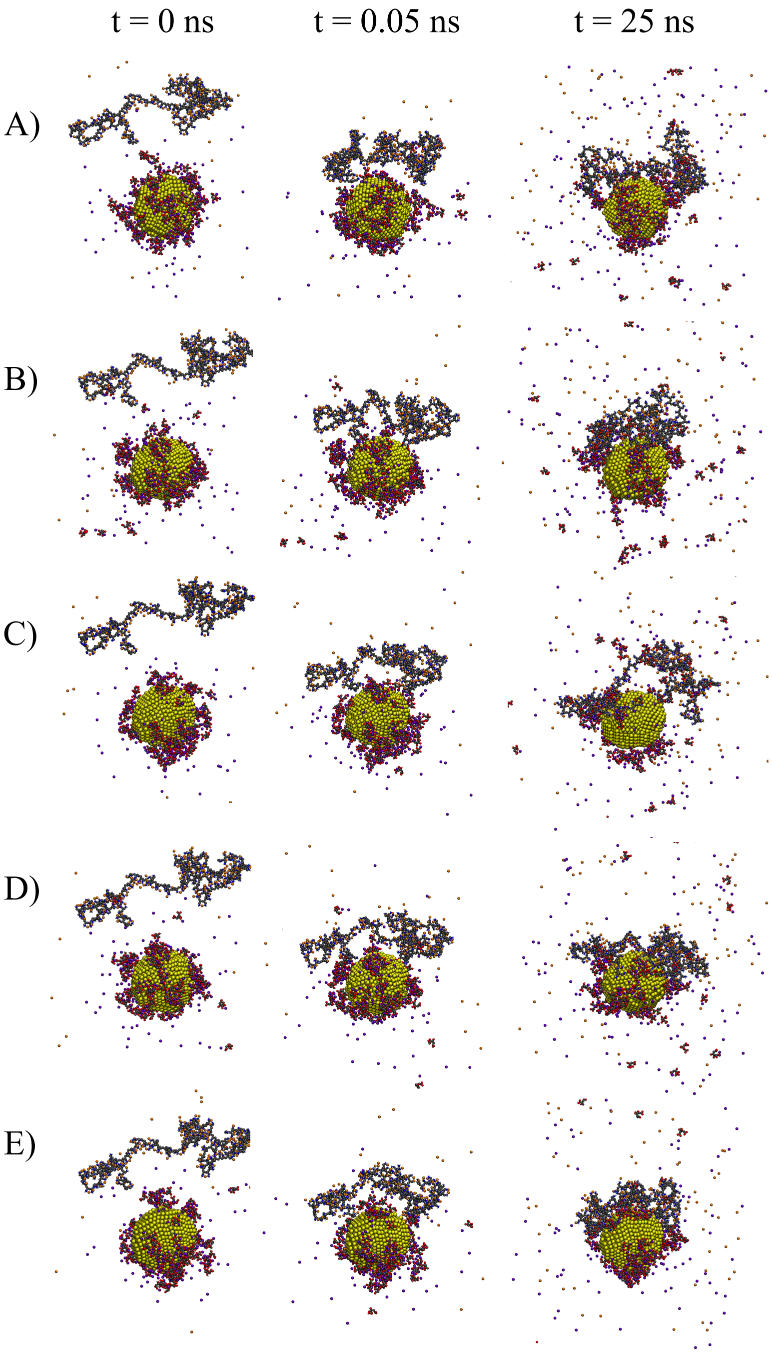

Figure A6.4: Simulation snapshots from five trajectories (A-E) in explicit solvent of citrate^{3-} layers on 4 nm AuNPs in the presence of PAH at the initial configuration (0 ns), after steering PAH to the AuNP surface (0.05 ns), and at the end of equilibration and production runs (25 ns). Gold (yellow), carbon (gray), oxygen (red), hydrogen (white), nitrogen (blue), sodium (purple), and chloride (orange) atoms are shown. Water molecules are not shown for clarity.

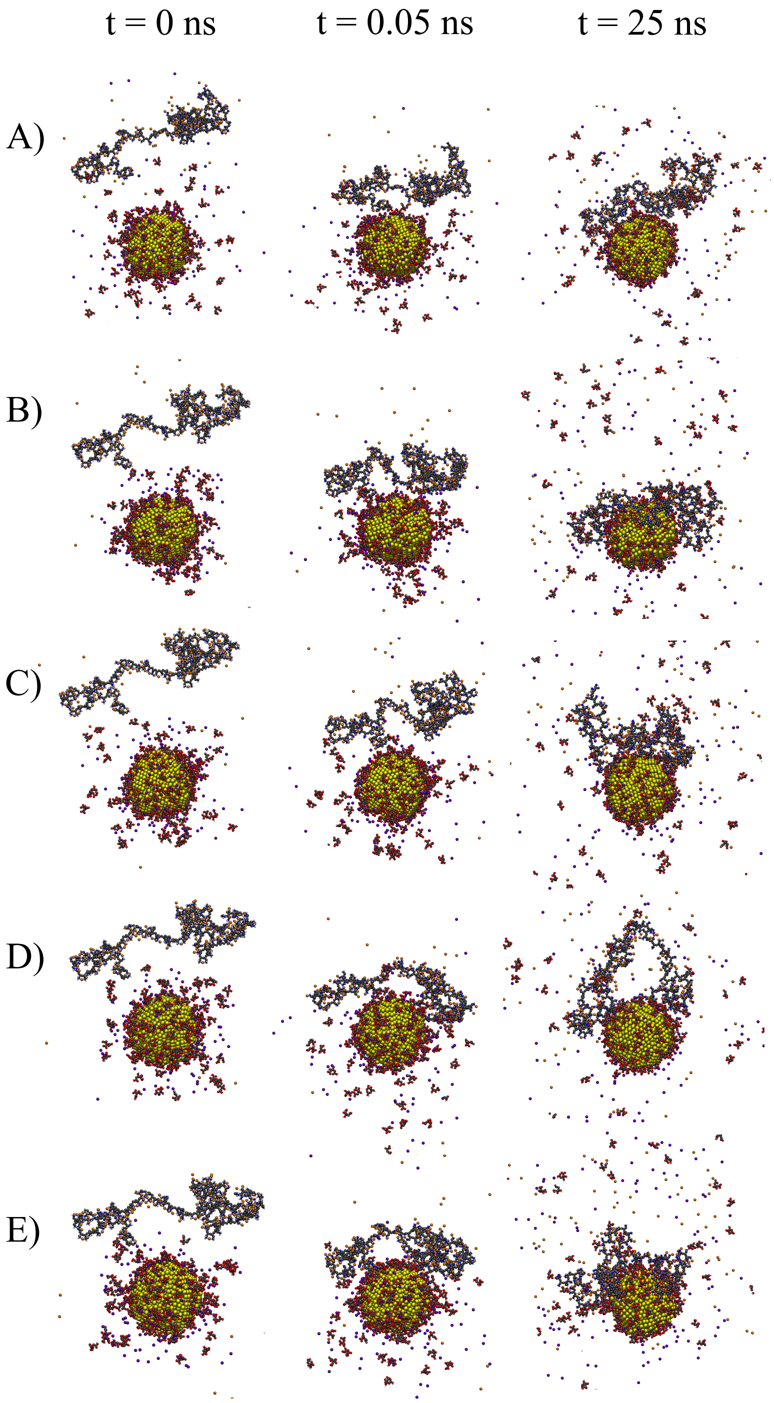

Figure A6.5: Simulation snapshots from five trajectories (A-E) in explicit solvent of H_2citrate$^-$ layers on 4 nm AuNPs in the presence of PAH at the initial configuration (0 ns), after steering PAH to the AuNP surface (0.05 ns), and at the end of equilibration and production runs (25 ns). Gold (yellow), carbon (gray), oxygen (red), hydrogen (white), nitrogen (blue), sodium (purple), and chloride (orange) atoms are shown. Water molecules are not shown for clarity.

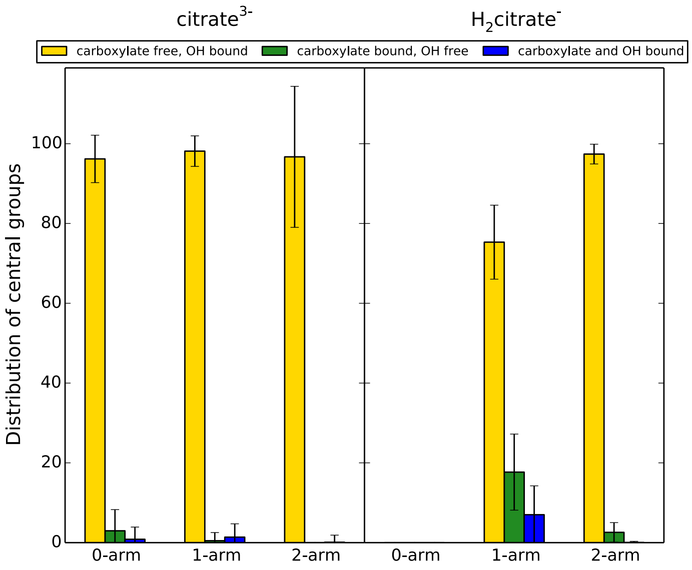

Figure A6.6: Percent of the 0-, 1-, and 2-arm configurations with either the central carboxylate group, hydroxyl group, or both bound to the surface of 4 nm cit-AuNPs in explicit solvent.

A7. Bottom-Up Coarse-Graining of Structurally Complex Nanoparticles and Lipid-Bilayer Systems

The distribution of lipid tail end-to-end distances as a function of lipid count (*i.e.* vesicle size) for all spherical DPD vesicles larger than 10 nm (in diameter) is shown in Figure A7.1. Vesicle self-assembly simulations using the DPD force-field parameters developed and presented in Tables 2 and 3 of Chapter 7 reveal vesicle size-dependent lipid packing with a higher frequency of lipids with smaller end-to-end distances in smaller vesicles, inducing greater curvature. Larger vesicles have lower curvature, and lipid tails pack more upright in the bilayer, as indicated by taller, narrower peaks at larger end-to-end distances.

The radial distribution functions, *g(r)*, between the the vesicle centers of mass and the ammonium, phosphate, glycerol, lipid-tail groups are shown in Figs. A7.2, A7.3, and A7.2). The peak for the density of ammonium groups in the outer layer can be used to determine the radius and, therefore, the size of vesicles assembled in our DPD simulations. Vesicles with 576, 1500, and 4000 lipids are ∼10, 16, and 24 nm in diameter, respectively. The difference between peaks for the lipid-tail group density in the inner and outer layers is consistently 4 nm in agreement with experimental and simulated values for lipid-membrane thickness [191].

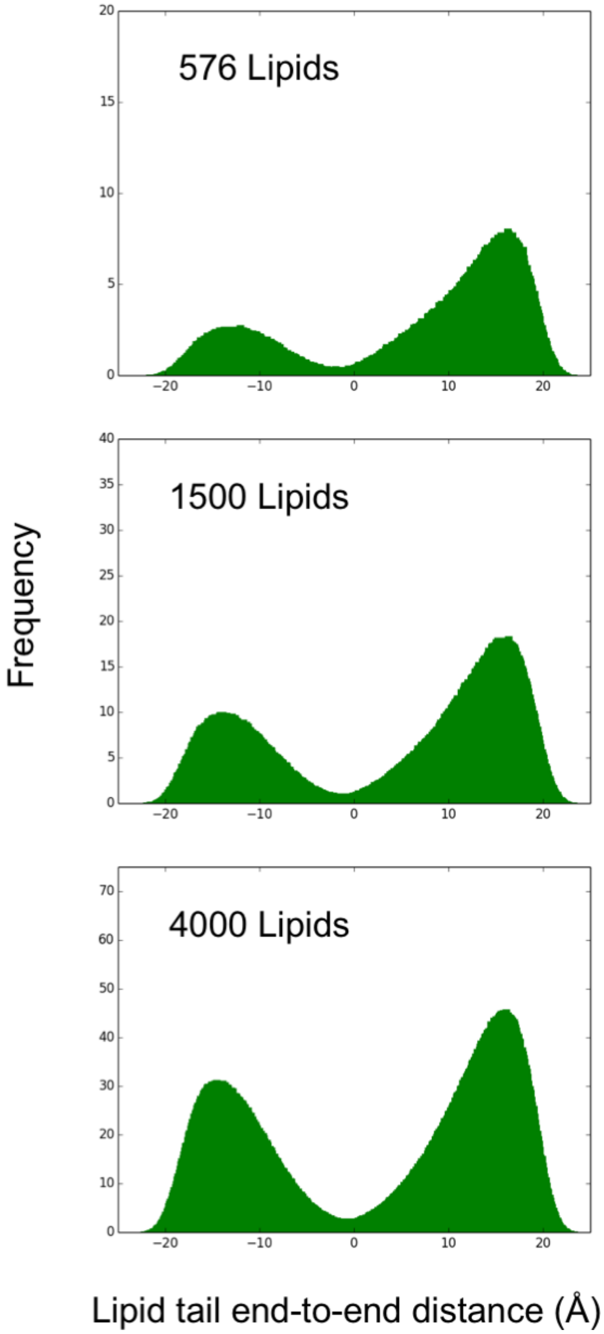

Figure A7.1: Distribution of lipid tail end-to-end distances in 576-, 1500-, and 4000-lipid DPD coarse-grained vesicles.

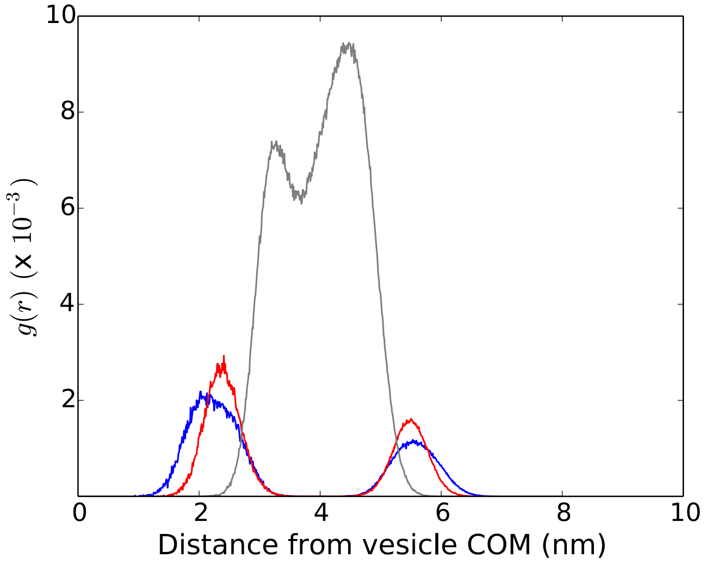

Figure A7.2: *g(r)* between the vesicle COM and ammonium (blue), phosphate (red), and lipid-tail (gray) groups for a 576-lipid DPD vesicle.

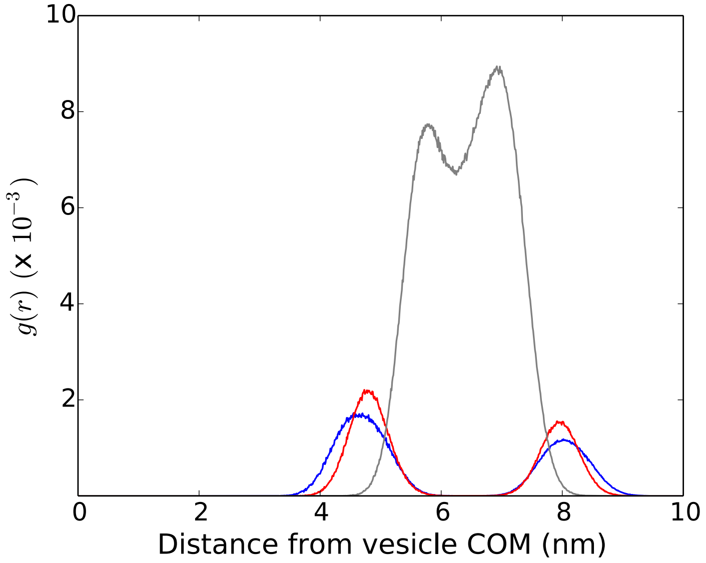

Figure A7.3: *g(r)* between the vesicle COM and ammonium (blue), phosphate (red), and lipid-tail (gray) groups for a 1500-lipid DPD vesicle.

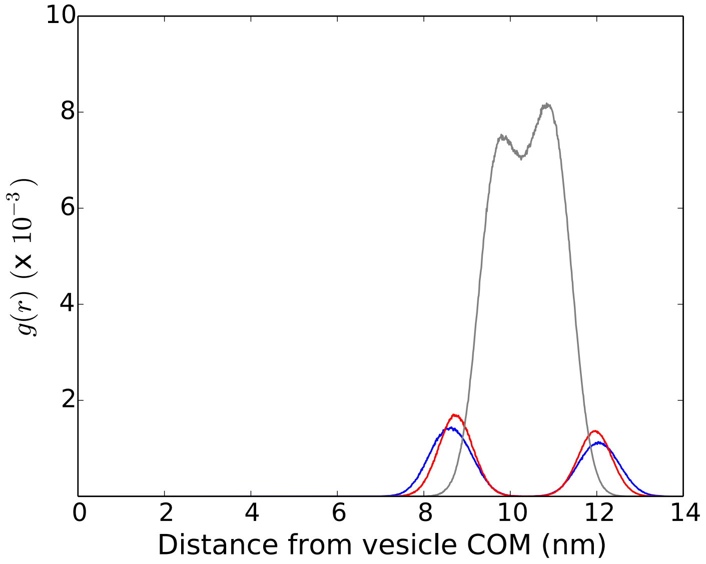

Figure A7.4: *g(r)* between the vesicle COM and ammonium (blue), phosphate (red), and lipid-tail (gray) groups for a 4000-lipid DPD vesicle.

A8. Defects in Self-Assembled Monolayers on Nanoparticles Prompt Lipid Extraction and Bilayer Curvature-Dependent Transformations

Simulation Setup

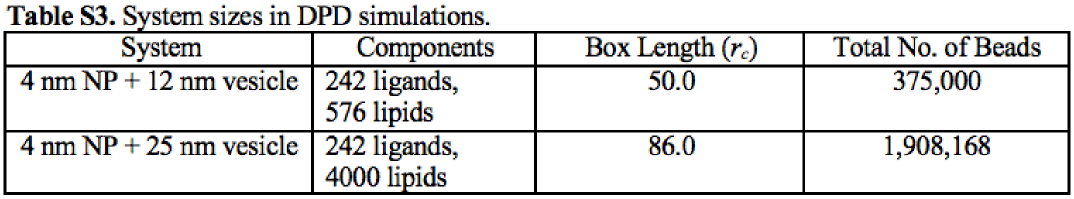

Table S3. System sizes in DPD simulations.

System	Components	Box Length (r_c)	Total No. of Beads
4 nm NP + 12 nm vesicle	242 ligands, 576 lipids	50.0	375,000
4 nm NP + 25 nm vesicle	242 ligands, 4000 lipids	86.0	1,908,168

Table A8.1: System sizes in DPD simulations.

Radial Distribution Functions

The radial distribution functions, *g(r)*'s, between the MUTAB-NP COM and lipid glycerol beads in a 12 nm vesicle (Figure A8.1) and between the vesicle COM and lipid glycerol beads for both 12 nm and 25 nm vesicles (Figure A8.2) were calculated using a bin size of 0.1 Å, normalizing by the annular volume, and averaging over the last 20 frames across each 200,000 timestep trajectory from data output every 1,000 timesteps. The peak in the *g(r)* in Figure A8.1 corresponds to the corona of lipids acquired by the NP upon lipid extraction. The first and second peak in each of the *g(r)*'s in Figure A8.2 correspond to the inner and outer layer of the vesicles, respectively. Nonzero values beyond the radius of the vesicle signify lipid extraction by the NP.

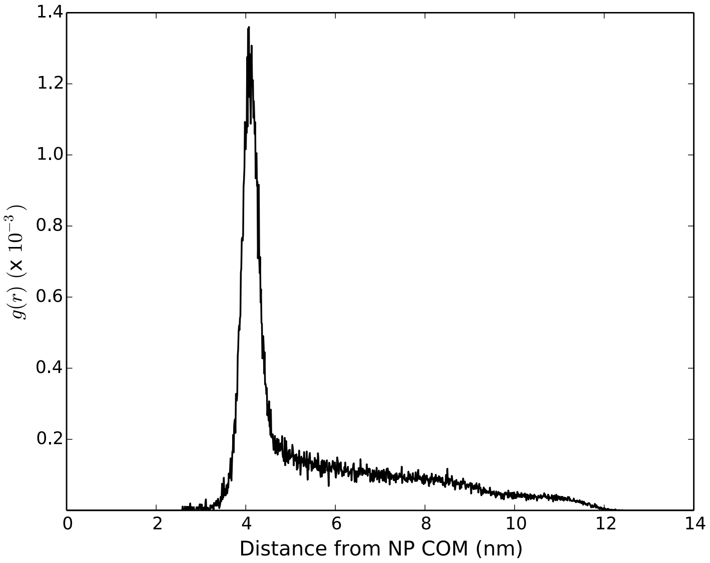

Figure A8.1: *g(r)* between the 4 nm MUTAB-NP COM and lipid glycerol beads from a 12 nm vesicle.

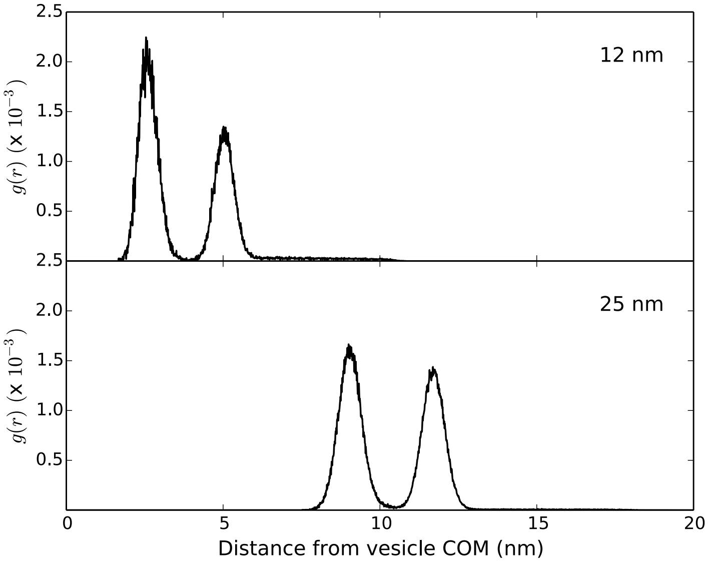

Figure A8.2: *g(r)* between the vesicle COM and lipid glycerol beads for 12 and 25 nm vesicles.

NP Insertion into 25 nm Vesicles, Lipid Extraction, and Water Leakage

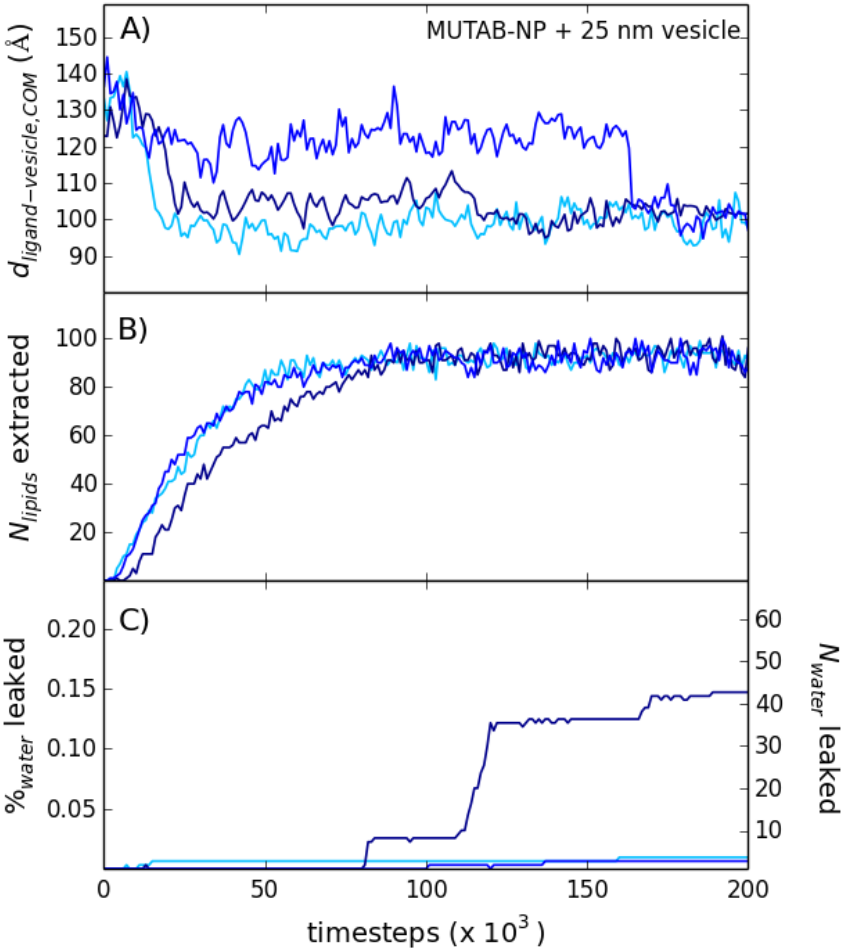

Figure A8.3: A) Distance between NP ligand and vesicle COM, $d_{ligand-vesicle,COM}$ *vs.* time. B) Number of lipids extracted *vs.* time. C) Percent of water and number of water beads leaked from vesicles *vs.* time. Note that each trajectory started with 31,269 water molecules inside the vesicle core. The lipid-tail protrusion event is set as 0 timesteps.

Lipid-Tail Protrusion and Lipid Extraction per Trajectory

The lipid-tail protrusion, lipid extraction, nanoparticle insertion events for the trajectories not presented in Chapter 8 are shown in Figs. A8.4, A8.5, and A8.6, 20000 and 200000 timesteps after the initial lipid-tail protrusion event, set as time $t = 0$. All coarse-grained beads, except for the initial protruding lipid (in solid beads) are made transparent with smaller bead size, and water beads are removed for clarity. Gold beads are in yellow, hydrophobic beads of the NP ligands in gray, hydrophobic beads of the lipids in cyan, lipid glycerol groups in orange, lipid phosphate groups in red, and quaternary ammonium groups of both the lipids and NP ligands in blue.

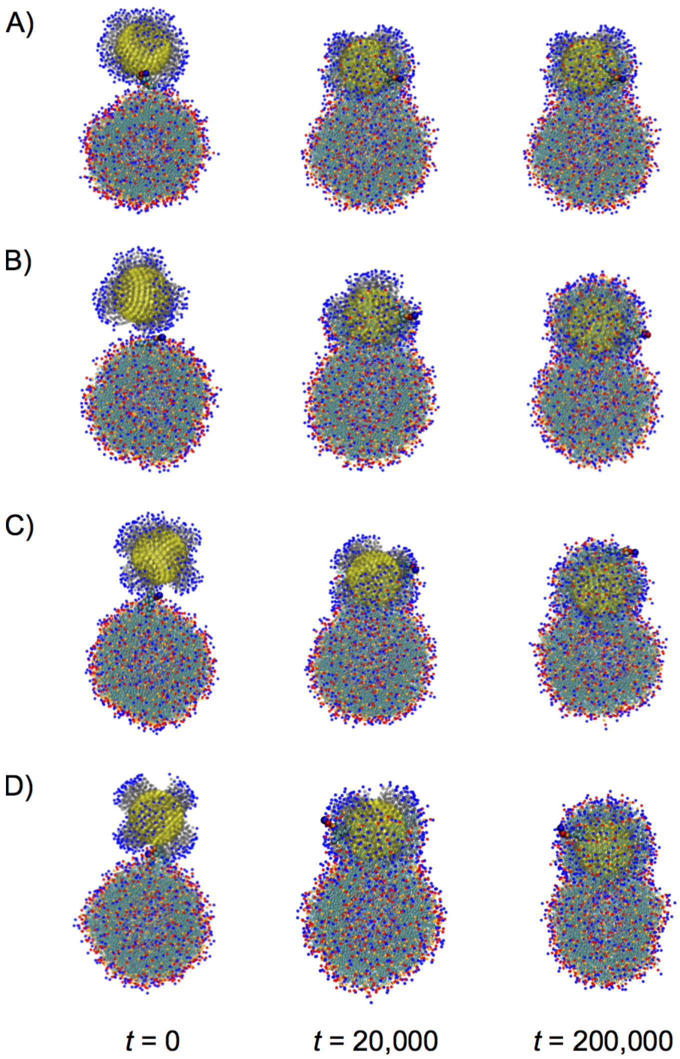

Figure A8.4: Trajectories A-D of 4 nm MUTAB-NPs with a 12 nm vesicle. One trajectory is shown in Figure 47 of Chapter 8.

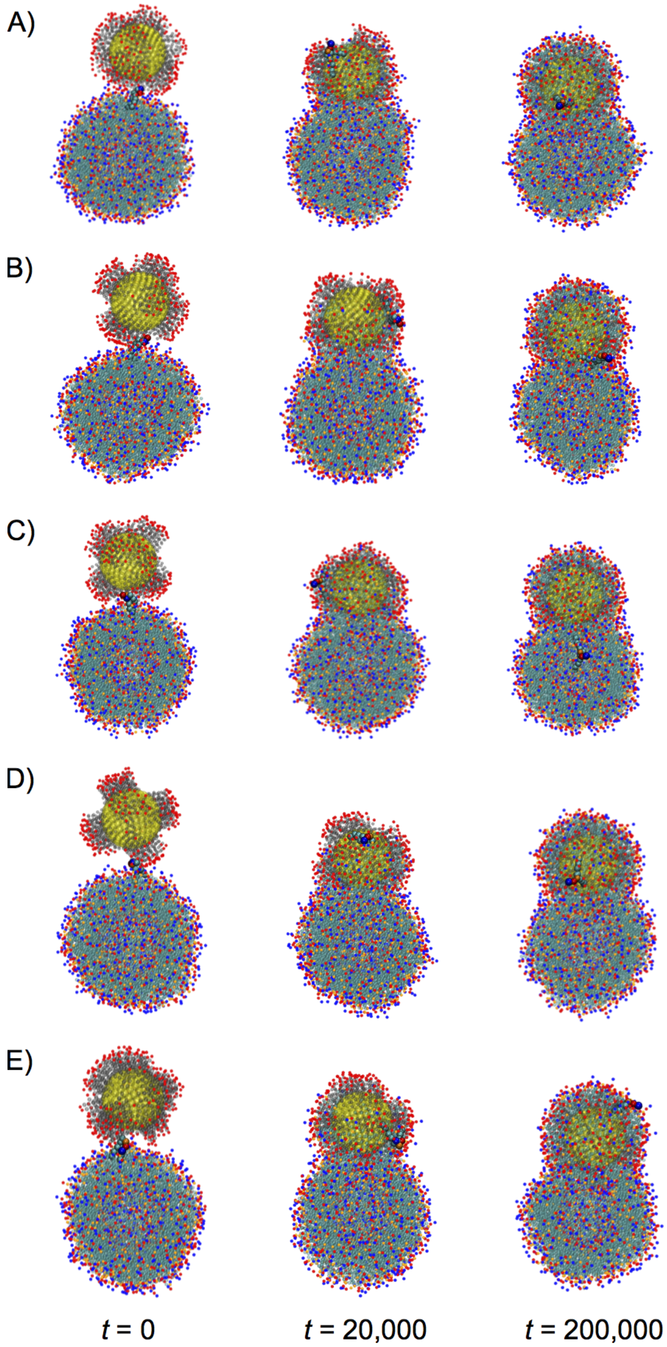

Figure A8.5: Trajectories A-E of 4 nm MUA-NPs with a 12 nm vesicle.

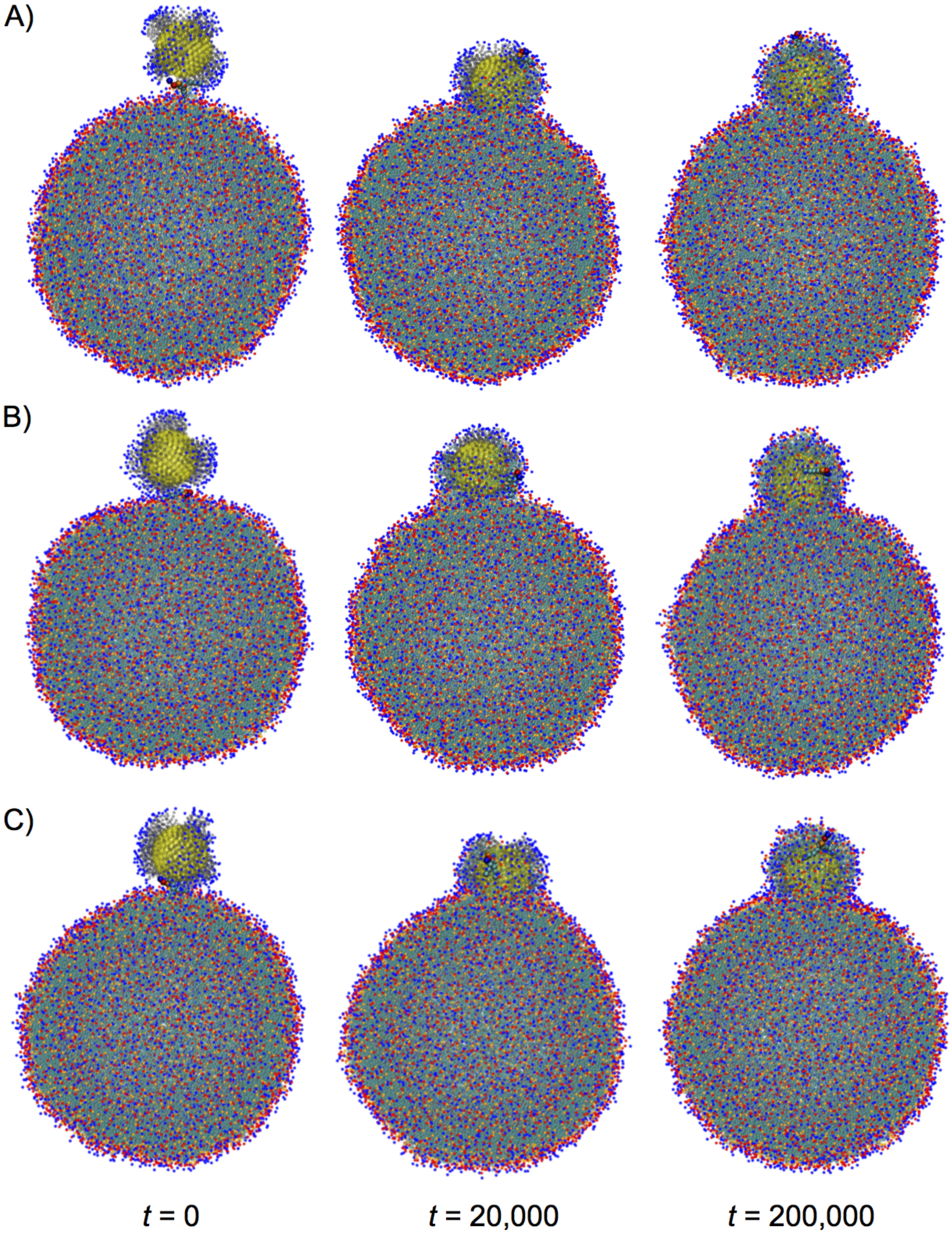

Figure A8.6: Trajectories A-C of 4 nm MUTAB-NPs with a 25 nm vesicle.

Bilayer Thinning per Trajectory

The distribution of lipids by the position of their glycerol groups and the average lipid tail end-to-end distance for each lipid relative to the vesicle COM in Figs. A8.7, A8.8, and A8.9, 200000 and 1 million timesteps after the initial lipid-tail protrusion. Similarity in vesicle structure, including increase in planarized bilayer segments and deviation from a spherical structure in 12 nm vesicles and thinning at the site of NP insertion, at these two timescales and across all individual trajectories show convergence in the structural deformations of the bilayer upon NP insertion.

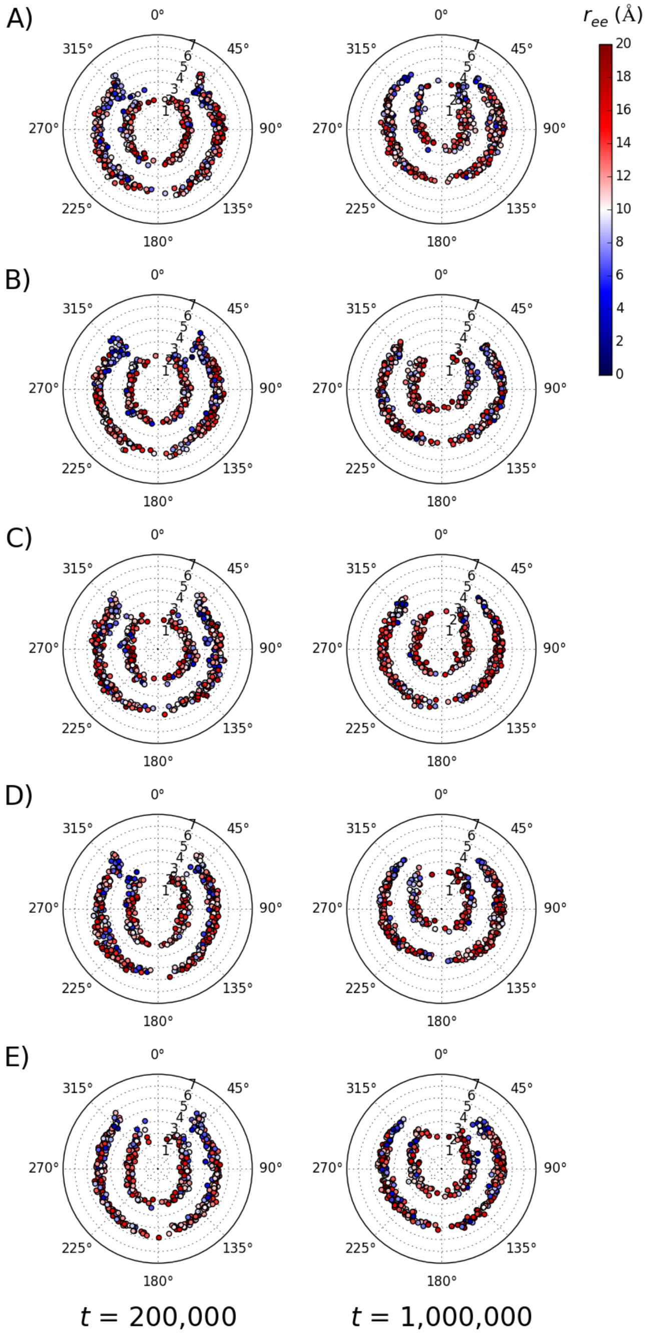

Figure A8.7: Distribution of lipid glycerol groups and the average lipid tail end-to-end distance, r_{ee}, for each lipid in a 12 nm vesicle upon MUTAB-NP exposure in trajectories A-E.

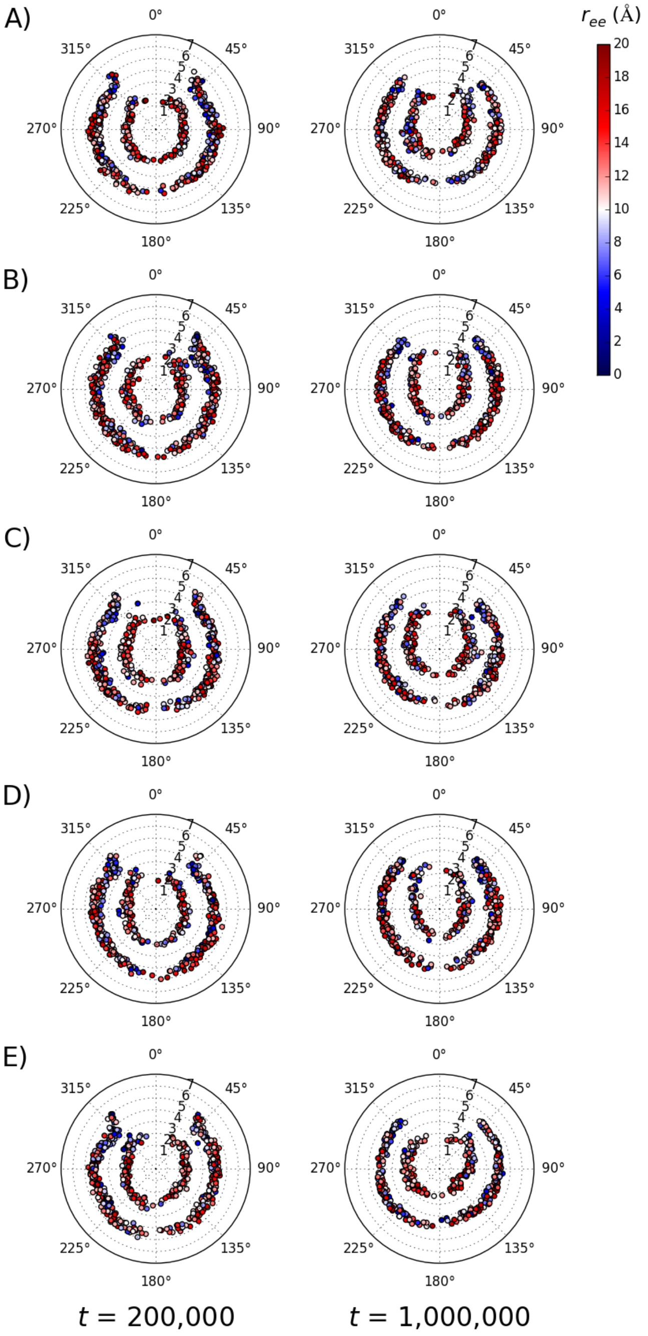

Figure A8.8: Distribution of lipid glycerol groups and the average lipid tail end-to-end distance, r_{ee}, for each lipid in a 12 nm vesicle upon MUA-NP exposure in trajectories A-E.

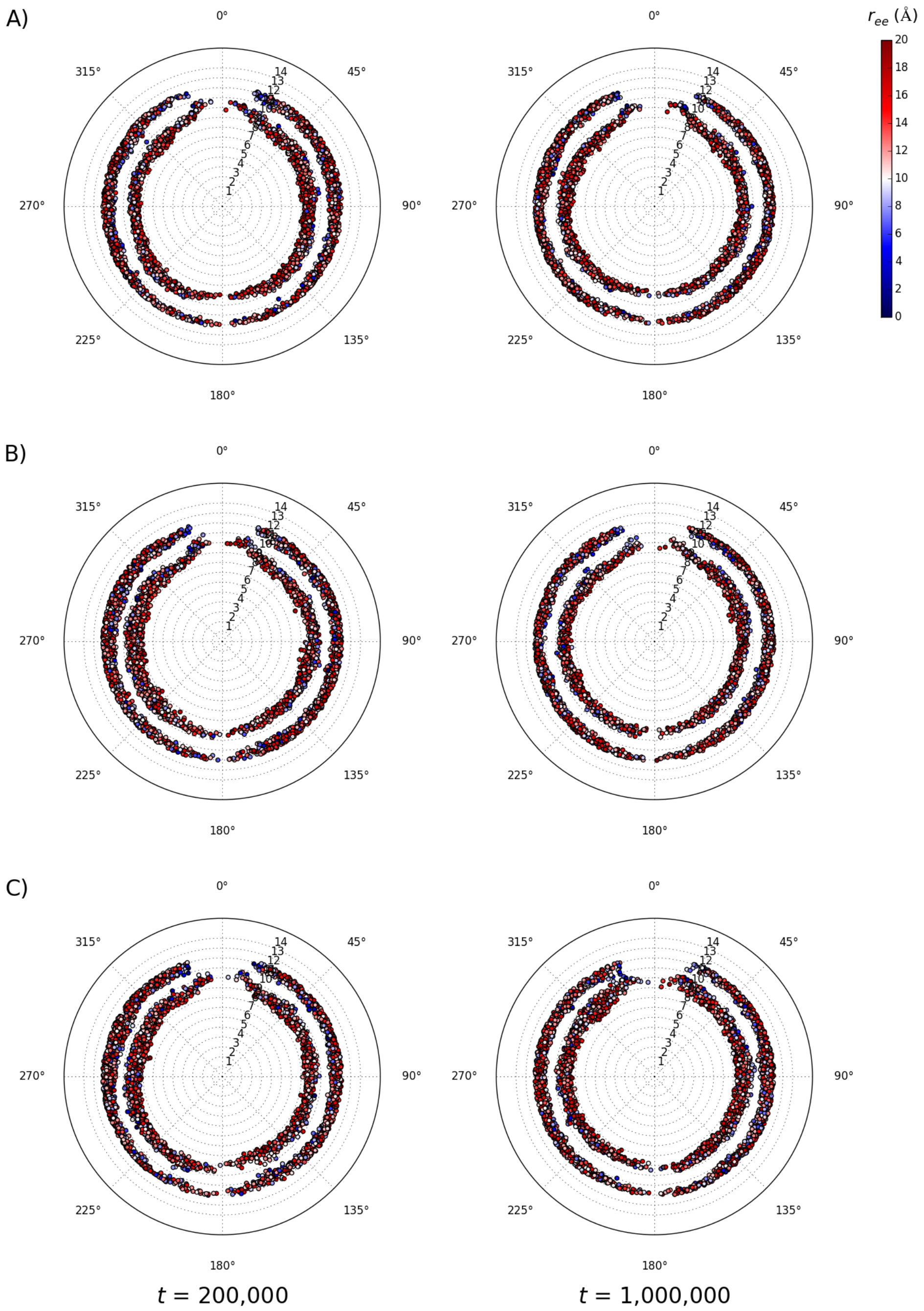

Figure A8.9: Distribution of lipid glycerol groups and the average lipid tail end-to-end distance, r_{ee}, for each lipid in a 25 nm vesicle upon MUTAB-NP exposure in trajectories A-C.

References

[1] Y. Xia, Y. Xiong, B. Lim, and S. E. Skrabalak. Shape-controlled synthesis of metal nanocrystals: Simple chemistry meets complex physics? *Angew. Chem., Int. Ed.*, 48:60–103, 2009.

[2] E. C. Dreaden, A. M. Alkilany, X. Huang, C. J. Murphy, and M. A. El-Sayed. The golden age: Gold nanoparticles for biomedicine. *Chem. Soc. Rev.*, 41:2740–2779, 2012.

[3] M.-C. Daniel and D. Astruc. Gold nanoparticles: Assembly, supramolecular chemistry, quantum size-related properties, and applications toward biology, catalysis, and nanotechnology. *Chem. Rev.*, 104:293–346, 2004.

[4] P. G. Bruce, B. Scrosati, and J.-M. Tarascon. Nanomaterials for rechargeable lithium batteries. *Angew. Chem., Int. Ed.*, 47:2930–2946, 2008.

[5] S. Runa, M. Hussey, and C. K. Payne. Nanoparticle–cell interactions: Relevance for publich health. *J. Phys. Chem. B*, 122:1009–1016, 2017.

[6] C. J. Murphy, A. M. Vartanian, F. M. Geiger, R. J. Hamers, J. A. Pedersen, Q. Cui, C. L. Haynes, E. E. Carlson, R. Hernandez, R. D. Klaper, G. Orr, and Z. Rosenzweig. Biological responses to engineered nanomaterials: Needs for the next decade. *ACS Cent. Sci.*, 1:117123, 2015.

[7] M. A. Maurer-Jones, I. L. Gunsolus, C. J. Murphy, and C. L. Haynes. Toxicity of

engineered nanoparticles in the environment. *Anal. Chem.*, 85:3036–3049, 2013.

[8] C. M. Goodman, C. D. McCusker, T. Yilmaz, and V. M. Rotello. Toxicity of gold nanoparticles functionalized with cationic and anionic side chains. *Bioconjugate Chem.*, 15:897–900, 2004.

[9] R. R. Arvizo, O. R. Miranda, M. A. Thompson, C. M. Pabelick, R. Bhattacharya, J. D. Robertson, V. M. Rotello, Y. S. Prakash, and P. Mukherjee. Effect of nanoparticle surface charge at the plasma membrane and beyond. *Nano Lett.*, 10:2543–2548, 2010.

[10] E. Frölich. The role of surface charge in cellular uptake and cytotoxicity of medical nanoparticles. *Int. J. Nanomed.*, 7:5577–5591, 2012.

[11] Z. V. Feng, I. L. Gunsolus, T. A. Qiu, K. R. Hurley, L. H. Nyberg, H. Frew, K. P. Johnson, A. M. Vartanian, L. M. Jacob, S. E. Lohse, M. D. Torelli, R. J. Hamers, C. J. Murphy, and C. L. Haynes. Impacts of gold nanoparticle charge and ligand type on surface binding and toxicity to Gram-negative and Gram-positive bacteria. *Chem. Sci.*, 6:5186–5196, 2015.

[12] G. A. Dominguez, S. E. Lohse, M. D. Torelli, C. J. Murphy, R. J. Hamers, G. Orr, and R. D. Klaper. Effects of charge and surface ligand properties of nanoparticles on oxidative stress and gene expression within the gut of *Daphnia magna*. *Aquat. Toxicol.*, 162:1–9, 2015.

[13] G. A. Dominguez, M. D. Torelli, J. T. Buchman, C. L. Haynes, R. J. Hamers, and R. D. Klaper. Size dependent oxidative stress response of the gut of *Daphnia magna* to functionalized nanodiamond particles. *Environ. Res.*, 167:267–275, 2018.

[14] L. W. C. Ho, Y. Liu, R. Han, Q. Bai, and C. H. J. Choi. Nano–cell interactions of non-cationic bionanomaterials. *Acc. Chem. Res.*, page

DOI:10.1021/acs.accounts.9b00103, 2019.

[15] P. Falagan-Lotsch, E. M. Grzincic, and C. J. Murphy. One low-dose exposure of gold nanoparticles induces long-term changes in human cells. *Proc. Natl. Acad. Sci. U.S.A.*, 113:13318–13323, 2016.

[16] E. S. Melby, C. Allen, I. U. Foreman-Ortiz, E. R. Caudill, T. R. Kuech, A. M. Vartanian, X. Zhang, C. J. Murphy, R. Hernandez, and J. A. Pedersen. Peripheral membrane proteins facilitate nanoparticle binding at lipid bilayer interfaces. *Langmuir*, 34:10793–10805, 2018.

[17] E. J. Tollefson, C. R. Allen, G. Chong, X. Zhang, N. D. Rozanov, A. Bautista, J. J. Cerda, J. A. Pedersen, C. J. Murphy, E. E. Carlson, and R. Hernandez. Preferential binding of cytochrome *c* to anionic ligand-coated gold nanoparticles: A complementary computational and experimental approach. *ACS Nano*, 13:6856–6866, 2019.

[18] J. N. Anker, W. P. Hall, O. Lyandres, N. C. Shah, J. Zhao, and R. P. Van Duyne. Biosensing with plasmonic nanosensors. *Nat. Mater.*, 7:442–453, 2008.

[19] K. M. Mayer and J. H. Hafner. Localized surface plasmon resonance sensors. *Chem. Rev.*, 111:3828–3857, 2011.

[20] X. Huang, P. K. Jain, I. H. El-Sayed, and M. A. El-Sayed. Plasmonic photothermal therapy (PPTT) using gold nanoparticles. *Lasers Med. Sci.*, 23:217–228, 2008.

[21] E. C. Dreaden, L. A. Austin, M. A. Mackey, and M. A. El-Sayed. Size matters: Gold nanoparticles in targeted cancer drug delivery. *Ther. Deliv.*, 3:457–478, 2012.

[22] Q. Cui, R. Hernandez, S. E. Mason, T. Frauenheim, J. A. Pedersen, and F. Geiger. Sustainable nanotechnology: Opportunities and challenges for theoretical/computational studies. *J. Phys. Chem. B*, 120:7297–7306, 2016.

[23] M. Wu, A. M. Vartanian, G. Chong, A. K. Pandiakumar, R. J. Hamers, R. Hernandez, and C. J. Murphy. Solution NMR analysis of ligand environment in quaternary ammonium-terminated self-assembled monolayers on gold nanoparticles: The effect of surface curvature and ligand structure. *J. Am. Chem. Soc.*, 141:4316–4327, 2019.

[24] G. Chong and R. Hernandez. Adsorption dynamics and structure of polycations on citrate-coated gold nanoparticles. *J. Phys. Chem. C*, 122:19962–19969, 2018.

[25] G. Chong, E. D. Laudadio, M. Wu, C. J. Murphy, R. J. Hamers, and R. Hernandez. Density, structure, and stability of citrate^{3-} and H$_2$citrate$^-$ on bare and coated gold nanoparticles. *J. Phys. Chem. C*, 122:28393–28404, 2018.

[26] L. L. Olenick, J. M. Troiano, A. M. Vartanian, E. S. Melby, A. C. Mensch, L. Zhang, J. Hong, T. A. Qiu, J. S. Bozich, S. E. Lohse, X. Zhang, T. R. Kuech, A. Millevolte, I. L. Gunsolus, A. C. McGeachy, M. Dogangun, T. Li, D. Hu, S. R. Walter, A. Mohaimani, A. Schmoldt, M. D. Torelli, K. R. Hurley, J. Dalluge, G. Chong, Z. V. Feng, C. L. Haynes, R. J. Hamers, J. A. Pedersen, Q. Cui, R. Hernandez, R. D. Klaper, G. Orr, C. J. Murphy, and F. M. Geiger. Lipid corona formation from nanoparticle interactions with bilayers. *Chem*, 4:2709–2723, 2018.

[27] D. Docter, D. Westmeier, M. Markiewicz, S. Stolte, S. K. Knauer, and R. H. Stauber. The nanoparticle biomolecule corona: Lessons learned – challenge accepted? *Chem. Soc. Rev.*, 44:6094–6121, 2015.

[28] C. Corbo, R. Molinaro, A. Parodi, N. A. Toledano Furman, F. Salvatore, and E. Tasciotti. The impact of nanoparticle protein corona on cytotoxicity, immunotoxicity and target drug delivery. *Nanomedicine (Lond.)*, 11:81–100, 2016.

[29] E. Casals, T. Pfaller, A. Duschl, G. J. Oostingh, and V. Puntes. Time evolution of the nanoparticle protein corona. *ACS Nano*, 4:3623–3632, 2010.

[30] D. Walczyk, F. B. Bombelli, M. P. Monopoli, I. Lynch, and K. A. Dawson. What the cell 'sees' in bionanoscience. *J. Am. Chem. Soc.*, 132:5762–5768, 2010.

[31] S. Tenzer, D. Docter, J. Kuharev, A. Musyanovych, V. Fetez, R. Hecht, F. Schlenk, D. Fischer, K. Kiouptsi, C. Reinhardt, K. Landfester, H. Schild, M. Maskos, S. K. Knauer, and R. H. Stauber. Rapid formation of plasma protein corona critically affects nanoparticle pathophysiology. *Nat. Nanotechnol.*, 8:772–781, 2013.

[32] W. Lin, T. Insley, M. D. Tuttle, L. Y. Zhu, D. A. Berthold, P. Král, C. M. Rienstra, and C. J. Murphy. Control of protein orientation on gold nanoparticles. *J. Phys. Chem. C*, 119:21035–21043, 2015.

[33] G. Brancolini, A. Corazza, M. Vuano, F. Fogolari, M. C. Mimmi, V. Bellotti, M. Stoppini, S. Corni, and G. Esposito. Probing the influence of citrate-capped gold nanoparticles on an amyloidogenic protein. *ACS Nano*, 9:2600–2613, 2015.

[34] F. Tavanti, A. Pedone, and M. C. Menziani. A closer look into the ubiquitin corona on gold nanoparticles by computational studies. *New J. Chem.*, 39:2474–2482, 2015.

[35] Q. Shao and C. K. Hall. Protein adsorption on nanoparticles: Model development using computer simulation. *J. Phys.: Condens. Matter*, 28:414019, 2016.

[36] E. S. Melby, S. E. Lohse, J. E. Park, A. M. Vartanian, R. A. Putans, H. B. Abbott, R. J. Hamers, C. J. Murphy, and J. A. Pedersen. Cascading effects of nanoparticle coatings: Surface functionalization dictates the assemblage of complexed proteins and subsequent interaction with model cell membranes. *ACS Nano*, 11:5489–5499, 2017.

[37] X. Zhang, A. K. Pandiakumar, R. J. Hamers, and C. J. Murphy. Quantification of lipid corona formation on colloidal nanoparticles from lipid vesicles. *Anal. Chem.*, 90:14387–14394, 2018.

[38] R. Hernandez and A. V. Popov. Molecular dynamics out of equilibrium: Mechanics and measurables. *WIREs Comput. Mol. Sci.*, 4:541–561, 2014.

[39] J. M. Troiano, T. R. Kuech, A. M. Vartanian, M. D. Torelli, A. Sen, L. M. Jacob, R. J. Hamers, C. J. Murphy, J. A. Pedersen, and F. M. Geiger. On electronic and charge interference in second harmonic generation responses from gold metal nanoparticles at supported lipid bilayers. *J. Phys. Chem. C*, 120:20659–20667, 2016.

[40] M. D. Torelli, R. A. Putans, Y. Tan, S. E. Lohse, C. J. Murphy, and R. J. Hamers. Quantitative determination of ligand densities on nanomaterials by X-ray photoelectron spectroscopy. *ACS Appl. Mater. Interfaces*, 7:1720–1725, 2015.

[41] M. Maccarini, G. Briganti, S. Rucareanu, X.-D. Lui, R. Sinibaldi, M. Sztucki, and R. B. Lennox. Characterization of poly(ethylene oxide)-capped gold nanoparticles in water by means of transmission electron microscopy, thermogravimetric analysis, mass density, and small angle scattering. *J. Phys. Chem. C*, 114:6937–6943, 2010.

[42] J.-W. Park and J. S. Shumaker-Parry. Structural study of citrate layers on gold nanoparticles: Role of intermolecular interactions in stabilizing nanoparticles. *J. Am. Chem. Soc.*, 136:1907–1921, 2014.

[43] H. Al-Johani, E. Abou-Hamad, A. Jedidi, C. M. Widdifield, J. Viger-Gravel, S. S. Sangaru, D. Gajan, D. H. Anjum, S. Ould-Chikh, M. N. Hedhili, A. Gurinov, M. J. Kelly, M. El Eter, L. Cavallo, L. Emsley, and J.-M. Basset. The structure and binding mode of citrate in the stabilization of gold nanoparticles. *Nat. Chem.*,

9:890–895, 2017.

[44] J. Hong, R. J. Hamers, J. A. Pedersen, and Q. Cui. A hybrid molecular dynamics/multiconformer continuum electrostatics (MD/MCCE) approach for the determination of surface charge of nanomaterials. *J. Phys. Chem. C*, 121:3584–3596, 2017.

[45] C. J. Murphy, A. M. Gole, J. W. Stone, P. N. Siscoand, A. M. Alkilany, E. C. Goldsmith, and S. C. Baxter. Gold nanoparticles in biology: Beyond toxicity to cellular imaging. *Acc. Chem. Res.*, 41:1721–1730, 2008.

[46] A. A. Shemetov, I. Nabiev, and A. Sukhanova. Molecular interaction of proteins and peptides with nanoparticles. *ACS Nano*, 6:4584–4602, 2012.

[47] S. H. Brewer, W. R. Glomm, M. C. Johnson, M. K. Knag, and S. Franzen. Probing BSA binding to citrate-coated gold nanoparticles and surfaces. *Langmuir*, 21:9303–9307, 2005.

[48] S. H. D. P. Lacerda, J. J. Park, C. Meuse, D. Pristinski, M. L. Becker, A. Karim, and J. F. Douglas. Interaction of gold nanoparticles with common human blood proteins. *ACS Nano*, 4:365–379, 2010.

[49] G. Maiorano, S. Sabella, B. Sorce, V. Brunetti, M. A. Malvindi, R. Cingolani, and P. P. Pompa. Effects of cell culture media on the dynamic formation of protein-nanoparticle complexes and influence on the cellular response. *ACS Nano*, 4:7481–7491, 2010.

[50] F. Tavanti, A. Pedone, and M. C. Menziani. Competitive binding of proteins to gold nanoparticles disclosed by molecular dynamics simulations. *J. Phys. Chem. C*, 119:22172–22180, 2015.

[51] J. Smith, K. G. Sprenger, R. Liao, A. Joseph, E. Nance, and J. Pfaendtner.

Determining dominant driving forces affecting controlled protein release from polymeric nanoparticles. *Biointerphases*, 12:02D412, 2017.

[52] G. Brancolini and V. Tozzini. Multiscale modeling of proteins interaction with functionalized nanoparticles. *Curr. Opin. Colloid Interface Sci.*, 41:66–73, 2019.

[53] V. L. Mendoz and R. W. Vachet. Probing protein structure by amino acid-specific covalent labeling and mass spectrometry. *Mass Spectrom. Rev.*, 28:785–815, 2009.

[54] L. Wang and M. R. Chance. Protein footprinting comes of age: Mass spectrometry for biophysical structure assessment. *Mol. Cell. Proteomics*, 16:706–716, 2017.

[55] S. Shrivastava, J. H. Nuffer, R. W. Siegel, and J. S. Dordick. Position-specific chemical modification and quantitative proteomics disclose protein orientation adsorbed on silica nanoparticles. *Nano Lett.*, 12:1583–1587, 2012.

[56] S. Shrivastava, S. A. McCallum, J. H. Nuffer, X. Qian, R. W. Siegel, and J. S. Dordick. Identifying specific protein residues that guide surface interactions and orientation on silica nanoparticles. *Langmuir*, 29:10841–10849, 2013.

[57] H. Bayraktar, C.-C. You, V. M. Rotello, and M. J. Knapp. Facial control of nanoparticle binding to cytochrome *c*. *J. Am. Chem. Soc.*, 129:2732–2733, 2007.

[58] S. Devineau, C. Mathé, V. Legros, F. Gonnet, R. Daniel, J. P. Renault, and S. Pin. The nano-bio interface mapped by oxidative footprining of the adsorption sites of myoglobin. *Anal. Bioanal. Chem.*, 406:8037–8040, 2014.

[59] J. C. Reed. Cytochrome *c*: Can't live with it - can't live without it. *Cell*, 91:559–562, 1997.

[60] E. K. Tuominen, C. J. Wallace, and P. K. Kinnunen. Phospholipid-cytochrome *c* interaction: Evidence for the extended lipid anchorage. *J. Biol. Chem.*, 277:8822–8826, 2002.

[61] E. Kalanxhi and C. J. Wallace. Cytochrome *c* impaled: Investigation of the extended lipid anchorage of a soluble protein to mitochondrial membrane models. *Biochem. J.*, 407:179–187, 2007.

[62] M. Rytömaa and P. K. J. Kinnunen. Evidence for two distinct acidic phospholipid-binding sites in cytochrome *c*. *J. Biol. Chem.*, 269:1770–1774, 1994.

[63] M. Rytömaa and P. K. J. Kinnunen. Reversibility of the binding of cytochrome *c* to liposomes: Implications for lipid-protein interactions. *J. Biol. Chem.*, 270:3197–3202, 1995.

[64] M. M. Elmer-Dixon and B. E. Bowler. Electrostatic constituents of the interaction of cardiolipin with site A of cytochrome *c*. *Biochemistry*, 57:5683–5695, 2018.

[65] E. Casals, T. Pfaller, A. Duschl, G. J. Oostingh, and V. F. Puntes. Hardening of the nanoparticle-protein corona in metal (Au, Ag) and oxide Fe_3O_4, CoO, and CeO_2) nanoparticles. *Small*, 7:3479–3486, 2011.

[66] A. L. Wang, Y. R. Perera, M. B. Davidson, and N. C. Fitzkee. Electrostatic interactions and protein competition reveal a dynamic surface in gold nanoparticle-protein adsorption. *J. Phys. Chem. C*, 120:24231–24239, 2016.

[67] L. Banci, I. Bertini, H. B. Gray, C. Luchinat, T. Reddig, A. Rosato, and P. Turano. Solution structure of oxidized horse heart cytochrome *c*. *Biochemistry*, 36:9867–9877, 1997.

[68] R. B. Best, X. Zhu, J. Shim, P. E. Lopes, J. Mittal, M. Feig, and A. D. MacKerell, Jr. Optimization of the additive CHARMM all-atom protein force field targeting improved sampling of the backbone phi, psi and side-chain chi(1) and chi(2) dihedral angles. *J. Chem. Theory Comput.*, 8:3257–3273, 2012.

[69] J. Huang and A. D. MacKerell, Jr. CHARMM36 all-atom additive protein

force field: Validation based on comparison to NMR data. *J. Comput. Chem.*, 34:2135–2145, 2013.

[70] L. Kalé, R. Skeel, M. Bhandarkar, R. Brunner, A. Gursoy, N. Krawetz, J. Phillips, A. Shinozaki, K. Varadarajan, and K. Schulten. NAMD2: Greater scalability for parallel molecular dynamics. *J. Comput. Phys.*, 151:283–312, 1999.

[71] E. S. O'Brien, N. V. Nucci, B. Fuglestad, C. Tommos, and A. J. Wand. Defining the apoptotic trigger: The interaction of cytochrome *c* and cardiolipin. *J. Biol. Chem.*, 290:30879–30887, 2015.

[72] C. Kawai, F. M. Prado, G. L. Nunes, P. Di Mascio, A. M. Carmona-Ribeiro, and I. L. Nantes. pH-dependent interaction of cytochrome *c* with mitochondrial mimetic membranes: The role of an array of positively charged amino acids. *J. Biol. Chem.*, 280:34709–34717, 2005.

[73] F. Sinibaldi, B. D. Howes, E. Droghetti, F. Polticelli, M. C. Piro, D. Di Pierro, L. Fiorucci, M. Coletta, G. Smulevich, and R. Santucci. Role of lysines in cytochrome *c*-cardiolipin interaction. *Biochemistry*, 52:4578–4588, 2013.

[74] P. K. J. Kinnunen, A. Koiv, J. Y. A. Lehtonen, M. Rytömaa, and P. Mustonen. Lipid dynamics and peripheral interactions of proteins with membrane surfaces. *Chem. Phys. Lipids*, 73:181–207, 1994.

[75] F. Tavanti, A. Pedone, P. Matteini, and M. C. Menziani. Computational insight into the interaction of cytochrome *c* with wet and PVP-coated Ag surfaces. *J. Phys. Chem. B*, 121:9532–9540, 2017.

[76] M. Karaoke, Y. Hagihara, K. Mihara, and Y. Goto. Molten globule of cytochrome *c* studied by small-angle X-ray scattering. *J. Mol. Biol.*, 229:591–596, 1993.

[77] N. J. Greenfield. Using circular dichroism spectra to estimate protein secondary

structure. *Nat. Protoc.*, 1:2876–2890, 2006.

[78] S. M. Kelly, T. J. Jess, and N. C. Price. How to study proteins by circular dichroism. *Biochim. Biophys. Acta, Proteins Proteomics*, 1751:119–139, 2005.

[79] C. J. Barrow, A. Yasuda, P. T. M. Kenny, and M. G. Zagorski. Solution conformations and aggregational porperties of synthetic amyloid β-peptides of Alzheimer's Disease: Analysis of circular dichroism spectra. *J. Mol. Biol.*, 225:1075–1093, 1992.

[80] P. Wallimann, R. J. Kennedy, J. S. Miller, W. Shalongo, and D. S. Kemp. Dual wavelength parametric test of two-state models for circular dichroism spectra of helical polypeptides: Anomalous dichroic properties of alanine-rich peptides. *J. Am. Chem. Soc.*, 125:1203–1220, 2003.

[81] E. Valusova, P. Svec, and M. Antalik. Structural and thermodynamic behavior of cytochrome *c* assembled with glutathione-covered gold nanoparticles. *J. Biol. Inorg. Chem.*, 14:621–630, 2009.

[82] W. Shang, J. H. Nuffer, V. A. Muñiz-Papandrea, W. Colón, R. W. Siegel, and J. S. Dordick. Cytochrome *c* on silica nanoparticles: Influence of nanoparticle size on protein structure, stability, and activity. *Small*, 5:470–476, 2009.

[83] M.-E. Aubin-Tam and K. Hamad-Schifferli. Gold nanoparticle-cytochrome *c* complexes: The effect of nanoparticle ligand charge on protein structure. *Langmuir*, 21:12080–12084, 2005.

[84] X. Jiang, J. Jiang, Y. Jin, E. Wang, and S. Dong. Effect of colloidal gold size on the conformational changes of adsorbed cytrochrome *c*: Probing by circular dichroism, UV-visible, and infrared spectroscopy. *Biomacromolecules*, 6:46–53, 2005.

[85] H.-Z. Zhao, Q. Du, Z.-S. Li, and Q.-Z. Yang. Mechanisms for the direct electron transfer of cytochrome *c* induced by multi-walled carbon nanotubes. *Sensors*, 12:10450–10462, 2012.

[86] N. Sreerama and R. W. Woody. Estimation of protein secondary structure from circular dichroism spectra: Comparison of CONTIN, SELCON, and CDSSTR methods with an expanded reference set. *Anal. Biochem.*, 287:252–260, 2000.

[87] G. Balakrishnan, Y. Hu, and T. G. Spiro. His26 protonation in cytochrome *c* triggers microsecond β-sheet formation and heme exposure: Implications for apoptosis. *J. Am. Chem. Soc.*, 134:19061–19069, 2012.

[88] K. Nakano, T. Yoshitake, Y. Yamashita, and E. F. Bowden. Cytochrome *c* self-assembly on alkanethiol monolayer electrodes as characterized by AFM, IR, QCM, and direct electrochemistry. *Langmuir*, 23:6270–6275, 2007.

[89] A. F. Loftus, K. P. Reighard, S. A. Kapourales, and M. C. Leopold. Monolayer-protected nanoparticle film assemblies as platforms for controlling interfacial and adsorption properties in protein monolayer electrochemistry. *J. Am. Chem. Soc.*, 130:1649–1661, 2008.

[90] S. Wei, L. S. Ahlstrom, and C. L. Brooks, III. Exploring protein-nanoparticle interactions with coarse-grained protein folding models. *Small*, 13:1603748, 2017.

[91] K. E. Woods, Y. R. Perera, M. B. Davidson, C. A. Wilks, D. K. Yadav, and N. C. Fitzkee. Understanding protein structure deformation on the surface of gold nanoparticles of varying size. *J. Phys. Chem. C*, 120:27944–27953, 2016.

[92] A. Albanese, P. S. Tang, and W. C. W. Chan. The effect of nanoparticle size, shape, and surface chemistry on biological systems. *Annu. Rev. Biomed. Eng.*, 14:1–16, 2012.

[93] J. C. Love, L. A. Estroff, J. K. Kriebel, R. G. Nuzzo, and G. M. Whitesides. Self-assembled monolayers of thiolates on metals as a form of nanotechnology. *Chem. Rev.*, 105:1103–1169, 2005.

[94] S. T. Kim, K. Saha, C. Kim, and V. M. Rotello. The role of surface functionality in determining nanoparticle cytotoxicity. *Acc. Chem. Res.*, 46:681–691, 2013.

[95] C. S. Weisbecker, M. V. Merritt, and G. M. Whitesides. Molecular self-assembly of aliphatic thiols on gold colloids. *Langmuir*, 12:3763–3772, 1996.

[96] S. D. Techane, L. J. Gamble, and D. G. Castner. Multitechnique characterization of self-assembled carboxylic acid-terminated alkanethiol monolayers on nanoparticle and flat gold surfaces. *J. Phys. Chem. C*, 115:9432–9441, 2011.

[97] M. Azubel, J. Koivisto, S. Malola, D. Bushnell, G. K. Hura, A. L. Koh, H. Tsunoyama, T. Tsukuna, M. Pettersson, H. Häkkinen, and R. D. Kornberg. Electron microscopy of gold nanoparticles at atomic resolution. *Science*, 345:909–912, 2014.

[98] X. Liu, M. Yu, H. Kim, M. Mameli, and F. Stellacci. Determination of monolayer-protected gold nanoparticle ligand-shell morphology using NMR. *Nat. Commun.*, 3:1182, 2012.

[99] E. Colangelo, J. Comenge, D. Paramelle, M. Volk, Q. Chen, and R. Lévy. Characterizing self-assembled monolayers on gold nanoparticles. *Bioconjugate Chem.*, 28:11–22, 2016.

[100] H. Zeger and J. C. Martins. A solution NMR toolbox for characterizing the surface chemistry of colloidal nanocrystals. *Chem. Mater.*, 25:1211–1221, 2013.

[101] I. Moreels, Y. Justo, B. De Geyter, K. Haustraete, J. C. Martins, and Z. Hens. Size-tunable, bright, and stable PbS quantum dots: A surface chemistry study.

ACS Nano, 5:2004–2012, 2011.

[102] Y. Q. Zhang, C. G. Fry, J. A. Pedersen, and R. J. Hamers. Dynamics and morphology of nanoparticle-linked polymers elucidated by nuclear magnetic resonance. *Anal. Chem.*, 89:12399–12407, 2017.

[103] A. Cros-Gagneux, F. Delpech, C. Nayral, A. Cornejo, Y. Coppel, and B. Chaudret. Surface chemistry of InP quantum dots: A comprehensive study. *J. Am. Chem. Soc.*, 132:18147–18157, 2010.

[104] M. A. Boles, D. Ling, T. Hyeon, and D. V. Talapin. The surface science of nanocrystals. *Nat. Mater.*, 15:141–153, 2016.

[105] A. Badia, R. B. Lennox, and L. Reven. A dynamic view of self-assembled monolayers. *Acc. Chem. Res.*, 33:475–481, 2000.

[106] B. S. Zelakiewicz, A. C. de Dios, and Y. Tong. ^{13}C NMR spectroscopy of $^{13}C_1$-labeled octanethiol-protected Au nanoparticles: Shifts, relaxations, and particle-size effect. *J. Am. Chem. Soc.*, 125:18–19, 2003.

[107] L. Vigerman, P. Manna, and E. R. Zubarev. Quantitative replacement of cetyl trimethylammonium bromide by cationic thiol ligands on the surface of gold nanorods and their extremely large uptake by cancer cells. *Angew. Chem., Int. Ed.*, 51:636–641, 2012.

[108] M. J. Hostetler, J. E. Wingate, C. J. Zhong, J. E. Harris, R. W Vachet, M. R. Clark, J. D. Londono, S. J. Green, J. J. Stokes, G. D. Wignall, G. L. Glish, M. D. Porter, N. D. Evans, and R. W. Murray. Alkanethiolate gold cluster molecules with core diameters from 1.5 to 5.2 nm: Core and monolayer properties as a function of core size. *Langmuir*, 14:17–30, 1998.

[109] W. L. Jorgensen, D. S. Maxwell, and J. Tirado-Rives. Development and testing

of the OPLS all-atom force field on conformational energetics and properties of organic liquids. *J. Am. Chem. Soc.*, 118:11225–11236, 1996.

[110] P. K. Ghorai and S. C. Glotzer. Molecular dynamics simulation study of self-assembled monolayers of alkanethiol surfactants on spherical gold nanoparticles. *J. Phys. Chem. C*, 111:15857–15862, 2007.

[111] D. S. Bolintineanu, J. M. D. Lane, and G. S. Grest. Effects of functional groups and ionization on the structure of alkanethiol-coated gold nanoparticles. *Langmuir*, 30:11075–11085, 2014.

[112] H. Heinz, R. A. Vaia, B. L. Farmer, and R. R. Naik. Accurate simulation of surfaces and interfaces of face-centered cubic metals using 12-6 and 9-6 Lennard-Jones potentials. *J. Phys. Chem. C*, 112:17281–17290, 2008.

[113] T. K. Xia, J. Ouyang, M. W. Ribarsky, and U. Landman. Interfacial alkane films. *Phys. Rev. Lett.*, 69:1967–1970, 1992.

[114] W. D. Luedtke and U. Landman. Structure and thermodynamics of self-assembled monolayers on gold nanocrystallites. *J. Phys. Chem. B*, 102:6566–6572, 1998.

[115] L. Martínez, R. Andrade, E. G. Birgin, and J. M. Martínez. Packmol: A package for building initial configurations for molecular dynamics simulations. *J. Comput. Chem.*, 30:2157–2164, 2009.

[116] S. Plimpton. Fast parallel algorithms for short-range molecular-dynamics. *J. Comput. Phys.*, 117:1–19, 1995.

[117] W. Haiss, N. T. K. Thanh, J. Aveyard, and D. G. Fernig. Determination of size and concentration of gold nanoparticles from UV-vis spectra. *Anal. Chem.*, 79:4215–4221, 2007.

[118] X. Cui, S. Mao, M. Liu, H. Yuan, and Y. Du. Mechanism of surfactant micelle

formation. *Langmuir*, 24:10771–10775, 2008.

[119] Y. Ahn, J. K. Saha, G. C. Schatz, and J. Jang. Molecular dynamics study of the formation of a self-assembled monolayer on gold. *J. Phys. Chem. C*, 115:10668–10674, 2011.

[120] M. T. Frederick, J. L. Achtyl, K. E. Knowles, E. A. Weiss, and F. M. Geiger. Surface-amplified ligand disorder in CdSe quantum dots determined by electron and coherent vibrational spectroscopies. *J. Am. Chem. Soc.*, 133:7476–7481, 2011.

[121] K. Salorinne, S. Malola, O. A. Wong, C. D. Rithner, X. Chen, C. J. Ackerson, and H. Häkkinen. Conformation and dynamics of the ligand shell of a water-soluble Au_{102} nanoparticle. *Nat. Commun.*, 7:10401, 2016.

[122] R. G. Nuzzo, B. R. Zegarski, and L. H. Dubois. Fundamental studies of the chemisorption of organosulfur compounds on gold (111). Implications for molecular self-assembly on gold surfaces. *J. Am. Chem. Soc.*, 109:733–740, 1987.

[123] H. D. Hill, J. E. Millstone, M. J. Banholzer, and C. A. Mirkin. The role radius of curvature plays in thiolated oligonucleotide loading on gold nanoparticles. *ACS Nano*, 3:418–424, 2009.

[124] H. Hinterwirth, S. Kappel, T. Waitz, T. Prohaska, W. Lindner, and M. Lämmerhofer. Quantifying thiol ligand density of self-assembled monolayers on gold nanoparticles by inductively coupled plasma-mass spectrometry. *ACS Nano*, 7:1129–1136, 2013.

[125] A. M. Smith, L. E. Marbella, K. A. Johnston, M. J. Hartmann, S. E. Crawford, L. M. Kozycz, D. S. Seferos, and J. E. Millstone. Quantitative analysis of thiolated ligand exchange on gold nanoparticles by ^{1}H NMR spectroscopy. *Anal. Chem.*, 87:2771–2778, 2015.

[126] B. M. DeVetter, S. T. Sivapalan, D. D. Patel, M. V. Schulmerich, C. J. Murphy, and R. Bhargava. Observation of molecular diffusion in polyelectrolyte-wrapped SERS nanoprobes. *Langmuir*, 30:8931–8937, 2014.

[127] G. Schneider, G. Decher, N. Nerambourg, R. Praho, M. H. V. Werts, and M. Blanchard-Desce. Distance-dependent fluorescence quenching on gold nanoparticles ensheathed with layer-by-layer assembled polyelectrolytes. *Nano Lett.*, 6:530–536, 2006.

[128] A. Elbakry, A. Zaky, R. Liebkl, R. Rachel, A. Goepferich, and M. Breunig. Layer-by-layer assembled gold nanoparticles for siRNA delivery. *Nano Lett.*, 9:2059–2064, 2009.

[129] S. Guo, Y. Huang, Q. Jiang, Y. Sun, L. Deng, Z. Liang, Q. Du, J. Xing, Y. Zhao, P. C. Wang, A. Dong, and X.-J. Liang. Enhanced gene delivery and siRNA silencing by gold nanoparticles coated with charge-reversal polyelectrolyte. *ACS Nano*, 4:5505–5511, 2010.

[130] R. C. Van Lehn, M. Ricci, P. H. J. Silva, P. Andreozzi, J. Reguera, K. Voïtchovsky, F. Stellacci, and A. Alexander-Katz. Lipid tail protrusions mediate the insertion of nanoparticles into model cell membranes. *Nat. Commun.*, 5:1–11, 2014.

[131] P. Gkeka, P. Angelikopoulos, L. Sarkisov, and Z. Cournia. Membrane partitioning of anionic, ligand-coated nanoparticles is accompanied by ligand snorkeling, local disordering, and cholesterol depletion. *PLoS Comp. Biol.*, 10:e1004769, 2014.

[132] E. Heikkilä, H. Martinez-Seara, A. A. Gurtovenko, M. Javanainen, H. Häkkinen, I. Vattulainen, and J. Akola. Cationic Au nanoparticle binding with plasma membrane-like lipid bilayers: Potential mechanism for spontaneous permeation to cells revealed by atomistic simulations. *J. Phys. Chem. C*, 118:11131–11141, 2014.

[133] E. Heikkilä, H. Martinez-Seara, A. A. Gurtovenko, I. Vattulainen, and J. Akola. Atomistic simulations of anionic $\mathrm{Au}_{144}(\mathrm{SR})_{60}$ nanoparticles interacting with asymmetric model lipid membranes. *Biochim. Biophys. Acta*, 1838:2852–2860, 2014.

[134] F. Simonelli, D. Bochicchio, R. Ferrando, and G. Rossi. Monolayer-protected anionic Au nanoparticles walk into lipid membranes step by step. *J. Phys. Chem. Lett.*, 6:3175–3179, 2015.

[135] J. M. Troiano, L. L. Olenick, T. R. Kuech, E. S. Melby, D. Hu, S. E. Lohse, A. C. Mensch, M. Dogangun, A. M. Vartanian, M. D. Torelli, E. Ehimiaghe, S. R. Walter, L. Fu, C. R. Anderton, Z. Zhu, H. Wang, G. Orr, C. J. Murphy, R. J. Hamers, J. A. Pedersen, and F. M. Geiger. Direct probes of 4 nm diameter gold nanoparticles interacting with supported lipid bilayers. *J. Phys. Chem. C*, 119:534–546, 2015.

[136] T. A. Qiu, J. S. Bozich, S. E. Lohse, A. M. Vartanian, L. M. Jacob, B. M. Meyer, I. L. Gunsolus, N. J. Niemuth, C. J. Murphy, C. L. Haynes, and R. D. Klaper. Gene expression as an indicator of the molecular response and toxicity in the bacterium *Shewanella oneidensis* and the water flea *Daphnia magna* exposed to functionalized gold nanoparticles. *Environ. Sci.: Nano*, 2:615–629, 2015.

[137] P. A. Patel, J. Jeon, P. T. Mather, and A. V. Dobrynin. Molecular dynamics simulations of layer-by-layer assembly of polyelectrolytes at charged surfaces: Effects of chain degree of polymerization and fraction of charged monomers. *Langmuir*, 21:6113–6122, 2005.

[138] V. Panchagnula, J. Jeon, and A. V. Dobrynin. Molecular dynamics simulations of electrostatic layer-by-layer self-assembly. *Phys. Rev. Lett.*, 93:037801, 2004.

[139] F. Carnal and S. Stoll. Adsorption of weak polyelectrolytes on charged nanoparticles. Impact of salt valency, pH, and nanoparticle charge density. Monte Carlo simulations. *J. Phys. Chem. B*, 115:12007–12018, 2011.

[140] P. S. Mdluli, N. M. Sosibo, P. N. Mashazi, T. Nyokong, R. T. Tshikhudo, A. Skepu, and E. van der Lingen. Selective adsorption of PVP on the surface of silver nanoparticles: A molecular dynamics study. *J. Mol. Struct.*, 1004:131–137, 2011.

[141] A. Kyrychenko, O. M. Korsun, I. I. Gubin, S. M. Kovalenko, and O. N. Kalugin. Atomistic simulations of coating of silver nanoparticles with poly(vinylpyrrolidone) oligomers: Effect of oligomer chain length. *J. Phys. Chem. C*, 119:7888–7899, 2015.

[142] J. Suh, H.-J. Paik, and B. K. Hwang. Ionization of poly(ethylenimine) and poly(allylamine) at various pHs. *Bioorg. Chem.*, 22:318–327, 1994.

[143] J. M. Troiano, A. C. McGeachy, L. L. Olenick, D. Fang, D. Liang, J. Hong, T. R. Kuech, E. R. Caudill, J. A. Pedersen, Q. Cui, and F. M. Geiger. Quantifying the electrostatics of polycation-lipid bilayer interactions. *J. Am. Chem. Soc.*, 139:5808–5816, 2017.

[144] W. L. Jorgensen, J. D. Madura, and C. J. Swenson. Optimized intermolecular potential functions for liquid hydrocarbons. *J. Am. Chem. Soc.*, 106:6638–6646, 1984.

[145] L. B. Wright, P. M. Rodger, and T. R. Walsh. Aqueous citrate: A first-principles and force-field molecular dynamics study. *RSC Adv.*, 3:16399–16409, 2013.

[146] A. Y. Kostritskii, D. A. Kondinskaia, A. M. Nesterenko, and A. A. Gurtovenko. Adsorption of synthetic cationic polymers on model phospholipid membranes: Insight from atomic-scale molecular dynamics simulations. *Langmuir*, 32:10402–

10414, 2016.

[147] R. W. Chang and A. Yethiraj. Dilute solutions of strongly charged flexible polyelectrolytes in poor solvents: Molecular dynamics simulations with explicit solvent. *Macromolecules*, 39:821–828, 2006.

[148] H. R. Bureau, D. R. Merz, E. Hershkovits, S. Quirk, and R. Hernandez. Constrained unfolding of a helical peptide: Implicit versus explicit solvents. *PLoS ONE*, 10:e0127034, 2015.

[149] N. Hoda and R. G. Larson. Explicit- and implicit-solvent molecular dynamics simulations of complex formation between polycations and polyanions. *Macromolecules*, 42:8851–8863, 2009.

[150] G. Reddy and A. Yethiraj. Implicit and explicit solvent models for the simulation of dilute polymer solutions. *Macromolecules*, 39:8536–8542, 2006.

[151] G. Reddy and A. Yethiraj. Solvent effects in polyelectrolyte adsorption: Computer simulations with explicit and implicit solvent. *J. Chem. Phys.*, 132:074903, 2010.

[152] S. J. Marrink, H. J. Risselada, S. Yefimov, D. P. Tieleman, and A. H. de Vries. The MARTINI force field: Coarse grained model for biomolecular simulations. *J. Phys. Chem. B*, 111:7812–7824, 2007.

[153] P. Hoogerbrugge and J. Koelman. Simulating microscopic hydrodynamic phenomena with dissipative particle dynamics. *Europhys. Lett.*, 19:155–160, 1992.

[154] R. D. Groot and P. B. Warren. Dissipative particle dynamics: Bridging the gap between atomistic and mesoscopic simulation. *J. Chem. Phys.*, 107:4423–4435, 1997.

[155] T. A. Qiu, M. D. Torelli, A. M. Vartanian, N. B. Rackstraw, J. T. Buchman,

L. M. Jacob, C. J. Murphy, R. J. Hamers, and C. L. Haynes. Quantification of free polyelectrolytes present in colloidal suspension, revealing a source of toxic responses for polyelectrolyte-wrapped gold nanoparticles. *Anal. Chem.*, 89:1823–1830, 2017.

[156] J. Turkevich, P. C. Stevenson, and J. Hillier. A study of the nucleation and growth processes in the synthesis of colloidal gold. *Discuss. Faraday Soc.*, 11:55–75, 1951.

[157] J. Kimling, M. Maier, B. Okenve, V. Kotaidis, H. Ballot, and A. Plech. Turkevich method for gold nanoparticle synthesis revisited. *J. Phys. Chem. B*, 110:15700–15707, 2006.

[158] X. Yang, M. Yang, B. Pang, M. Vara, and Y. Xia. Gold nanomaterials at work in biomedicine. *Chem. Rev.*, 115:10410–10488, 2015.

[159] C. Vericat, M. E. Vela, G. Benitez, P. Carro, and R. C. Salvarezza. Self-assembled monolayers of thiols and dithiols on gold: New challenges for a well-known system. *Chem. Soc. Rev.*, 39:1805–1834, 2010.

[160] J.-W. Park and J. S. Shumaker-Parry. Strong resistance of citrate anions on metal nanoparticles to desorption under thiol functionalization. *ACS Nano*, 9:1665–1682, 2015.

[161] A. Gole and C. J. Murphy. Polyelectrolyte-coated gold nanorods: Synthesis, characterization and immobilization. *Chem. Mater.*, 17:1325–1330, 2005.

[162] A. Rostek, D. Mahl, and M. Epple. Chemical composition of surface-functionalized gold nanoparticles. *J. Nanoparticle Res.*, 13:4809–4814, 2011.

[163] J. V. M. Girón, R. V. Vico, B. Maggio, E. Zelaya, A. Rubert, G. Benitez, P. Carro, R. C. Salvarezza, and M. E. Vela. Role of the capping agent in the interaction of hydrophilic Ag nanoparticles with DMPC as a model biomembrane. *Environ.*

Sci.: Nano, 3:462–472, 2016.

[164] J. M. Gisbert-González, J. M. Feliu, A. Ferre-Vilaplana, and E. Herrero. Why citrate shapes tetrahedral and octahedral colloidal platinum nanoparticles in water. *J. Phys. Chem. C*, 122:19004–19014, 2018.

[165] G. Mpourmpakis and D. G. Vlachos. Insights into the early stages of metal nanoparticle formation via first-principle calculations: The roles of citrate and water. *Langmuir*, 24:7465–7473, 2008.

[166] S. Monti, G. Barcaro, L. Sementa, V. Carravetta, and H. Ȧgren. Characterization of the adsorption dynamics of trisodium citrate on gold in water solution. *RSC Adv.*, 7:49655–49663, 2017.

[167] C. J. Murphy and J. M. Buriak. Best practices for the reporting of colloidal inorganic nanomaterials. *Chem. Mater.*, 27:4911–4913, 2015.

[168] A. E. Nel, L. Mädler, D. Velegol, T. Xia, E. M. V. Hoek, P. Somasundaran, F. Klaessig, V. Castranova, and M. Thompson. Understanding biophysicochemical interactions at the nano-bio interface. *Nat. Mater.*, 8:543–557, 2009.

[169] J. E. Gagner, S. Shrivastava, X. Qian, J. S. Dordick, and R. W. Siegel. Engineering nanomaterials for biomedical applications requires understanding the nano-bio interface: A perspective. *J. Phys. Chem. Lett.*, 3:3149–3158, 2012.

[170] B. Pelaz, G. Charron, C. Pfeiffer, Y. Zhao, J. M. de la Fuente, X.-J. Liang, W. J. Parak, and P. del Pino. Interfacing engineered nanoparticles with biological systems: Anticipating adverse nano-bio interactions. *Small*, 9:1573–1584, 2013.

[171] G. Zhu, Z. Huang, Z. Xu, and L.-T. Yan. Tailoring interfacial nanoparticle organization through entropy. *Acc. Chem. Res.*, 51:900–909, 2018.

[172] J. P. P. Ramalho, P. Gkeka, and L. Sarkisov. Structure and phase transformations

of DPPC lipid bilayers in the presence of nanoparticles: Insights from coarse-grained molecular dynamics simulations. *Langmuir*, 27:3723–3730, 2011.

[173] Y. Li, X. Zhang, and D. Cao. Self-assembly of patterned nanoparticles on cellular membranes: Effect of charge distribution. *J. Phys. Chem. B*, 117:6733–6740, 2013.

[174] P. Chen, Z. Huang, J. Liang, T. Cui, X. Zhang, B. Miao, and L.-T. Yan. Diffusion and directionality of charged nanoparticles on lipid bilayer membrane. *ACS Nano*, 10:11541–11547, 2016.

[175] G. Rossi and L. Monticelli. Gold nanoparticles in model biological membranes: A computational perspective. *Biochim. Biophys. Acta*, 1858:2380–2389, 2016.

[176] W. Phanchai, U. Srikulwong, A. Chompoosor, C. Sakonsinsiri, and T. Puangmali. Insight into the molecular mechanisms of AuNP-based aptasensor for colorimetric detection: A molecular dynamics approach. *Langmuir*, 34:6161–6169, 2018.

[177] L. B. Wright, P. M. Rodger, and T. R. Walsh. Structure and properties of citrate overlayers adsorbed at the aqueous Au(111) interface. *Langmuir*, 30:15171–15180, 2014.

[178] H. Heinz, B. L. Farmer, R. B. Pandey, J. M. Slocik, S. S. Patnaik, R. Pachter, and R. R. Naik. Nature of molecular interactions of peptides with gold, palladium, and Pd-Au bimetal surfaces in aqueous solution. *J. Am. Chem. Soc.*, 131:9704–9714, 2009.

[179] K. C. Jha, H. Liu, M. R. Bockstaller, and H. Heinz. Facet recognition and molecular ordering of ionic liquids on metal surfaces. *J. Phys. Chem. C*, 117:25969–25981, 2013.

[180] G. A. Jeffrey. *An Introduction to Hydrogen Bonding.* Oxford University Press, New York, 1997.

[181] S. Wang, H. Yao, S. Sato, and K. Kimura. Inclusion-water-cluster in a three-dimensional superlattice of gold nanoparticles. *J. Am. Chem. Soc.*, 126:7438–7439, 2004.

[182] J.-B. Bossa, F. Borget, F. Duvernay, P. Theulé, and T. Chiavassa. Formation of neutral methylcarbamic acid ($CH_3NHCOOH$) and methylammonium methylcarbamate $[CH_3NH_3^+][CH_3NHCO_2^-]$ at low temperature. *J. Phys. Chem. A*, 112:5113–5120, 2008.

[183] J.-J. Max and C. Chapados. Infrared spectroscopy of aqueous carboxylic acids: Comparison between different acids and their salts. *J. Phys. Chem. A*, 108:3324–3337, 2004.

[184] I. A. Mudunkotuwa and V. H. Grassian. Citric acid adsorption on TiO_2 nanoparticles in aqueous suspensions at acidic and circumneutral pH: Surface coverage, surface speciation, and its impact on nanoparticle-nanoparticle interactions. *J. Am. Chem. Soc.*, 132:14986–14994, 2010.

[185] Y. Li, X. Li, Z. Li, and H. Gao. Surface-structure-regulated penetration of nanoparticles across a cell membrane. *Nanoscale*, 4:3768–3775, 2012.

[186] L. Zhang, M. Becton, and X. Wang. Designing nanoparticle translocation through cell membranes by varying amphiphilic polymer coatings. *J. Phys. Chem. B*, 119:3786–3794, 2015.

[187] K. Lee, L. Zhang, Y. Yi, X. Wang, and Y. Yu. Rupture of lipid membranes induced by amphiphilic Janus nanoparticles. *ACS Nano*, 12:3646–3657, 2018.

[188] P. Español and P. Warren. Statistical mechanics of dissipative particle dynamics. *Europhys. Lett.*, 30:191–196, 1995.

[189] R. M. Füchslin, H. Fellermann, A. Eriksson, and H.-J. Ziock. Coarse graining and

scaling in dissipative particle dynamics. *J. Chem. Phys.*, 130:214102, 2009.

[190] R. Mao, M.-T. Lee, A. Vishnyakov, and A. V. Neimark. Modeling aggregation of ionic surfactants using a smeared charge approximation in dissipative particle dynamics simulations. *J. Phys. Chem. B*, 119:11673–11683, 2015.

[191] X. Li, L. Gao, and W. Fang. Dissipative particle dynamics simulations for phospholipid membranes based on a four-to-one coarse-grained mapping scheme. *PLoS ONE*, 11:e0154568, 2016.

[192] M. Kranenburg, J.-P. Nicolas, and B. Smit. Comparison of mesoscopic phospholipid-water models. *Phys. Chem. Chem. Phys.*, 6:4142–4151, 2004.

[193] I. V. Pivkin and G. E. Karniadakis. Accurate coarse-grained modeling of red blood cells. *Phys. Rev. Lett.*, 101:118105, 2008.

[194] R. D. Groot and K. L. Rabone. Mesoscopic simulation of cell membrane damage, morphology change and rupture by nonionic surfactants. *Biophys. J.*, 81:725–736, 2001.

[195] L. Gao, J. Shillcock, and R. Lipowsky. Improved dissipative particle dynamics simulations of lipid bilayers. *J. Chem. Phys.*, 126, 2007.

[196] S. Nikolov, A. Fernandez-Nieves, and A. Alexeev. Mesoscale modeling of microgel mechanics and kinetics through the swelling transition. *Appl. Math. Meth. Engl. Ed.*, 39:47–62, 2018.

[197] Z. Peng, X. Li, I. V. Pivkin, M. Dao, G. E. Karniadakis, and S. Suresh. Lipid bilayer and cytoskeletal interactions in a red blood cell. *Proc. Natl. Acad. Sci. U.S.A.*, 110:13356–13361, 2013.

[198] Y. Li, X. Zhang, and D. Cao. A spontaneous penetration mechanism of patterned nanoparticles across a biomembrane. *Soft Matter*, 10:6844–6856, 2014.

[199] A. Alexeev, W. E. Uspal, and A. C. Balazs. Harnessing janus nanoparticles to create controllable pores in membranes. *ACS Nano*, 2:1117–1122, 2008.

[200] D. Stelter and T. Keyes. Lipid packing in lipid-wrapped nanoparticles. *J. Phys. Chem. B*, 122:6755–6762, 2018.

[201] M. Dutt, O. Kuksenok, M. J. Nayhouse, S. R. Little, and A. C. Balazs. Modeling the self-assembly of lipids and nanotubes in solution: Forming vesicles and bicelles with transmembrane nanotube channels. *ACS Nano*, 5:4769–4782, 2011.

[202] X. Chu, F. Aydin, and M. Dutt. Modeling interactions between multicomponent vesicles and antimicrobial peptide-inspired nanoparticles. *ACS Nano*, 10:7351–7361, 2016.

[203] F. Xu, A. Bandara, H. Akiyama, B. Eshaghi, D. Stelter, T. Keyes, J. E. Straub, S. Gummuluru, and B. M. Reinhard. Membrane-wrapped nanoparticles probe divergent roles of GM3 and phosphatidylserine in lipid-mediated viral entry pathways. *Proc. Natl. Acad. Sci. U.S.A.*, 115:E9041–E9050, 2018.

[204] J. C. Shillcock and R. Lipowsky. Tension-induced fusion of bilayer membranes and vesicles. *Nat. Mater.*, 4:225–228, 2005.

[205] S. J. Marrink, A. H. de Vries, and D. P. Tieleman. Lipids on the move: Simulations of membrane pores, domains, stalks and curves. *Biochim. Biophys. Acta*, 1788:149–168, 2009.

[206] H. J. Risselada and S. J. Marrink. Curvature effects on lipid packing and dynamics in liposomes revealed by coarse grained molecular dynamics simulations. *Phys. Chem. Chem. Phys.*, 11:2056–2067, 2009.

[207] A. A. Gavrilov, A. V. Chertovich, and E. Y. Kramarenko. Dissipative particle dynamics for systems with high density of charges: Implementation of electrostatic

interactions. *J. Chem. Phys.*, 145:174101, 2016.

[208] J. B. Klauda, R. M. Venable, J. Alfredo Freites, J. W. O'Connor, D. J. Tobias, C. Mondragon-Ramirez, I. Vorobyov, A. D. MacKerell, Jr., and R. W. Pastor. Update of the CHARMM all-atom additive force field for lipids: Validation on six lipid types. *J. Phys. Chem. B*, 114:7830–7843, 2010.

[209] C.-M. Lin, C.-S. Li, Y.-J. Sheng, D. T. Wu, and H.-K. Tsao. Size-dependent properties of small unilamellar vesicles formed by model lipids. *Langmuir*, 28:689–700, 2011.

[210] C. Huang, D. Quinn, Y. Sadovsky, S. Suresh, and K. J. Hsia. Formation and size distribution of self-assembled vesicles. *Proc. Natl. Acad. Sci. U.S.A.*, 114:2910–2915, 2017.

[211] I. Hoffmann, C. Hoffmann, B. Farago, S. Preévost, and M. Gradzielski. Dynamics of small unilamellar vesicles. *J. Chem. Phys.*, 148:104901, 2018.

[212] A. C. Balazs, T. Emrick, and T. P. Russell. Nanoparticle polymer composites: Where two small worlds meet. *Science*, 314:1107–1110, 2006.

[213] P. K. Ghorai and S. C. Glotzer. Atomistic simulation study of striped phase separation in mixed-ligand self-assembled monolayer coated nanoparticles. *J. Phys. Chem. C*, 114:19182–19187, 2010.

[214] D. Zherebetskyy, M. Scheele, Y. Zhang, N. Bronstein, C. Thompson, D. Britt, M. Salmeron, P. Alivisatos, and L.-W. Wang. Hydroxylation of the surface of PbS nanocrystals passivated with oleic acid. *Science*, 344:1380–1384, 2014.

[215] S. N. Merz, Z. J. Farrell, J. Pearring, E. Hoover, M. Kester, S. A. Egorov, D. L. Green, and K. H. DuBay. Computational and experimental investigation of Janus-like monolayers on ultrasmall noble metal nanoparticles. *ACS Nano*,

12:11031–11040, 2018.

[216] K. G. Sprenger, Y. He, and J. Pfaendtner. *Probing How Defects in Self-Assembled Monolayers Affect Peptide Adsorption with Molecular Simulation*, pages 21–35. Molecular Modeling and Simulation. Springer, Singapore, 2016.

[217] K. Yang and Y.-Q. Ma. Computer simulation of the translocation of nanoparticles with different shapes across a lipid bilayer. *Nat. Nanotechnol.*, 5:579–583, 2010.

[218] C. F. Schmidt, D. Lichtenberg, and T. E. Thompson. Vesicle-vesicle interactions in sonicated dispersions of dipalmitoylphosphatidylcholine. *Biochemistry*, 20:4792–4797, 1981.

[219] M. Wong, F. H. Anthony, T. W. Tillack, and T. E. Thompson. Fusion of dipalmitoylphosphatidylcholine vesicles at 4°C. *Biochemistry*, 21:4126–4132, 1982.

[220] Z. Zheng, J. Saar, B. Zhi, T. A. Qiu, M. J. Gallagher, D. H. Fairbrother, C. L. Haynes, K. Lienkamp, and Z. Rosenzweig. Structure-property relationships of amine-rich and membrane-disruptive poly(oxonorbornene)-coated gold nanoparticles. *Langmuir*, 34:4614–4625, 2018.

[221] W. Lin and C. J. Murphy. A demonstration of Le Chatelier's Principle on the nanoscale. *ACS Cent. Sci.*, 3:1096–1102, 2017.

[222] E. Falck, T. Rog, M. Karttunen, and I. Vattulainen. Lateral diffusion in lipid membranes through collective flows. *J. Am. Chem. Soc.*, 130:44–45, 2008.

[223] A. C. Mensch, J. T. Buchman, C. L. Haynes, J. A. Pedersen, and R. J. Hamers. Quaternary amine-terminated quantum dots induce structural changes to supported lipid bilayers. *Langmuir*, 34:12369–12378, 2018.

Curriculum Vitae

Gene Chong
Department of Chemistry
Johns Hopkins University
3400 N Charles St
Baltimore, MD 21218

Biographical Sketch:
Place of Birth – Atlanta, GA
2006 IB Diploma Programme, Campbell High School, Smyrna GA

Education:

2016-present	Ph.D. Candidate, Chemistry, Johns Hopkins University
2014-2016	Graduate Research Assistant, Chemistry, Georgia Institute of Technology
2013	Post-baccalaureate, Chemistry, Georgia Institute of Technology
2010	B.A. Biology, Reed College

Honors and Awards:

2017	Student Seed Grant, Center for Sustainable Nanotechnology – Advancing accessible time- and length-scales for simulations of the nano-bio interface, using dissipative particle dynamics
2014	William H. Emerson Fellowship, Georgia Institute of Technology

Publications:

6. Tollefson†, E. J.; Allen†, C.; **Chong, G.**; Zhang, X.; Rozanov, N.; Bautista, A.; Cerda, J.; Pedersen, J. A.; Murphy, C. J.; Carlson*, E. E.; Hernandez*, R. "Preferential Binding of Cytochrome *c* to Anionic Ligand-Coated Gold Nanoparticles: A Complementary Computational and Experimental Approach," *ACS Nano*, **2019**, *13*, 6856-6866.
5. Wu, M.; Vartanian, A. M.; **Chong, G.**; Pandiakumar, A. K.; Hamers, R. J.; Hernandez, R.; Murphy*, C. J. "Solution NMR Analysis of Ligand Environment in Quaternary Ammonium-Terminated Self-Assembled Monolayers on Gold Nanoparticles: The Effect of Surface Curvature and Ligand Structure," *J. Am. Chem. Soc.*, **2019**, *141*, 4316-4327.

4. **Chong, G.**; Laudadio, E. D.; Wu, M.; Murphy, C. J.; Hamers, R. J.; Hernandez*, R. “Density, Structure, and Stability of Citrate^{3-} and H_2citrate$^-$ on Bare and Coated Gold Nanoparticles,” *J. Phys. Chem. C*, **2018**, *122*, 28393-28404.
3. Olenick, L. L.; Troiano, J. M.; Vartanian, A.; Melby, E. S.; Mensch, A. C.; Zhang, L.; Hong, J.; Mesele, O.; Qiu, T.; Bozich, J.; Lohse, S.; Zhang, X.; Kuech, T. R.; Millevolte, A.; Gunsolus, I.; McGeachy, A. C.; Dongangun, M.; Li, T.; Hu, D.; Walter, S. R.; Mohaimani, A.; Schmoldt, A.; Torelli, M. D.; Hurley, K. R.; Dalluge, J.; **Chong, G.**; Feng, Z. V.; Haynes, C. L.; Hamers, R. J.; Pedersen, J. A.; Cui, Q.; Hernandez, R.; Klaper, R.; Orr, G.; Murphy, C. J.; Geiger*, F. M. “Lipid Corona Formation from Nanoparticle Interactions with Bilayers,” *Chem*, **2018**, *4*, 2709-2723.
2. **Chong, G.**; Hernandez*, R. “Adsorption Dynamics and Structure of Polycations on Citrate-Coated Gold Nanoparticles,” *J. Phys. Chem. C*, **2018**, *122*, 19962-19969.
1. Borisovska, M.; Bensen, A. S. L.; **Chong, G.**; Westbrook*, G. L. “Distinct Modes of Dopamine and GABA Release in a Dual Transmitter Neuron,” *J. Neurosci.*, **2013**, *33*, 1790-1796.

Manuscripts in Preparation:

Chong, G.; Foreman-Ortiz, I. U.; Wu, M.; Bautista, A.; Murphy, C. J.; Pedersen, J. A.; Hernandez*, R. “Defects in Self-Assembled Monolayers on Nanoparticles Prompt Lipid Extraction and Bilayer Curvature-Dependent Deformations,” In preparation.

Chong, G.; Dahal, U.; Cui, Q.; Hernandez*, R. “Correspondence and Predictability in Vesicle Size and Structure across All-Atom, MARTINI, and Dissipative Particle Dynamics Simulations,” In preparation.

Presentations:

6.	Spring ’19	Invited Talk: Lectures in Computational Biophysics, Johns Hopkins University, Baltimore, MD: “Deciphering Biomolecular Corona Formation on Coated Gold Nanoparticles through All-Atom Molecular Dynamics and Dissipative Particle Dynamics Simulations”
5.	Fall ’18	National Meeting of the American Chemical Society, Division of Computers in Chemistry, Boston, MA: “Bottom-Up Coarse-Graining of Polyelectrolyte-Coated Gold Nanoparticles,” Oral.
4.	Fall ’18	National Meeting of the American Chemical Society, Division of Physical Chemistry, Boston, MA: “Benchmarking Coarse-Grained Simulations of the Nanoparticle-Bilayer Interface,” Poster.
3.	Summer ’17	American Conference on Theoretical Chemistry, Boston, MA: “Adsorption Dynamics and Structure of Ligands on Gold Nanoparticles,” Poster.
2.	Spring ’16	National Meeting of the American Chemical Society, Division of Computers in Chemistry, San Diego, CA: “Structure and Dynamics of Electrostatic Striped Colloidal Assemblies,” Oral.

1. Spring '16 National Meeting of the American Chemical Society, Division of Physical Chemistry, San Diego, CA: "Detailed and Coarse-Grained Simulations of Aggregating Charged Ligand-Coated Gold Nanoparticles," Poster.

Service / Outreach:

Undergraduate Poster Judge, National Meeting of the American Chemical Society, Division of Computers in Chemistry, Boston, MA (2018)

Representative, Student Board, Center for Sustainable Nanotechnology (2015-2018)

Member, Professional Development Committee, Center for Sustainable Nanotechnology (2017-present)

Blog Writer, Center for Sustainable Nanotechnology